

**Application of experimental and numerical simulation techniques to microscale
devices**

by

Vishwanath Somashekar

A dissertation submitted to the graduate faculty
in partial fulfillment of the requirements for the degree of
DOCTOR OF PHILOSOPHY

Major: Mechanical Engineering

Program of Study Committee:
Michael G. Olsen, Major Professor
Rodney O. Fox
James C. Hill
Ted Heindel
Terry Meyer

Iowa State University

Ames, Iowa

2011

Copyright © Vishwanath Somashekar, 2011. All rights reserved.

DEDICATION

I would like to dedidate this dissertation to my wife *Srivani (gunda)*, my parents *Manjula* and *Somashekar (ganesha)*, my in-laws *Indira* and *Harish*, and to my beloved late uncle *Prabhakara(MVP)*

TABLE OF CONTENTS

LIST OF TABLES	vi
LIST OF FIGURES	vii
ACKNOWLEDGEMENTS	x
CHAPTER 1. Introduction	1
1.1 General Introduction	1
1.2 Dissertation Organization	2
CHAPTER 2. Basics and theory of microPIV	4
2.1 PIV procedure	4
2.2 Differences between macroscopic PIV and microscopic PIV	5
2.3 MicroPIV Setup	6
2.4 Fluorescence and seed particles	6
2.4.1 Effect of Brownian motion	8
2.4.2 Particle Concentration	10
2.4.3 Depth of Correlation	10
2.5 Processing methods for microPIV images	11
2.5.1 Image overlapping	13
2.5.2 Average correlation	14
CHAPTER 3. Flow structure in a wide microchannel with surface grooves	16
3.1 Introduction	16
3.2 Device design	17
3.3 Methodology	19

3.4	Results	20
3.5	Conclusions	26
CHAPTER 4. Turbulent reactive mixing visualization		27
4.1	Introduction	27
4.2	Reactor geometry and Flow-delivery system	29
4.3	Experimental Technique and Apparatus	30
4.3.1	Technique Overview	30
4.3.2	Experimental Setup and Procedure	32
4.3.3	Image Processing Technique	34
4.4	Results and Discussion	35
4.4.1	Instantaneous Images	35
4.4.2	Image Thresholding and Statistical Analysis	38
4.4.3	Spatial Correlations and Large-Scale Structures	40
4.5	Conclusions	43
CHAPTER 5. Measurements of Turbulent Velocity Statistics in a Microscale Rectangular Confined Impinging Jets Reactor		44
5.1	Introduction	44
5.2	Device Fabrication	46
5.3	Methodology	47
5.4	Experimental Setup and Procedure	48
5.5	Results and Discussion	51
5.5.1	Instantaneous and Mean Velocity Fields	51
5.5.2	Turbulence Statistics	55
5.6	Conclusions	63
CHAPTER 6. Large Eddy Simulation of CIJR		65
6.1	Direct Numerical Simulation, RANS and LES	66
6.2	LES filters	68
6.3	Subgrid scale models	70

6.3.1	Smagorinsky model	70
6.3.2	Dynamic subgrid scale model	70
6.4	Numerical methods	72
6.4.1	Convective term	74
6.4.2	Diffusive term	76
6.4.3	Source terms	77
6.4.4	Temporal discretization	77
6.5	Discretization of the Navier-Stokes equations	79
6.6	Application of LES to CIJR using OpenFOAM	82
6.6.1	Grid generation	83
6.6.2	SGS models analyzed	84
6.6.3	Boundary conditions	84
6.6.4	Results and Discussion	85
6.6.5	Instantaneous and mean velocity flowfields	87
6.6.6	Reynolds Stresses	87
6.7	Conclusions	93
CHAPTER 7. Conclusion and Future work		95
APPENDIX A. ADDITIONAL MATERIAL		98
BIBLIOGRAPHY		101

LIST OF TABLES

Table 2.1	Signal-to-Noise ratios for various particle concentration and test-section depth (from Meinhart et al. [1])	10
Table 5.1	Summary of Images Captured	50
Table 6.1	Common LES filters	68
Table 6.2	Simulation Details	85
Table A.1	Interpolation schemes	98
Table A.2	Surface normal gradient schemes	99
Table A.3	Discretization schemes available in <i>gradSchemes</i>	99
Table A.4	Behavior of surface normal schemes used in <i>laplacianSchemes</i>	99
Table A.5	Behavior of interpolation schemes used in <i>divSchemes</i>	99
Table A.6	Discretization schemes available in <i>ddtSchemes</i>	100
Table A.7	Linear solvers	100
Table A.8	Preconditioner options	100
Table A.9	Smoother options	100

LIST OF FIGURES

Figure 2.1	Schematic setup of microPIV	7
Figure 2.2	Principle of fluorescence	8
Figure 2.3	Absorption and emission spectra of Nile red dye. Blue line represents absorption spectrum and Red line represents emission spectrum	9
Figure 2.4	Depth of correlation (image source: Nguyen et al.[2]	12
Figure 2.5	Low particle density image (image source: Wereley et al. [3]	13
Figure 2.6	Image formed after overlapping 9 low density recordings (image source: Wereley et al. [3]	14
Figure 3.1	Schematic of the high-aspect ratio staggered herringbone mixer. (a) Top view of the channel; flow is from bottom to top. (b) Close-up view of the herringbone pattern. (c) Representation of flow in channel illustrating the presence of counter-rotating rolls.	18
Figure 3.2	Flow at the interface between the channel and a groove. (a) Velocity field for $Re = 0.8$. Mean flow is from bottom to top; x denotes the transverse direction and y the streamwise direction. (b) Velocity orien- tation ϕ along the line A-A in (a); $\phi = 0$ corresponds to the flow aligned with the channel axis. (c) Relative magnitude of the interfacial velocity along the line A-A in (a). (d) Transverse component of the relative interfacial velocity. The vertical dashed lines mark the locations of the groove peaks.	21

Figure 3.3	Flow at the midplane of the channel. (a) Velocity field for $Re = 0.8$. Mean flow is from bottom to top. Solid line show groove locations. (b) Velocity field for $Re = 0.8$ with constant streamwise velocity of $12mm/s$ removed. (c) Streamwise velocity along line B-B in (a). (d) Normalized transverse velocity along the line B-B in (a) and (b). The vertical dash lines mark the locations of the groove peaks.	22
Figure 3.4	The normalized midplane velocities are plotted along the line B-B in Fig. 3.3a, and the normalized interface velocities are plotted along the line A-A in Fig. 3.2a	24
Figure 3.5	The normalized midplane velocities are plotted along the line B-B in Fig. 3.3a, and the normalized interface velocities are plotted along the line A-A in Fig. 3.2a for 90 degree micromixer	25
Figure 4.1	Geometry of the planar confined impinging jet reactor	29
Figure 4.2	Schematic of experimental setup	31
Figure 4.3	Sample original instantaneous images for $Re_j = 25$	36
Figure 4.4	Sample original instantaneous images for $Re_j = 1000$	36
Figure 4.5	Sample original instantaneous images for $Re_j = 1500$	37
Figure 4.6	Sample processed instantaneous images (bottom) for $Re_j = 25$ (left), $Re_j = 1000$ (middle) and $Re_j = 1500$ (right).	38
Figure 4.7	Contours of means for $Re_j = 25$ (left), $Re_j = 1000$ (middle) and $Re_j = 1500$ (right).	39
Figure 4.8	Contours of two-point spatial auto-correlation coefficient for $Re_j = 1000$ (top), $Re_j = 1500$ (bottom) at three different locations (marked with the '+' sign)	41
Figure 5.1	Geometry of CIJR	47
Figure 5.2	Schematic of the experimental Setup	49

Figure 5.3	Instantaneous Velocity Vector Fields at various Reynolds numbers. In all the figures presented above, every other vector has been deliberately removed for the sake of clarity	53
Figure 5.4	Mean Velocity Vector Fields at various Reynolds numbers. In the above figures, every other vector has been removed for the sake of clarity . .	54
Figure 5.5	Reynolds normal stress $\frac{\langle u'u' \rangle}{U^2}$ at Re 1000	55
Figure 5.6	Reynolds shear stress $\frac{\langle u'v' \rangle}{U^2}$ at Re 1500	56
Figure 5.7	Reynolds normal stress $\frac{\langle v'v' \rangle}{U^2}$ at Re 1000	56
Figure 5.8	Reynolds normal stress $\langle v'v' \rangle$ at Re 1500	57
Figure 5.9	Reynolds normal stress $\frac{\langle u'v' \rangle}{U^2}$ at Re 1000	58
Figure 5.10	Reynolds shear stress $\frac{\langle u'v' \rangle}{U^2}$ at Re 1500	59
Figure 5.11	Two Point Spatial Correlation at <i>Re</i> 1000	61
Figure 5.12	Two Point Spatial Correlation at <i>Re</i> 1500	62
Figure 6.1	Shape of filters in Spacial and Frequency domain	69
Figure 6.2	Arbitrary Control Volume	73
Figure 6.3	Variation of ϕ across two control volumes	75
Figure 6.4	Splitting of Area normal vector into orthogonal and non-orthogonal parts	77
Figure 6.5	PISO algorithm	81
Figure 6.6	OpenFOAM case structure	83
Figure 6.7	Streamlines at Re 1000	86
Figure 6.8	Instantaneous streamlines at Re 1500	86
Figure 6.9	Instantaneous velocity vector fields at Reynolds numbers of 1000 and 1500.	88
Figure 6.10	Average velocity vector fields at Reynolds numbers at 1000 and 1500. .	89
Figure 6.11	Normalized Reynolds normal stress $\frac{\langle u'u' \rangle}{U^2}$	90
Figure 6.12	Normalized Reynolds normal stress $\frac{\langle u'v' \rangle}{U^2}$	91
Figure 6.13	Normalized Reynolds normal stress $\frac{\langle v'v' \rangle}{U^2}$	92

ACKNOWLEDGEMENTS

I wish to express my gratitude to my advisor Dr. Michael G.Olsen for the incredible amount he has taught me during the course of this thesis. Dr Olsen, I am indebted to you for your support and advice throughout the research. The confidence you have shown in me has been my sole source of energy at times of need. Working with you has been an extremely rewarding experience.

I would like to thank Dr.Rodney O.Fox and Dr. James C. Hill for all their insights and words of encouragement which has given me hopes of survival under any circumstance. I would also like to thank the committee members for going through the thesis and making the suggestions, and, my group members Bo, Yan, Katrine, Ram and Alberto for all the support they have given me during my stay here at Iowa State University.

During the course of my education here at ISU, I have been fortunate to have met many people whose friendship will last for a lifetime. Ananth, Kirti, Sudip, Anu, Nikhil, Satya, Kritanjali, Prem, Abhi, Neeraj, Misha, Ankur, and Ramesh - thanks for all the support that you have shown me over the years and have made my stay in Ames a memorable one. Prem, Abhi and Neeraj - I will always cherish our serious and sometimes utterly nonsensical conversations during our group study. Special thanks to the SANKALP volleyball members, and the residents of 509, who helped me forget the frustrations of research.

I would like to thank my childhood friends Deepu, Prashanth and Sharath for their support besides the wonderful memories. Big thanks to my undergrad friends Moni, Prasadi, Bodi, Bonda, CC, Savya, Soori, Hoota, Dadi and Shivu, who have been instrumental in what I am today.

I am eternally grateful to my wife Srivani (gunda) for the years of patience, love and

unconditional support she has shown. I have enjoyed every single moment of the roller-coaster ride of life that we are in. Sowmya, I am thankful to you for being there for me during my ups and downs since we were kids. Thanks also go to my in-laws Indira and Harish for all their support and words of encouragement. Lastly, I would not be anything without the support of my parents Manjula and Somashekar. I am forever grateful to them, and consider myself blessed for having parents like them. I would like to thank them for their unconditional support and love.

Vishwa May 2011

CHAPTER 1. Introduction

1.1 General Introduction

Experimental investigation of fluid dynamics broadly serve two main goals. The first one is to understand the flow physics underlying the problem, and the second is to use the observations from the experiments as a benchmark for verifying the numerical simulations. On the experimental side, we have come a long way in the past decade since the first demonstration of microPIV technique by Santiago et al. [4] in a Hele-Shaw cell. MicroPIV was thought be very useful in steady laminar flows. Li and Olsen [5, 6], Liu et al. [7], and Cheng et al. [8], to name a few, have successfully applied the microPIV technique to understand turbulence in micro-scale devices. Two of the areas that have become relevant are the areas of mixing in micro-scale devices, and manufacturing of functional nanoparticles. Rapid mixing is essential for the successful operation of many microfluidic devices, but the laminar flows typically produced at these small scales make this difficult task to achieve. The various techniques and devices used for mixing enhancement in microscale systems can be found in the literature (see, [9, 10]). The use of nanoparticles in various applications is becoming increasingly commonplace. One particular area where nanoparticles can be transformative is the pharmaceutical industry. Here, nanoparticles may be used in cancer treatment, wherein the nanoparticles carrying the drug are coated with ligands which attach to the specific cells found in cancer tumors, allowing for the targeting of specific cells. Other nanoparticles application areas include cosmetics, pesticides, and paints [11, 12]. A very efficient manufacturing process for making nanoparticles is called Flash Nanoprecipitation. In particular, the multi-inlet vortex reactor (MIVR) and the confined impinging jets reactor (CIJR) have proved to be very effective [13, 14]. The size distribution of the nanoparticles produced are dependent on the turbulence generated inside the reactor.

The first step here is to visualize the turbulent structures using a simple, yet effective flow visualization technique. For this reason, a number of researchers have found phenolphthalein, a common pH indicator, particularly useful in turbulent mixing studies [15, 16, 17, 18, 19].

With the increase in the computational capability, what once seemed like an impossible thing to fathom, practical industrial problems can now be analyzed using techniques like large eddy simulation (LES). In the past, Reynolds Average Navier-Stokes equation was the most feasible way to address a practical problem, as it solves for only the mean quantities and the turbulence is modeled entirely. In LES, we explicitly solve the large structures, which are dependent on the flow geometry and the boundary conditions, and model the effect of small scale structures, as they are assumed to be universal in nature. This gives us a method to solve the problem as an unsteady one. In this work, we have made an effort to apply the experimental techniques first to high aspect-ratio microchannels, where we have analyzed the flowfields to investigate the effect of the presence of herringbone patterns in generating the transverse flow. We have also analyzed the turbulent characteristics of confined impinging jets reactor and compared them with the results from large eddy simulation.

1.2 Dissertation Organization

In Chapter 1, we introduce the microPIV technique, addressing issues that are important when analyzing flow at micron scale. Here, we deal mainly with how the optics that we use and the fluorescent seed particles that we choose affect the correlation signal. The different algorithms that can be used in case of low particle density are presented with their advantages and disadvantages. In Chapter 2, we present the application of microPIV technique in high aspect-ratio wide channels containing herringbone pattern on the floor of the channel. The velocity field data are presented in the midplane of the channel, and at the interface formed at location of the grooves. First, we discuss the effects of the very presence of the grooves on the flowfield. We then analyze the velocity normal to the direction of the flow in the midplane for different internal angles of the herringbone pattern. In Chapter 3, we present the flow visualization of the turbulent reactive mixing in CIJR. Here, we use phenolphthalein (Hln) as

pH indicator to visualize a reaction between Sodium hydroxide and Hydrochloric acid at inlet jet Reynolds numbers of 25, 1000 and 1500. Instantaneous images are thresholded to separate the image into regions of $\text{pH} > 9.3$ and $\text{pH} \leq 9.3$. Spatial autocorrelations are computed at different locations and analyzed. In Chapter 4, the application of microPIV to confined impinging jets reactor is presented. Here, we showcase the instantaneous flowfields at inlet jets Reynolds numbers of 200, 1000 and 1500. Turbulent statistics like the Reynolds normal stresses and Reynolds shear stresses are presented. We also compute the spatial auto and cross correlations of the velocity fluctuations to analyze the coherent structures in the flow. Chapter 5 describes the basic idea behind the large eddy simulation and the finite volume method of calculating the flowfields using the PISO algorithm. We deal only with the case of incompressible flow as that applies to our situation. We then present the flowfields and the turbulent statistics in the midplane of the CIJR and compare with the results from the application of microPIV to CIJR. Finally, Chapter 6 summarizes the results from all the work, and prompts towards possible future work.

CHAPTER 2. Basics and theory of microPIV

Particle Image Velocimetry (PIV) has been in use to calculate spatially and temporally resolved velocity fields for some time now. The detailed review can be found in Adrian [20] and Raffel et. al [21]. This chapter deals specifically with the Micro Particle Image Velocimetry (μ PIV) and some of the commonalities between the PIV and microPIV are omitted.

2.1 PIV procedure

The idea of PIV is very simple and can be described as follows:

1. The flow to be analyzed is seeded with flow tracers (e.g. glass microspheres, carboxylated polystyrene beads). The tracers are chosen judiciously such that the density of the tracers are close to that of the medium to which they are added, and that they follow the flow faithfully without altering the flow.
2. A bright light source such as laser, LED, xenon lamp etc. is used to illuminate the desired region in the flow domain. Here, light shaping optics are used to either generate a thin laser sheet in the case of PIV or a collimated beam of light in case of microPIV.
3. Using a precise timing unit to generate laser pulses, two images are recorded in an interval of time Δt , either to a photographic film or to a CCD (Charge Coupled Device) camera array.
4. The images are divided into interrogation windows, and a cross correlation algorithm is applied to the corresponding windows from first and second images, respectively. This gives the average displacement of the particles in the interrogation volume.

5. Knowing the displacement and the time between the two images, Δt , the X and Y components of the velocity is calculated as

$$u = \frac{\Delta x}{\Delta T}; v = \frac{\Delta y}{\Delta T} \quad (2.1)$$

MicroPIV was first demonstrated by Santiago et al. [4], by calculating the steady state velocity fields or flow around a heli-shaw cell. They used the Hg-arc lamp as the light source. Meinhart et al. [22] used double pulsed Nd:YAG laser as the light source to demonstrate microPIV. Since then microPIV has not only become viable, but also a reliable tool to accurately calculate the flowfields in microscale devices.

2.2 Differences between macroscopic PIV and microscopic PIV

In PIV, a thin laser sheet is generated and is used to illuminate a plane in the flow domain. The scattered light from the seed particles is captured either on a photographic film or onto a CCD array for further processing. The thickness of the light sheet is in the order of a few millimeters, which is almost always smaller than the depth of field of the camera lens being used. Therefore, only the particles illuminated by the laser sheet contribute towards the calculation of the correlation. The microscale devices pose a few challenges.

- Typical manufacturing processes for microfluidic devices include etching and micromachining. The geometry is etched onto a silicon wafer and then bonded to a glass cover slip to seal the device, thereby, giving optical access in only one direction, making the use of laser sheet impossible.
- The generation of laser sheet in microscale devices necessitates the use of optical guides and wave guides inside the device [1], which would increase the complexity and the cost of fabrication. Hence, usage of light sheet is not feasible.
- The characteristic dimension of a typical microscale device is of the order of a few hundred microns and for one to use a laser sheet, we need the thickness of the laser sheet to be a few microns thick. This laser sheet further has to be aligned with the focal plane of the microscope objective, which is virtually impossible to achieve.

Therefore, in microPIV, one uses volume illumination, where the entire flow field is illuminated. Now, the measurement plane is determined by the focal plane of the microscope objective being used. However, the downside of this procedure is that we now no longer have particles only in the focal plane that contribute to the correlation, instead we have particles both in front and behind the focal plane contributing to the correlation signal.

2.3 MicroPIV Setup

A schematic of the microPIV setup is shown in Fig. 2.1. A double pulsed 532nm Nd:YAG laser is used as a light source. The beam is expanded using a beam expander to obtain a collimated beam. The beam is then guided through the optical train of the inverted microscope. The dichroic mirror in the filter cube reflects the laser beam and steers it by 90° , which then passes through the microscope objective and gets focused at the objective's focal plane. The particle solution, which is seeded with fluorescent microspheres is injected via syringe pump into the device. When the laser light strikes the particles inside the channel, part of it excites the particles and results in the fluorescence emission, and part of it is scattered. It is worth noting here that there might be some light reflected off of the channel walls as well. The scattered light and the fluorescent emission are collected by the objective. The filter cube is fitted with a long pass filter, so that all the light from the laser (scattered from particles and reflected from the wall) is removed and only the fluorescence is recorded by the camera. The camera and the laser are triggered synchronously by a timing unit (not shown in the figure).

2.4 Fluorescence and seed particles

Fluorescence is the emission of energy (photons) from an atom, when the atom comes back to its ground state (low energy stable configuration) from an excited state. The process is schematically shown in Fig. 2.2. Fluorophores are the molecules which are capable of emitting fluorescence. When the fluorophores absorb sufficient energy in the form of light, they reach what is called excited state. There are multiple excited states that a fluorophore can attain

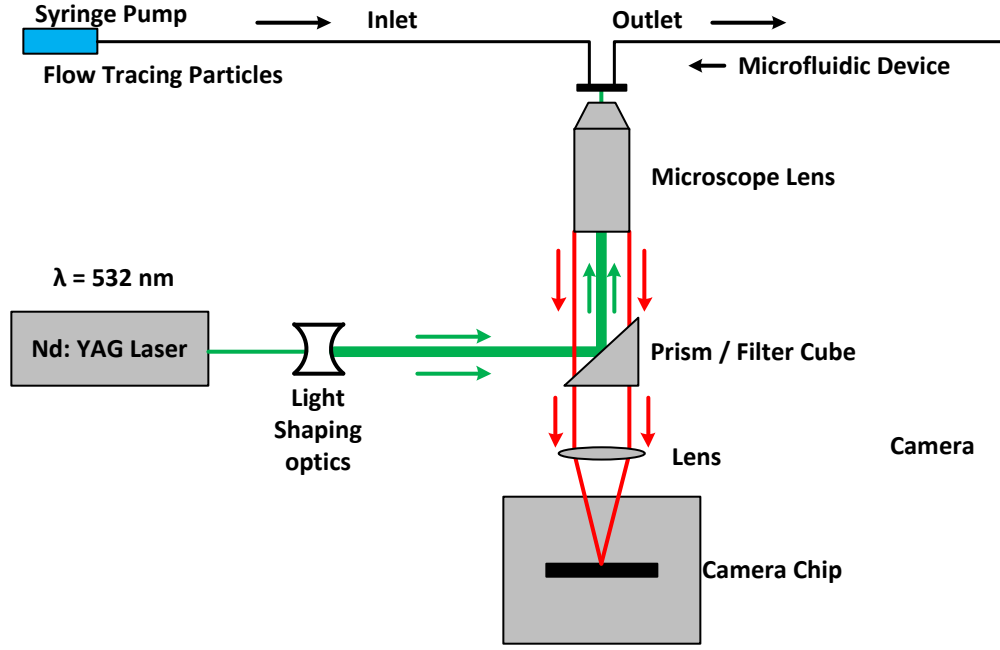


Figure 2.1 Schematic setup of microPIV

depending on the wavelength and the energy of the excitation light. This is depicted by the process 1 in Fig. 2.2. This excited state is very unstable and the fluorophore loses some energy and attains the lowest possible excited state which is semi-stable (process 2). This process lasts anywhere between 10^{-15} to 10^{-9} s. They then come back to the ground state by emitting energy (process 3). The energy of a photon is related to the wavelength by

$$E = \frac{hc}{\lambda}, \quad (2.2)$$

where, h is Planck's constant, c is the speed of light, and λ is the wavelength. The emitted light is at lower energy, and hence at a longer wavelength (from the equation above, we can see that $E \propto 1/\lambda$). The fluorophore can absorb a range of wavelengths called the excitation spectrum, and can emit a range of wavelengths called the emission spectrum. The absorption and the emission spectrum for a typical dye (nile red) is shown in Fig. 2.3. This particular dye has an excitation maximum of 535nm and an emission maximum of 575nm. We choose a particular dye such that the excitation wavelength is close to the wavelength of light source (laser), and the emission wavelength is long enough for us to separate the absorption light, so

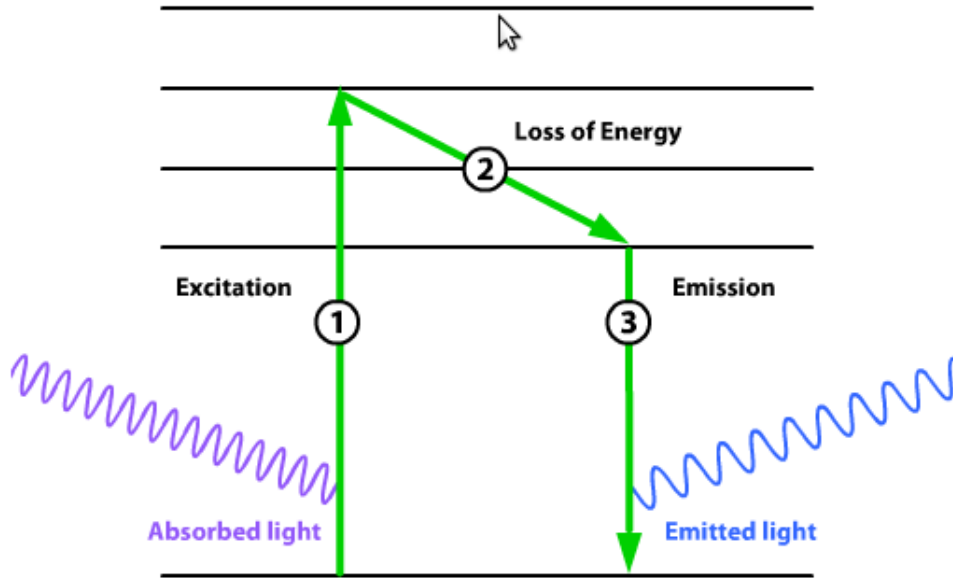


Figure 2.2 Principle of fluorescence

as to record just the particle images on the CCD array. This is very important as we need to make sure that we record bright particle images. The difference between the emission maxima and excitation maxima is called Stokes' shift.

2.4.1 Effect of Brownian motion

When sub-micron sized particles are used as tracers, the interaction between the particles and the fluid give rise to random motion of particles, known as Brownian motion. This will result in the particles not faithfully following the fluid. The effect of Brownian motion was addressed by Santiago et al.[4], by calculating a relative error

$$\epsilon_B = \frac{1}{u} \sqrt{\frac{2D}{\Delta T}}, \text{ where} \quad (2.3)$$

the diffusion coefficient D , is given by $D = KT/(6\pi\mu d_p)$, u is the velocity and ΔT is time interval between the frames. It can be seen from the equation that the error decreases as the flow rate increases, ΔT increases. The error also increases with the increase in temperature and decrease in particle diameter. The nature of the error is random and hence should decrease

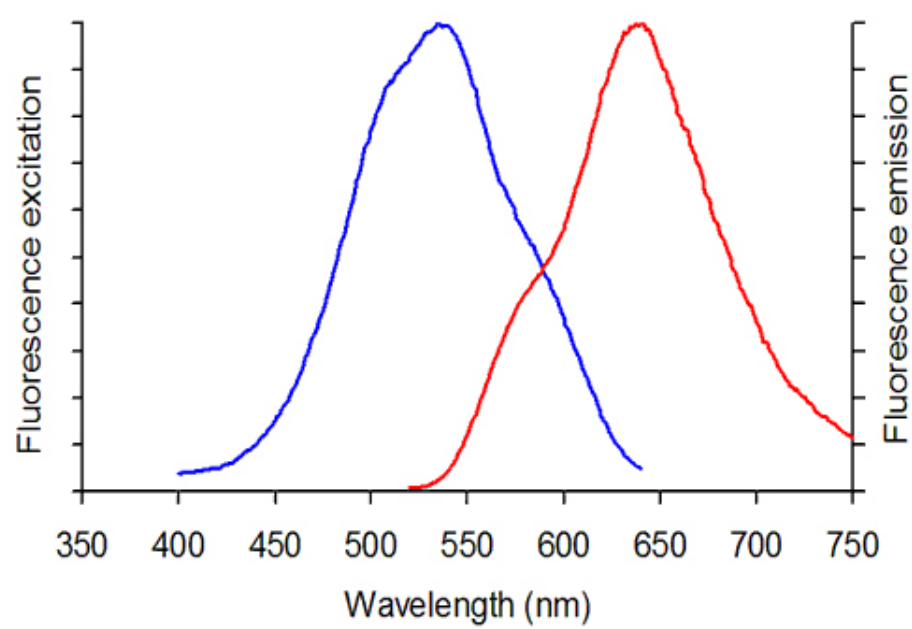


Figure 2.3 Absorption and emission spectra of Nile red dye. Blue line represents absorption spectrum and Red line represents emission spectrum

Table 2.1 Signal-to-Noise ratios for various particle concentration and test-section depth (from Meinhart et al. [1])

Test-section depth (μm)	Particle concentration (by volume)			
	0.01%	0.02%	0.04%	0.08%
25	2.2	2.1	2.0	1.9
50	1.9	1.7	1.4	1.2
125	1.5	1.4	1.2	1.1
170	1.3	1.2	1.1	1.0

when averaging over a population of particles. For a detailed treatment of effects of Brownian motion, the reader is referred to Olsen and Adrian [23].

2.4.2 Particle Concentration

Since we use volume illumination in microPIV, all the particles in the illuminated region fluoresce. Emissions from the particles that are not in the focal plane and are out of focus contribute to the background noise, thus reducing the Signal-to-Noise Ratio (SNR). The SNR is defined as the ratio of the peak intensity of the particle in focus to the average background intensity. Table 2.1 shows the SNR for various particles concentrations and test-section depths.

In most cases, the depth of the channel is something that we have no control over as the device is fabricated to some predefined design specifications. In such situations, the one parameter that we can control is the particle concentration. It is evident from the above table that the particle concentration should be kept low in deep channels in order to obtain high SNR.

2.4.3 Depth of Correlation

As it has been mentioned earlier, in microPIV, volume illumination is used. As a result of this, all the particles in the cone of light fluoresce leading either to the in-focus particle image or out-of-focus background noise. Depth of correlation of an imaging system [24], is defined as the region on either of the focal plane, beyond which the correlation signal of particles do not

contribute towards the calculation of correlation function. It is defined by

$$Z_{corr} = \left[\frac{1 - \sqrt{\varepsilon}}{\sqrt{\varepsilon}} \left(f^{\#2} d_p^2 + \frac{5.95(M+1)^2 \lambda^2 f^{\#4}}{M^2} \right) \right]^{1/2}, \text{ where} \quad (2.4)$$

d_p is the particle diameter, M is the magnification of the microscope objective, $f^{\#} = 1/2NA$, is the focal number which is related to the numerical aperture (NA) of the objective, λ is the wavelength of the emitted fluorescence, and $\varepsilon = 0.01$ is chosen. It can be seen from Eqn. 2.4 that the depth of correlation is weakly dependent on the magnification M , and it increases almost linear with $f^{\#}$ for large particles and increases approximately with square of $f^{\#}$ for small particles. An alternate equation developed by Meinhart et al. [1] can be used to calculate the measurement depth δz_m , given by

$$\delta z_m = \frac{3n\lambda_0}{NA^2} + \frac{2.16d_p}{\tan \theta} + d_p, \text{ where} \quad (2.5)$$

n is the refractive index of the fluid between the microfluidic device and the objective lens, λ_0 is the wavelength of the light in a vacuum being imaged by the optical system, NA is the numerical aperture of the objective lens, M is the magnification of the system, and d_p is the particle diameter. The depth of correlation effect can be further reduced by applying a power filter to the particle images as proposed in Bourdon et al. [25].

Figure. 2.4 shows velocity measurement, which is a weighted average of the velocities within the measurement volume. The particles on the focal plane have the most contribution to the correlation signal, and as the particle distance increases from the focal plane, their effect diminishes.

2.5 Processing methods for microPIV images

As described in Sec. 2.1, each PIV recording is divided into interrogation windows and then the cross-correlation is applied on the corresponding windows to obtain the displacement of particles. This assumes that there is sufficient number of particles (between 5 and 15) in each interrogation volume for obtaining a reliable and accurate velocity field. However, in many microPIV experiments, using a high number of particles per interrogation volume will result in

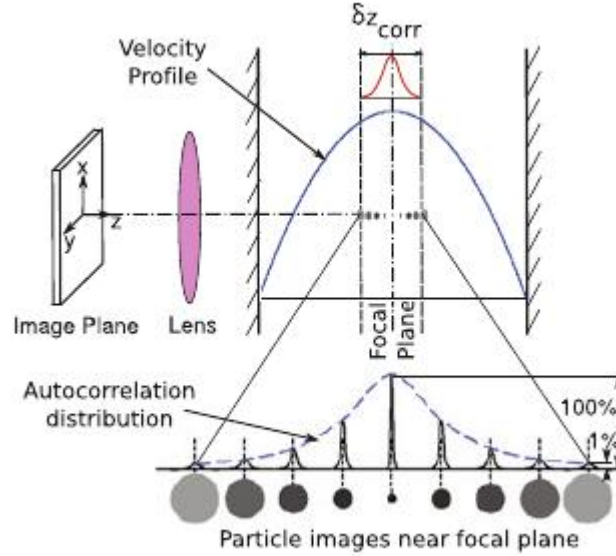


Figure 2.4 Depth of correlation (image source: Nguyen et al.[2])

an increase in the background noise, which in turn will lead to poor correlation fields due to low SNR. Hence, very few particles are used in such applications leading to low density recordings as shown in Fig. 2.5. One way to work around this would be to use an interrogation window big enough to contain a large number of particles. Doing so will result in an accurate velocity field, however, at an expense of spatial resolution, which is not desired. One would process with a smaller interrogation window with a fewer particle density, again with the consequence of unreliable velocity field, due to lack of correlation and high noise levels. One could resort to particle tracking technique, where we calculate the velocity of individual particle from one frame to the other. The disadvantage of this is that the vector field is sparse and the velocity is not arranged on a nice grid, like it is when a regular cross-correlation is applied. In order to have the individual vectors on regular grids, we further introduce interpolation errors. To overcome these drawbacks, special techniques have to be employed when dealing with low density images.

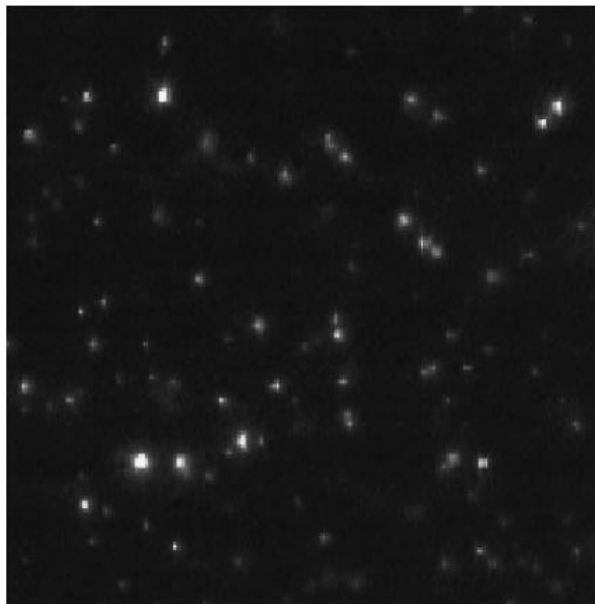


Figure 2.5 Low particle density image (image source: Wereley et al. [3])

2.5.1 Image overlapping

This is a very simple technique which does not require one to use any specialized interrogation schemes. Instead, the idea is to address the main issue with the low density PIV images, which is, fewer particles. This is accomplished by overlapping a number of individual low density recordings to form an image pair with a lot of particle pairs, so that we can apply the traditional cross-correlation technique to obtain the velocity field. Fig. 2.6 shows the result of nine images overlapped to form one image. The overlapped image is calculated as

$$I(x, y) = \max(I_k(x, y); k = 1, 2, 3, \dots, N) \quad (2.6)$$

The number of individual images used to form the overlapped images depends on the number of particles in the individual images. Using too many images results in a situation, wherein one may not even distinguish one particle from the other. Besides increasing the number of particles in the overlapped image, another important thing this process does is to decrease the depth of correlation. This is because when we apply Eqn. 2.6, we are taking the maximum intensity value at a particular pixel, and the particles are brightest when they are on the focal

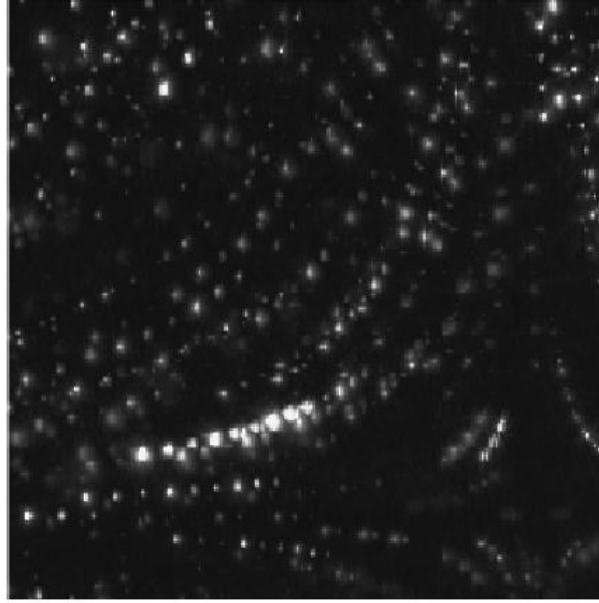


Figure 2.6 Image formed after overlapping 9 low density recordings (image source: Wereley et al. [3])

plane. Therefore, after the operation, we would have picked all the particles close to the focal plane, which would mean that we have decreased the depth of correlation.

2.5.2 Average correlation

Another technique to overcome the low seeded flows, is to use the average correlation method, also known as ‘sum of correlation’ method. This technique works well only for steady flows as under steady state condition, the location of correlation peak will not change from one image pair to other. For an interrogation window of size $m \times n$, the correlation function is given by

$$R(x, y) = \sum_{j=1}^n \sum_{i=1}^m I(i, j) \cdot I'(i + x, j + y), \quad (2.7)$$

where, the correlation peak would represent the displacement. However, when we have poorly seeded flows, this correlation peak may be embedded amongst other peaks which are randomly distributed due to the lack of image pairs and background noise. Since, we know that the location of the correlation peak should be at the same location because of the steady state

flow, one might average the correlation at each pixel over a number of images using

$$R_{ave} = \frac{1}{N} \sum_{k=1}^N R_k(x, y) \quad (2.8)$$

By performing this operation, we can get rid of the random peaks in the correlation field as they average to zero, with only the correlation peak left intact.

CHAPTER 3. Flow structure in a wide microchannel with surface grooves

Abstract

We present an experimental analysis of pressure-driven flow in a high (62:1) aspect ratio microchannel having a repeated herringbone surface pattern. The velocity field is determined at the groove-channel interface and at the midplane of the channel using microscopic particle image velocimetry. At Reynolds numbers of 0.08, 0.8 and 8, we observe secondary flow patterns consisting of counter-rotating flow cells aligned in the streamwise direction. The strength of this secondary flow is inhibited by fluid inertia when $Re = 8$. The resulting flow structure can be viewed as splitting one wide channel into multiple smaller channel without the use of solid boundaries.

3.1 Introduction

Rapid mixing is essential for the successful operation of many microfluidic devices, but the laminar flows typically produced at these small scales make this difficult to achieve. The various techniques and devices used for mixing enhancement in microscale systems are too numerous to detail here; several reviews can be found in the literature (see, [9, 10]). Here, we consider the ‘passive’ approach in which mixing is produced by steady, pressure-driven flow through a microchannel; this approach enables simple fabrication and operation in support of disposable single-use systems.

When mixing in steady, pressure-driven microchannel flow, the challenge lies in using the channel geometry to stretch and fold the fluid. Methods based on this approach include the generation of strong spatially-varying secondary flows in the channel cross-section and lamination of the fluid by physically splitting and recombining the channel. Secondary flow,

i.e., flow orthogonal to the mean flow direction, can be produced by, say, bends in the channel geometry [26] or recessed grooves in the channel wall [27]. Mixing is enhanced by varying these geometric features, and thus the secondary flow patterns, along the channel. Fluid lamination enhances mixing by physically splitting the main channel into multiple smaller channels that are later recombined [28, 29, 30]. Here, we discuss a hybrid technique in which the secondary flow itself splits the fluid into parallel counter-rotating regions as it moves through a single channel.

3.2 Device design

A schematic of the microchannel geometry considered in this study is shown in Fig. 3.2. This system was fabricated using standard polydimethoxysiloxane (PDMS) replica molding ([31, 32]). The channel is 2.5 mm wide by 40 μm deep, giving an aspect ratio of approximately 62:1. The floor of the channel contains recessed grooves arranged in a staggered herringbone pattern that extends the pattern introduced by Stroock et al. [27]. Each groove measures 50 μm wide by 20 μm deep and consists of six sequential grooves separated by 100 μm in the axial direction. Successive herringbone patterns are staggered as in Stroock et al. [27], so that the fluid is mixed due to axial variations in the secondary flow. Here, we consider only the effect of one herringbone pattern on the flow.

Our motivation for studying a high-aspect ratio microchannel is twofold. First, there are a number of applications for which it is necessary to enhance fluid transport in high-aspect ratio geometry, including DNA analysis on micro-arrays [33] and studies of cell chemotaxis [29, 34]. Second, it has been shown that a herringbone pattern can produce significant secondary flow in a channel with small aspect ratio [27] (i.e., approximately 3:1). This previous work and the present results together give evidence that this approach can be used to generate counter-rotating secondary flows in a wide variety of channel aspect ratios.

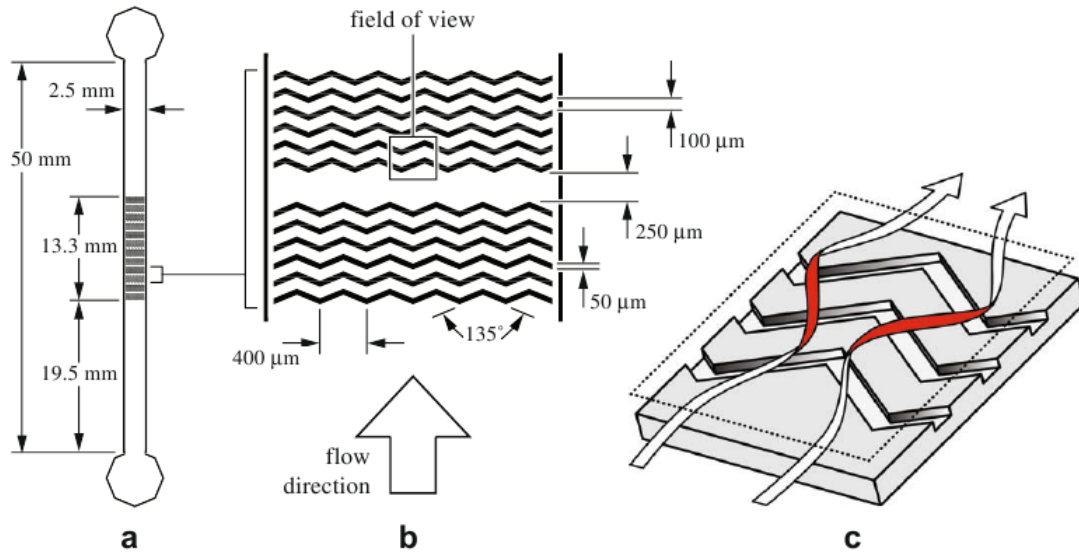


Figure 3.1 Schematic of the high-aspect ratio staggered herringbone mixer. (a) Top view of the channel; flow is from bottom to top. (b) Close-up view of the herringbone pattern. (c) Representation of flow in channel illustrating the presence of counter-rotating rolls.

3.3 Methodology

The flow generated in this channel is illustrated in Fig. 3.1c. A pressure gradient drives fluid along the axis of the channel in the streamwise direction. When the fluid encounters a groove, it tends to move along the groove [35]. The angle of a surface groove thus causes oblique fluid motion along the groove direction near the bottom of the channel. The opposing orientation of neighboring grooves causes this oblique flow to change direction near the peaks of each chevron, and the expected effect of this pattern is the generation of counter-rotating secondary flow as the fluid moves down the channel.

The strength of this secondary flow relative to the streamwise flow is due to competition between the influence of the surface grooves through viscous effects and the inertia of the fluid as it moves down the channel. This competition is characterized by the Reynolds number, $Re = \rho U D_h / \mu$, where ρ is the fluid density, U is the mean flow velocity, D_h is the hydraulic diameter of the channel, and μ is the molecular viscosity of the fluid. For the present investigation we consider flowrates of $6\mu\text{L}/\text{min}$, $60\mu\text{L}/\text{min}$, and $600\mu\text{L}/\text{min}$ corresponding to Reynolds numbers of 0.08, 0.8, and 8, respectively.

The details of the flow in this channel were determined using microscopic particle image velocimetry (μPIV) [4, 22]. The working fluid was deionized water. The flow was generated and controlled using a Stoelting 210P syringe pump. The flow was seeded with $1\mu\text{m}$ diameter fluorescent carboxylated polystyrene microspheres, illumination was provided by a double-pulsed Nd:YAG Continuum Minilite laser, and images were captured with a LaVision Imager Intense CCD camera. The flow was imaged using a 40x 0.6NA objective, and the CCD camera was mounted to a Nikon TE-300 inverted microscope using a 0.45x coupling, resulting in an overall magnification of 18x and a measurement depth, i.e., a depth of correlation [24, 36] of $8.2\mu\text{m}$. Velocity field measurements were made at two different depths within the channel: at the centerplane of the channel, and at the interface of the channel and the grooves. The field of view of the microscope was set to be the width of a single chevron (i.e., 0.4 mm). A chevron near the centerline of the channel was chosen for this investigation, as indicated in Fig. 3.1b. For each flow condition and location investigated, 1000 μPIV image pairs were acquired

and analyzed using the sum of correlation technique [3]. Individual interrogation regions were overlapped by 50%, resulting in an in-plane vector spacing of $5.7 \mu\text{m}$. Results were quantified by averaging the data from at least three separate runs performed on the same device. Further details of the μPIV system used in the present work can be found in Li and Olsen [6].

The flow causes this channel to expand slightly at $Re = 8$. In order to accurately compare results at different flowrates, we normalize velocity values by the spatial average of the streamwise velocity measurement in the midplane, namely

$$V_{ave}(Re) = \frac{1}{|x_2 - x_1|} \int_{x_1}^{x_2} V_y^M(x; Re) dx \quad (3.1)$$

where, x is the transverse direction, V_y^M is the streamwise component of the midplane velocity, the integral is along the line B-B in Fig. 3.3a, and the integration limits are chosen to cover the experimental field of view.

3.4 Results

A representative velocity field at the groove-channel interface is shown in Fig. 3.2a for $Re = 0.8$. Near the peaks of the chevron the interfacial flow is aligned with the axis of the channel, while between these peaks the interfacial flow is oblique to the channel axis. Fig. 3.2b quantifies ϕ , the angle of the interfacial flow with respect to the axial direction, along the line labeled A-A in Fig. 3.2a. Fig. 3.2c shows the normalized interfacial velocity magnitude, V^I/V_{ave} , along this same line. Variations in both ϕ and V^I/V_{ave} are essentially identical for $Re = 0.08$ and 0.8 , while the flow at $Re = 8$ shows a slight decrease in the extremes of ϕ and a more substantial decrease in the normalized velocity magnitude. The result of this oblique flow along the groove is a sinusoidal-like variation in V_x^I , the transverse component of the interfacial velocity along the line C-C, as shown in Fig. 3.2d.

The oblique interfacial flow generates a secondary flow pattern that penetrates into the bulk flow, as seen by examining the flow at midplane; a representative velocity field is shown in Fig. 3.3a for $Re = 0.8$. Rather than being purely in the streamwise direction, the midplane velocity field is ‘wavy’ due to the secondary flow. This effect is more clearly visible when a constant streamwise velocity is subtracted from each velocity vector, as shown in Fig. 3.3b.

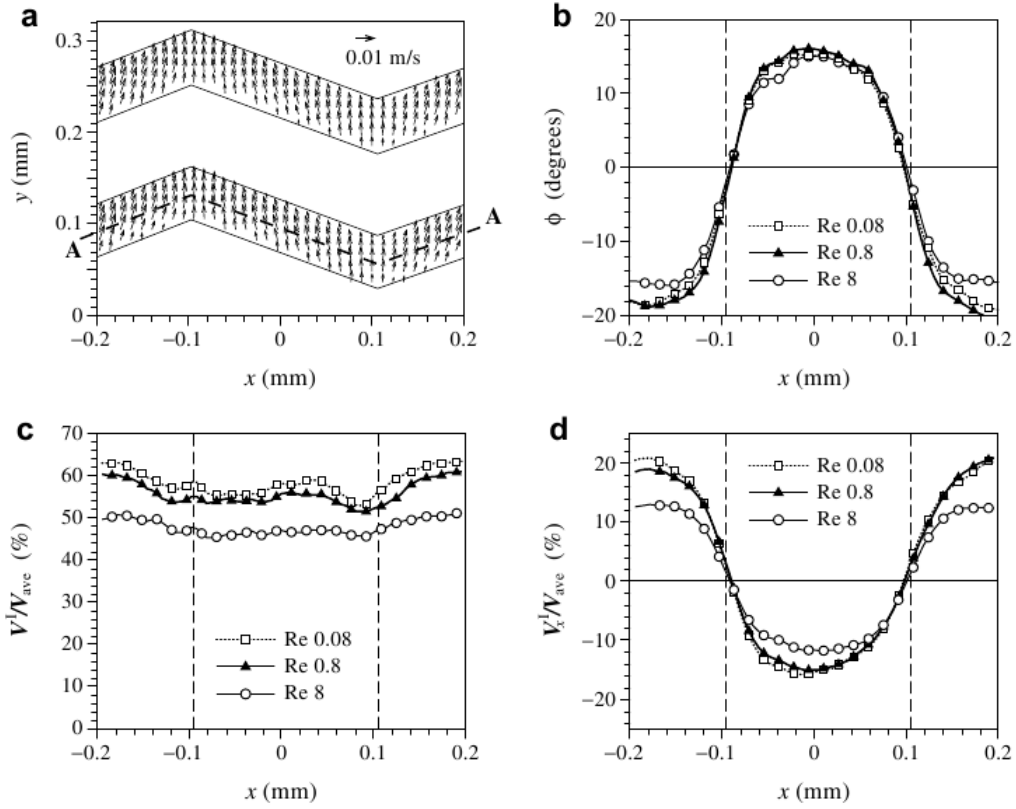


Figure 3.2 Flow at the interface between the channel and a groove. (a) Velocity field for $Re = 0.8$. Mean flow is from bottom to top; x denotes the transverse direction and y the streamwise direction. (b) Velocity orientation ϕ along the line A-A in (a); $\phi = 0$ corresponds to the flow aligned with the channel axis. (c) Relative magnitude of the interfacial velocity along the line A-A in (a). (d) Transverse component of the relative interfacial velocity. The vertical dashed lines mark the locations of the groove peaks.

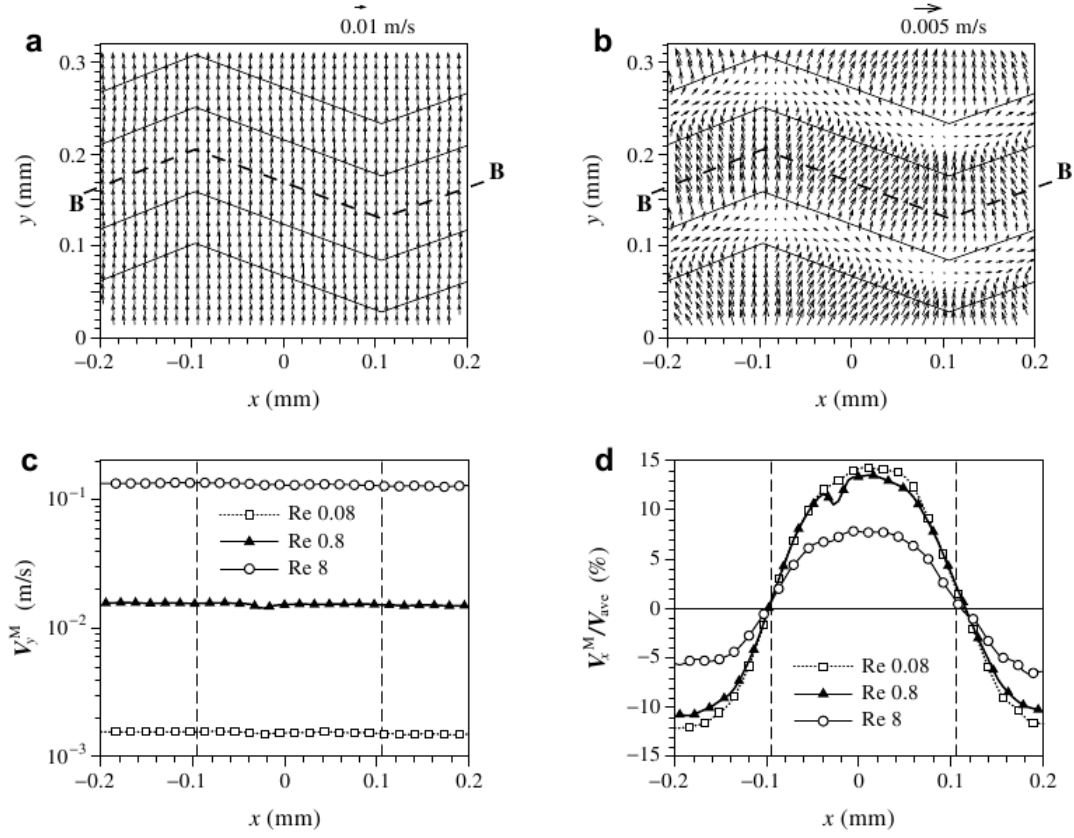
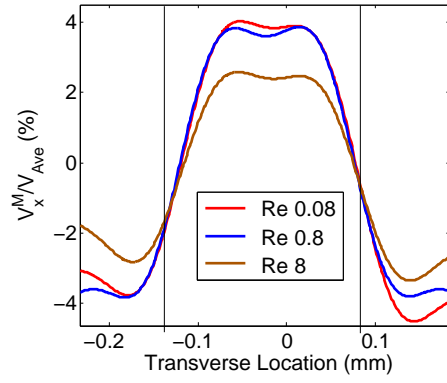


Figure 3.3 Flow at the midplane of the channel. (a) Velocity field for $Re = 0.8$. Mean flow is from bottom to top. Solid line show groove locations. (b) Velocity field for $Re = 0.8$ with constant streamwise velocity of 12mm/s removed. (c) Streamwise velocity along line B-B in (a). (d) Normalized transverse velocity along the line B-B in (a) and (b). The vertical dash lines mark the locations of the groove peaks.

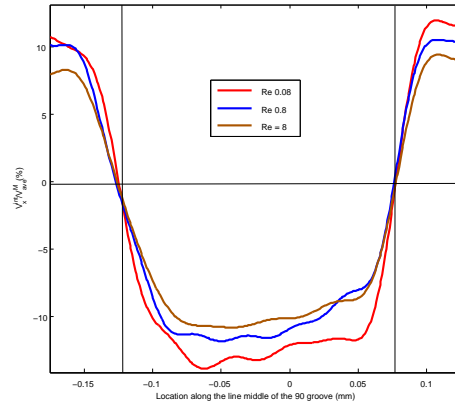
Here, we choose to examine midplane velocities along the line B-B in Figs. 3.3a and 3.3b so that all the points considered are equidistant from the trailing edge of the upstream groove. The streamwise component of midplane velocity, V_y^M , is essentially constant along this line, as shown in Fig. 3.3c; the spatial average of V_y^M along B-B gives V_{ave} . As with the interfacial velocity, the direction of V_x^M/V_{ave} is opposite of that of V_x^I/V_{ave} , which indicates counter-rotating secondary flow. The maximum amplitude of V_x^M/V_{ave} is approximately 75% that of V_x^I/V_{ave} at $Re = 0.08$ and 0.8 , but for $Re = 8$ the maximum amplitude of V_x^M/V_{ave} is only 50% that of V_x^I/V_{ave} .

In order to analyze the effect of the internal angle of the herringbone pattern in generating the transverse velocity in the midplane, microPIV experiments were performed on two other microchannels, one with an internal angle of 90° and the other with an internal angle of 45° . The rest of the dimensions of the channel were the same as the microchannel with an internal angle of 135° . Since, we have the same number of chevrons (6 in number) across the channel, the field of view keeps reducing from 135° through 90° to 45° . Figure. 3.4(a) shows the normalized transverse velocity along the line B-B in Fig. 3.3a. It can be seen that the peak value of the normalized velocity for corresponding Reynolds number drops down from about 15% at Re 0.08 in the 135° mixer to about 4% in the 90° mixer. We observe a similar trend in the normalized interface velocity as shown in Fig. 3.4(b).

Figure 3.5 shows the normalized transverse velocity at the midplane and at interface for a 45° mixer. The peak values of the normalized midplane transverse velocities are even smaller than that for the 90° mixer. However, we see that the normalized interface velocity is higher at Re 8 for the 45° mixer, which is against our intuition. The reason why for a higher value here is due to the error in locating the interface plane accurately. Even a slight variation in locating the interface will move the focal plane by a few microns into the chevron, which would give a higher transverse velocity, and hence a higher normalized velocity.

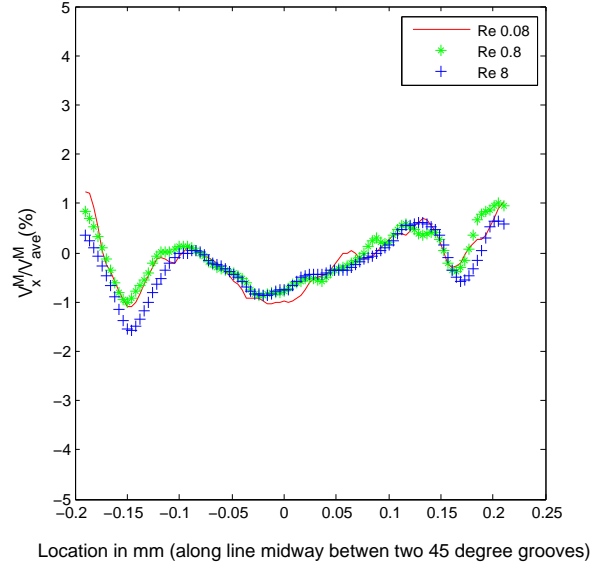


(a) Normalized transverse velocity at midplane

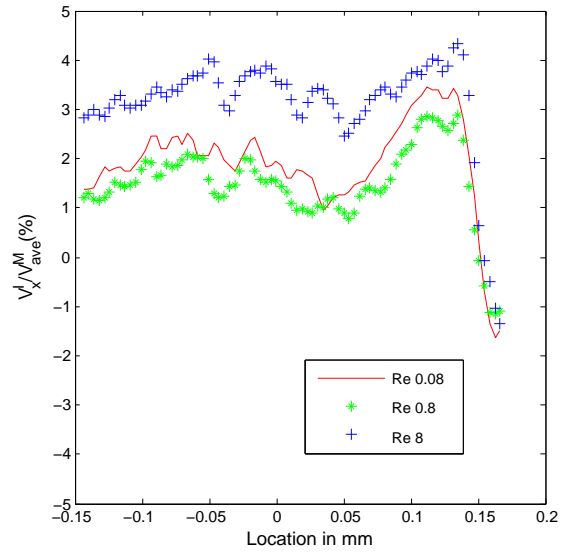


(b) Normalized transverse velocity at Interface

Figure 3.4 The normalized midplane velocities are plotted along the line B-B in Fig. 3.3a, and the normalized interface velocities are plotted along the line A-A in Fig. 3.2a



(a) Normalized transverse velocity at midplane



(b) Normalized transverse velocity at Interface

Figure 3.5 The normalized midplane velocities are plotted along the line B-B in Fig. 3.3a, and the normalized interface velocities are plotted along the line A-A in Fig. 3.2a for 90 degree micromixer

3.5 Conclusions

For steady, pressure-driven flow in a high-aspect ratio channel, oblique surface grooves cause a transverse velocity near the channel wall. At low Reynolds numbers, the influence of this surface velocity generates a strong secondary flow. We found that the transverse velocity changes sign near the chevron peaks both at the groove interface and at the channel midplane, and between these peaks the transverse velocities at the interface and midplane have opposite sign. These results suggest that the flow structure consists of regions of counter-rotating secondary flow separated by stream surfaces that serve as barriers to (non-diffusive) transverse transport. The normalized magnitude of the secondary flow is nearly identical for $Re = 0.08$ and 0.8 , but at $Re = 8$ the inertia of the fluid reduces the normalized effect of the surface grooves on the midplane velocity field.

Due to the high-aspect ratio of the channel cross-section, the velocity field is essentially periodic in the transverse direction. Thus, the herringbone surface pattern establishes a set of parallel counter-rotating regions across the channel, effectively splitting this wide channel into multiple smaller channels. It is expected that the axial variations in the surface pattern will cause splitting and combining of these regions similar to a parallel laminating mixer. We also notice that the transverse velocity generated due to the pattern decreases with the decrease in the internal angles for the chevron. There lies an optimal angle which will give the maximum transverse velocity both at the interface and the midplane. That angle should be chosen for the best performance of this mixer.

CHAPTER 4. Visualization of turbulent reactive mixing in a planar microscale confined impinging-jets reactor

Abstract

Turbulent reactive mixing in a rectangular microscale *confined impinging-jet reactor* (CIJR) was investigated using the pH indicator phenolphthalein in this study for three different jet Reynolds numbers $Re_j = 25, 1000$ and 1500 . Laminar flow regime was observed at $Re_j = 25$ whereas the flow was turbulent at $Re_j = 1000$ and 1500 . An image processing technique was applied to instantaneous images to extract quantitative mixing data by identifying regions with $pH \geq 9.3$ and regions with $pH < 9.3$. The ensemble-averages were computed using these thresholded images to compare mixing performance between different Reynolds numbers. Finally, the spatial auto-correlation fields of the thresholded images fluctuations were evaluated, based on which large-scale turbulent structure were analyzed.

4.1 Introduction

In many chemical process applications, microscale reactors can have superior performance characteristics compared to their conventional large scale counterparts. For example, microscale reactors possess enhanced heat and mass transfer performance due to high surface area to volume ratio [37]. Moreover, characteristic mixing times due to the small volumes of microreactors can be greatly reduced, enabling the control of fast reactions [38, 39]. Common applications of microreactors range from sample preparation for chemical/biological analysis [40, 41] to industrial production of nanoparticles [42, 43].

Nanoparticle production has become a popular area of research over the past decade.

Nanoparticles with uniform size distribution have applications in various areas, such as pesticides, cosmetics and drug delivery [44, 45, 46]. Yet despite their growing popularity, nanoparticles can prove difficult to manufacture with existing technologies. One recently developed nanoparticle manufacturing technique, first proposed by Johnson and Prud’homme [14], *Flash Nano-Precipitation*, is a very promising technique for the synthesis of functional nanoparticles. Two types of microreactors, the *Confined Impinging-Jet Reactor* (CIJR) and *Multi-Inlet Vortex Reactor* (MIVR), have been developed with a particular emphasis on their usefulness in *Flash Nano-Precipitation*.

Rapid mixing and the resulting ‘homogeneity’ of the flow field are essential for the optimum realization of *Flash NanoPrecipitation*. These conditions imply shorter fluid mixing times than particle formation times. Both the CIJR and MIVR have demonstrated the capability to produce such short mixing times and good mixing [14, 43]. Past studies have attempted to characterize the mixing performance and/or hydrodynamics of the flow using various experimental and numerical techniques. Johnson and Prud’homme [43] quantified the mixing performance of their custom designed CIJR by measuring the dimethoxypropane (DMP) produced in the slow reaction in a carefully chosen second order Bourne pair. Note that this technique only provides information on the output of the reactor and provides no data on the flow field or mixing performance within the reactor. For the same reactor geometry, Liu and Fox [47] performed *computational fluid dynamics* (CFD) simulations and obtained satisfactory agreement with Johnson and Prud’homme’s experimental results. The same techniques were also applied to investigating the MIVR [13]. Once again the simulation results displayed satisfactory agreement with the experimental data. More recently, Cheng et al. [48] and Liu et al. [49] employed *microscopic particle image velocimetry* (microPIV) to directly measure the turbulent velocity field in the MIVR and the planar CIJR, respectively, for comparisons with CFD simulations. The comparisons turned out quite well.

To complement the previous studies, in the present research we utilize a non-intrusive technique for visualizing and quantifying turbulent reactive mixing in a confined impinging jet microreactor. This flow visualization technique is simple and inexpensive, but as we shall

demonstrate, quite effective. By utilizing the pH indicating dye phenolphthalein, this technique provides striking visualization of turbulent reactive mixing in the CIJR and can also provide a quantitative measure of fluid mixing and turbulent structure characteristics. In the following sections, the fabrication of the reactor, the experimental setup and procedures, and an image processing technique for quantifying reactive mixing will be described, followed by results and discussions from which some conclusions will be drawn.

4.2 Reactor geometry and Flow-delivery system

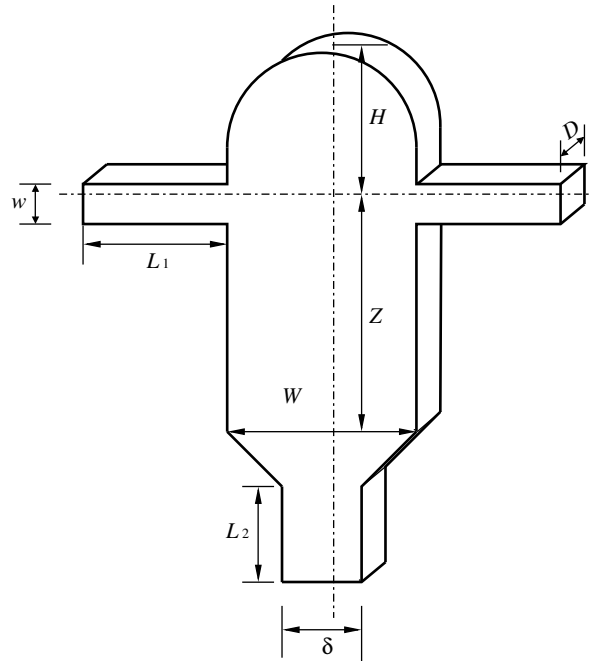


Figure 4.1 Geometry of the planar confined impinging jet reactor

Unlike the axisymmetric cylindrical CIJR design used in some previous studies [47, 43], the reactor geometry in the present work is rectangular in cross-section so as to avoid the optical distortion effects resulting from imaging through curved surfaces. A drawing of the reactor used in this study is shown in Fig. 4.1. The resulting three-plate reactor is similar to the one described by Liu et al. [49], where the fabrication technique is discussed in detail. For brevity, only a brief description of the fabrication is presented here. In Liu et al. [49], the reactor shape was carved out by *electrical discharge machining* (EDM) on a stainless steel plate.

In the present work, the same stainless steel plate has been used as in Liu et al. [49], but the top and bottom walls have been replaced by PlexiglasTM plates due to the high pressure provided by specially designed clamps, which may easily break glass slides. The purpose of these clamps is to strengthen the seal between the PlexiglasTM plates and the stainless steel and prevent leaks. In addition to the clamps, thin pieces of Parafilm (Pechiney Plastic Packaging Inc.) with the shape of the channel cut out are also inserted between the PlexiglasTM plates and the stainless steel plate to improve sealing. Any leakage issues at high Reynolds numbers have been eliminated this way while still leaving the flexibility of disassembling the reactor for cleaning whenever needed. However, since the thickness of Parafilm (0.127 mm) is slightly different from that of the adhesive film used by Liu et al. [49], the depth of the reactor (denoted by D in Fig. 4.1) is 1.12 mm compared to 0.92 mm in the work of Liu et al. [49]. The width of the impinging jets, w , is 0.5 mm. The chamber width W , height H , length Z and the outlet width δ have scaled values $W/w = 4.76$, $H = 0.8W$, $Z = 1.2W$, and $\delta = 2w$ respectively. The length-to-width ratio of the inlets is $L_1/w = 20$ and the length-to-width ratio of the outlet is also $L_2/\delta = 20$.

A schematic of the flow-delivery system is shown in the upper portion of Fig. 4.2. Fluid is delivered to the two inlets of the reactor by a dual-syringe pump (model KDS210P, KD Scientific Inc.). Two 60 ml syringes, one containing a sodium hydroxide solution and one containing a hydrochloric acid solution, are placed on the rack of the syringe pump and attached with flexible tubings (C-flex tubing, Cole-Parmer Instrument Co.) to the inlets of the reactor. The mixed fluid exits the reactor through another flexible tube and is collected in a waste bottle.

4.3 Experimental Technique and Apparatus

4.3.1 Technique Overview

Numerous experimental methods have been developed to visualize turbulent flow features and to either quantitatively or qualitatively characterize mixing performance. Methods for characterizing mixing performance typically fall into one of two categories. The first category

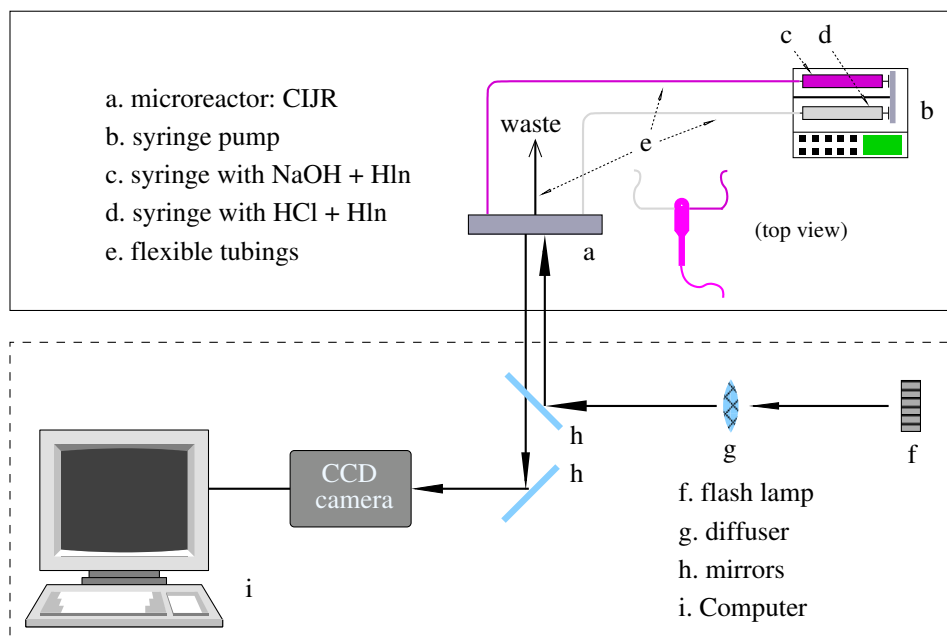


Figure 4.2 Schematic of experimental setup

involves mixing-sensitive processes [43], such as second-order competitive/consecutive chemical reactions [50], and the second category includes dye-based visualization techniques [18]. The first category has the advantage of easy implementation and is typically used as “chemical ruler” for the micromixing time due to well defined reaction kinetics. However, these techniques have the disadvantage of only measuring the output from reactor and provide no information on mixing and turbulence details within the reactor. In the second category, *laser induced fluorescence* (LIF) with its capability of providing both instantaneous flow visualization snapshots as well as quantitative statistical data on mixing and reaction processes is perhaps the most widely used [51, 52]. However, LIF inevitably requires rather expensive equipment, such as lasers, sensitive cameras, triggering and timing units, etc. [53] From this point of view, a simpler technique using non-fluorescent dyes is an attractive alternative that could potentially reduce experimental cost significantly and provide more researchers with access to the technique, while still providing valuable insights on the mixing performance and allowing turbulent structures to be visualized. For this reason, a number of researchers have found phenolphthalein, a common pH indicator, particularly useful in turbulent mixing stud-

ies for numerous reasons [15, 16, 17, 18, 19]. First, phenolphthalein is widely available and inexpensive. Second, phenolphthalein reacts to changes in pH so rapidly that the process is usually considered diffusion-limited [54]. Third, the pink or purple product created within a certain pH range can be easily distinguished from the colorless reactants [55].

Although the mixing extent can be quantified by the amount of phenolphthalein reacted in pure base-dye reaction [15, 18], the protocol established by Abarca and Clement [53] is employed here. Non-premixed binary mixing can be mathematically described by mixture fraction (or in this case equal to mass fraction), ξ . The pH at any location in the reactor can be related to this quantity. For our system, complete mixing corresponds to a mixture fraction $\xi = 0.5$ and a pH of 9.3. By thresholding the local values by using an image processing technique, the mixing performance can be quantitatively evaluated.

4.3.2 Experimental Setup and Procedure

The reaction solutions are prepared such that the solutes are dissolved in a solvent mixture consisting of 30% ethyl alcohol and 70% deionized water by volume. The alcohol is added to increase the solubility of phenolphthalein and thus allow for a greater concentration of phenolphthalein to be dissolved than would be possible in pure deionized water. The higher concentration of phenolphthalein is necessary to increase the contrast of the images so the phenolphthalein can be clearly imaged. After the solution is prepared, 30ml of phenolphthalein stock solution (abbreviated Hln in schematic) is then added to 1L of the solutions for both inlet streams. The phenolphthalein stock solution consists of 3.1832 g of phenolphthalein dissolved in 100 ml of ethyl alcohol. Dissolving phenolphthalein in both inlet streams was done to minimize density differences between the two streams, and more importantly, to reduce the two factors (pH and concentration of phenolphthalein) to one (only local pH) that influence the visibility of phenolphthalein [53] since the concentration of phenolphthalein will be constant throughout the reaction chamber. In the prepared solutions, phenolphthalein is saturated and the precipitated powders are filtered out to obtain precipitate free solutions after the solutions settle for two hours. The resulting base solution has a pH of 11 and the pH of the acid solution

is 3. The solutions are then degassed to minimize the possibility of bubbles forming in the reactor chamber and in the inlet.

The flow visualization system is shown in Fig. 4.2. While the flow-delivery system has been described previously, the imaging components, highlighted by the dashed box, are described here. The light path in this system is denoted by the solid arrows. The main body of an inverted biological microscope (model Eclipse T300 Inverted Microscope, Nikon Inc.) is omitted here for simplicity. In order to freeze the turbulent fluid motion and provide an instantaneous snapshot of the flow field, a pulsed light source (model PAX-1001-4 10Watt Precision Aligned Pulsed Xenon light source, Perkin Elmer Inc.), labeled flash lamp in the figure, with extremely short pulse duration ($5 \mu\text{s}$) is used to provide the illumination. For such a short pulse duration, a fluid element moving at 4.5 m/s , which is the maximum velocity in these experiments, travels only $22.5 \mu\text{s}$, demonstrating the effectiveness of the flash lamp in freezing the fluid motion. The flash lamp is powered by a power supply (model EFB Filtered DC power supply, Epsco Inc.) and the light intensity can be varied by adjusting the voltage. The non-uniformity of the light from the flash lamp is reduced by using a diffuser (10° , model 10DKIT-C2 Light Shaping Diffuser[®], Newport Corp.) to generate a visually uniform field of view. The instantaneous flow field images are recorded by a color CCD camera (model Stingray F-080C, Allied Vision Technologies GmbH), digitized and stored on a computer. Both the flash lamp and CCD camera are triggered by a pulse generator (model DG535 4-channel Digital Delay/Pulse Generator, Stanford Research Systems Inc.), operating at a frequency of 15 Hz providing synchronization so that each captured image is illuminated by a single pulse of the flash lamp. A 2X objective coupled with a 0.45X video coupler gives a broad field of view such that the entire reactor chamber can be imaged. The experiments are carried out for three different jet Reynolds numbers, 25, 1000 and 1500, as defined in $\text{Re}_j = u_{\text{jet}} D_h / \nu$, where u_{jet} is the mean velocity of the inlet channels, D_h the hydraulic diameter of the inlet channels and ν is the kinematic viscosity. Over 5000 images are collected for each of these Reynolds numbers.

4.3.3 Image Processing Technique

As will be seen in the results section, this technique can provide striking qualitative visualization of the turbulent reactive mixing in the reactor chamber. However, extracting quantitative data is more challenging. Phenolphthalein is clear at acidic and neutral pH, but turns a bright pink at basic pH. This color change in phenolphthalein is a sharp transition. This makes it difficult to simply attempt to calibrate the observed image intensity with pH, since the dynamic range of the signal is small. Instead, a more promising technique for extracting quantitative mixing data from the phenolphthalein images is to recognize that transition from clear to pink in the solutions used in these experiments occurs at a pH of 9.3, identify which regions of the flow field are clear and pink, and consequently, in each instantaneous image identify regions pH less than 9.3 and regions with pH greater than or equal to 9.3. This pH is also the pH at the outlet of reactor where the two solutions are completely mixed. The ensemble of images thresholded in this manner can be used to determine the probability of local pH being equal to or greater than 9.3 at various locations throughout the flow field. The seemingly easiest way of doing this is to convert the color images to gray scale and carry out the thresholding on the gray scale images. However, this technique was rejected after a few attempts since it failed to identify the interface between colored and uncolored region even when applied to the laminar case where there exists a sharp interface between the colorless and colored regions because of the low contrast in the gray scale images. One might argue this problem can be readily resolved by normalizing the images using images containing only uncolored phenolphthalein solutions, but this was found to be not of much help. However, a completely digital image processing method has been adopted in this work that is not only easy to perform but also successfully identifies colored and uncolored regions. Similar to the “gray-scale” idea, in this image processing technique, the images are first converted into *CIELAB* color space, where the three coordinates L^* , a^* and b^* represent the luminosity (or simply brightness), the positive component (consisting mainly of red hues) and the negative component (consisting mainly of green hues), respectively [56]. By only computing the a^* and b^* values, the purple (colored phenolphthalein) and green (uncolored phenolphthalein) regions, which are the prin-

ple colors in the collected images, can be successfully separated. In other words, dark and light colors are treated identically if this L value is ignored. The steps involved in this process are described below:

1. find characteristic a^* , b^* values from the average calibration image, where the reactor is filled with completely mixed solution with a pH of 9.3, for green and purple, denoted by a_{cg}^* , a_{cp}^* , b_{cg}^* and b_{cp}^* respectively;
2. evaluate for each point in each image the distances from the two characteristic values,

$$d_{i,green} = \sqrt{(a_i^* - a_{cg}^*)^2 + (b_i^* - b_{cg}^*)^2}, \quad (4.1)$$

$$d_{i,purple} = \sqrt{(a_i^* - a_{cp}^*)^2 + (b_i^* - b_{cp}^*)^2}; \quad (4.2)$$

3. assign the point a tag *purple* if $d_{i,green} > d_{i,purple}$, but a tag *green* otherwise;
4. let the intensity of a point $I_i = 1$ if the tag is *purple* and $I_i = 0$ if it is *green*.

This process is performed by utilizing the *Image Processing Toolbox* in Matlab[®], which results in a set of binary images. Example thresholded images created using this technique are presented in the next section.

4.4 Results and Discussion

4.4.1 Instantaneous Images

Three example instantaneous images for $Re_j = 25$ are shown in Fig. 4.3. In these images (and all images presented), the left inlet stream is acidic (and hence colorless), and the right inlet stream is basic (and hence pink). The two inlet streams impinge in the center of the reactor, and the flow is turned downwards towards the outlet. At this Reynolds number, the flow is laminar and steady and so the interface between the fluid of the two inlet streams remains sharp as they convect towards the outlet. The only mixing between the two streams is due to diffusion. The pink fluid observed above the inlets in the reactor is due to two



Figure 4.3 Sample original instantaneous images for $Re_j = 25$.

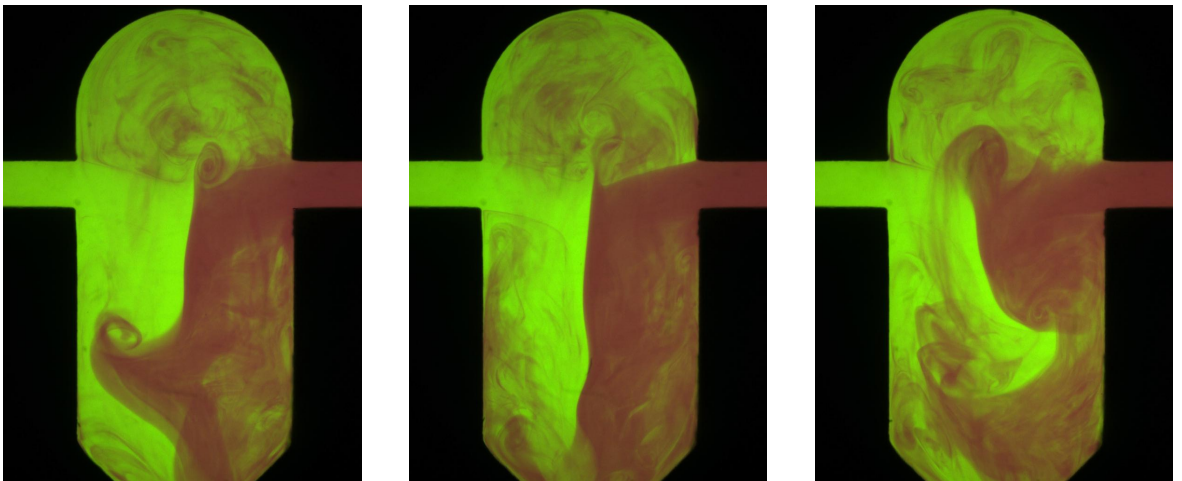


Figure 4.4 Sample original instantaneous images for $Re_j = 1000$.

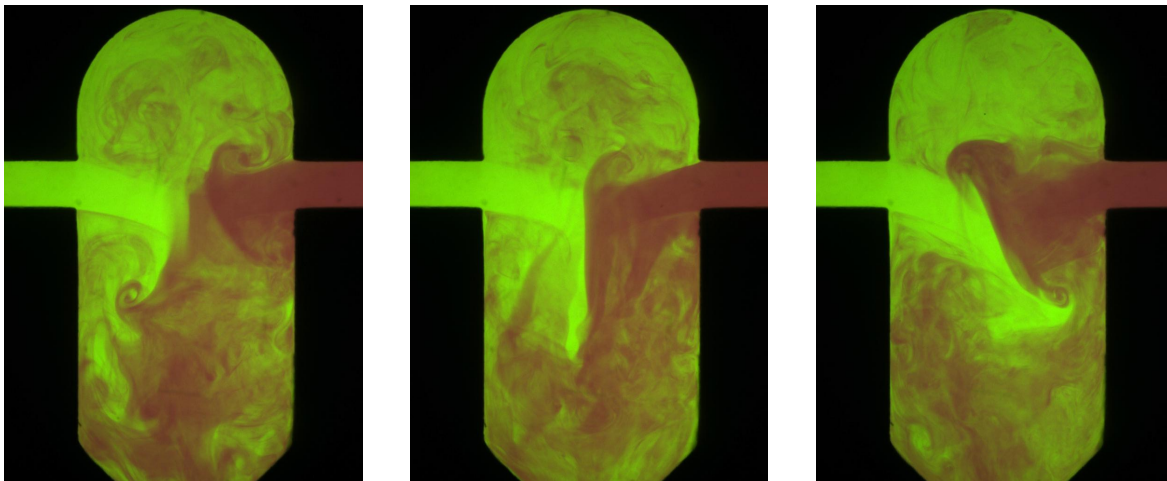


Figure 4.5 Sample original instantaneous images for $Re_j = 1500$.

counter-rotating recirculation eddies that appear in this region (these recirculation eddies were observed in both CFD simulations and microPIV measurements as reported by Liu et al. [49]). Three instantaneous images for $Re_j = 1000$ are shown in Fig. 4.4. Several features of the flow and mixing performance are suggested by these images. First, the inlet streams are not fully mixed or reacted when they exit the reactor. The fully reacted inlet fluids have a pH of 9.3, as pointed out previously, and thus produce a pink color in the phenolphthalein. Next, the highly convoluted interfaces between the colored and uncolored regions are indicative of the flow in the reactor being turbulent. Swirling patterns suggest the presence of large-scale turbulent vortices. Finally, the varying orientation of the impingement plane between the two inlet streams indicates an unsteady flapping motion of this impingement plane (a finding consistent with the *large eddy simulation* (LES) and *direct numerical simulation* (DNS) results of Icardi et al. [57, 58] for an axisymmetric impinging jets reactor). Fig. 4.5 shows three instantaneous images for $Re_j = 1500$. The flow at this Reynolds number is also turbulent and unsteady, with the turbulent features and oblique flapping of the impingement plane even more pronounced than at $Re_j = 1000$. The images also suggest improved mixing performance compared to $Re_j = 1000$. For example, in the first two panels of Fig. 4.5, broad swatches of clear fluid from the left inlet jet are observed to penetrate nearly to the outlet of the reactor, but this

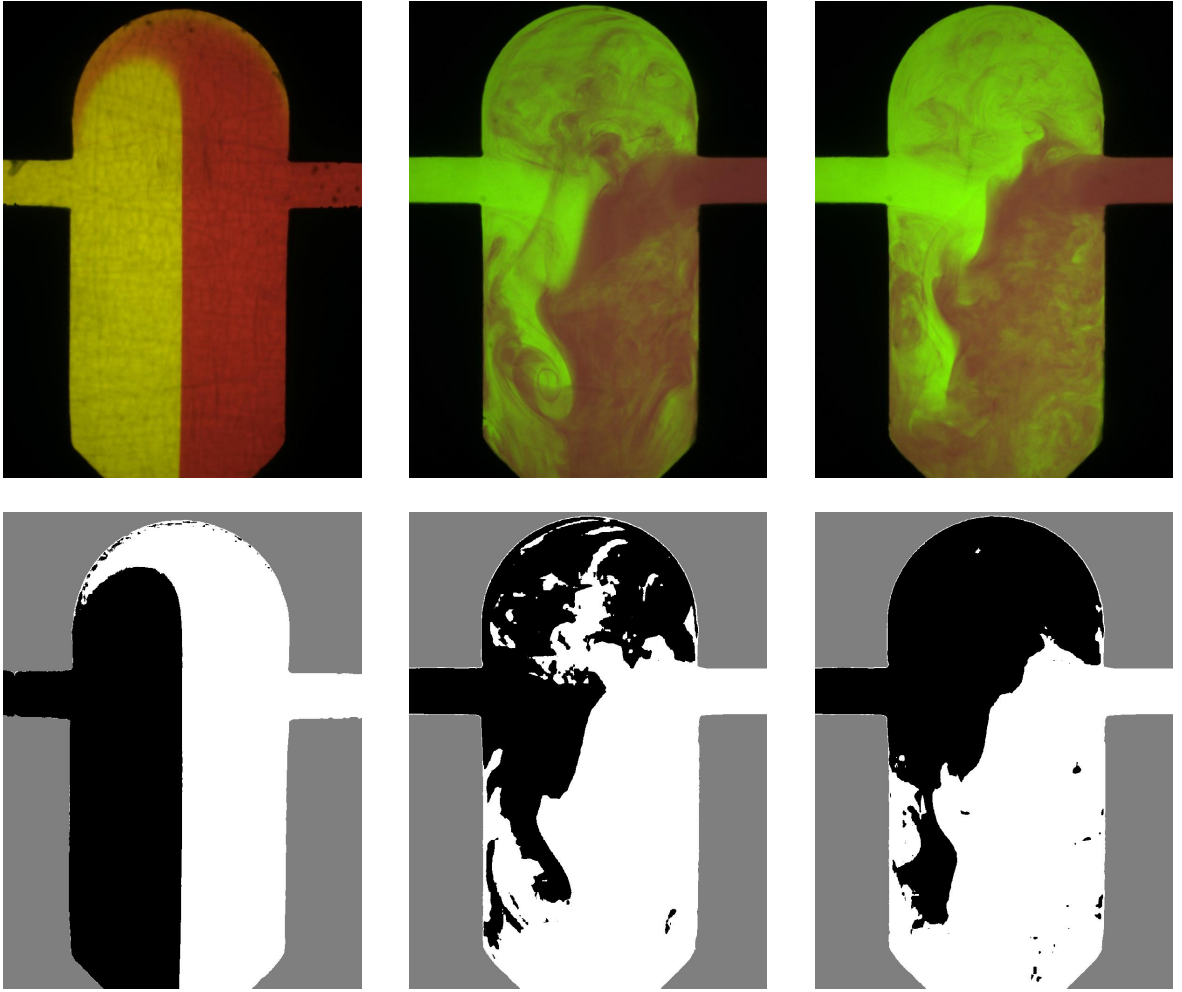


Figure 4.6 Sample processed instantaneous images (bottom) for $Re_j = 25$ (left), $Re_j = 1000$ (middle) and $Re_j = 1500$ (right).

penetration is reduced at $Re_j = 1500$.

4.4.2 Image Thresholding and Statistical Analysis

Example thresholded images created using the image processing technique described in Section 4.3.3 are shown in Fig. 4.6 for $Re_j = 25$, 1000 and 1500. In these images, the colored and uncolored phenolphthalein regions have been identified, with the colored regions tagged with a value of 1 and the uncolored regions with a value of 0. The resulting images identify regions where the local pH is less than 9.3 (value of zero) or greater than or equal to 9.3 (value

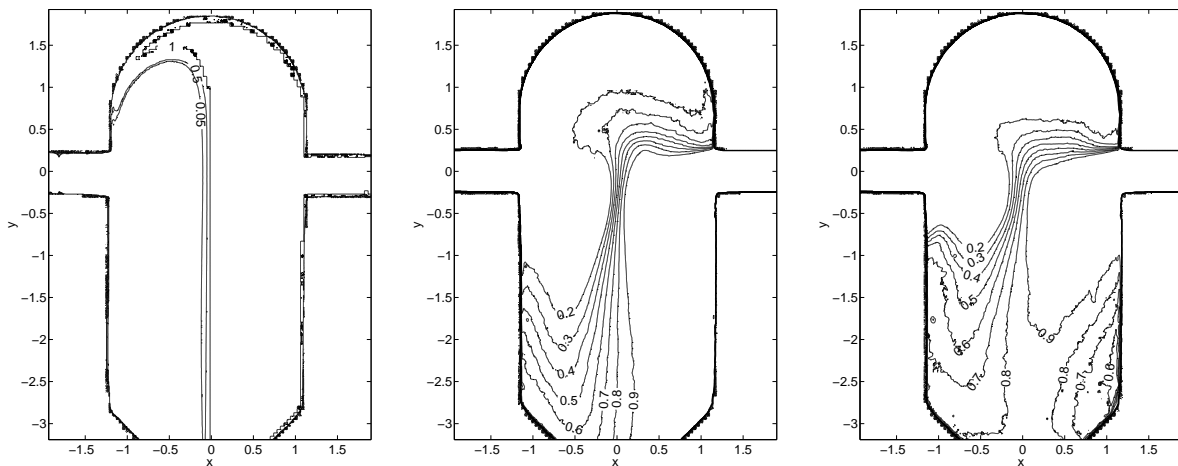


Figure 4.7 Contours of means for $Re_j = 25$ (left), $Re_j = 1000$ (middle) and $Re_j = 1500$ (right).

of one).

This thresholding was performed for each of the over 5000 realizations collected for each Reynolds number. Ensemble averages using these thresholded instantaneous realizations for all three Reynolds numbers investigated are shown in Fig. 4.7, and presented in the form of contour plots. The value at each location in the ensemble average contour plots falls between zero and one, and this value represents the probability at each point in the flow field that the local pH is greater than or equal to 9.3 in one instantaneous realization. Recall that for fully mixed and reacted inlet fluid, the pH is 9.3, and would thus result in a thresholded image value of 1. Thus, a flow in the reactor resulting in complete mixing and reaction within the reactor chamber would have fluid leaving the reactor with an ensemble-averaged value of one all across the exit of the reactor. Thus, the ensemble-average shown in Fig. 4.7 can provide a means of comparing mixing performance at the different Reynolds numbers investigated.

The first panel in Fig. 4.7 shows the ensemble-average of the thresholded images for $Re_j = 25$. The results are nearly binary, with the left side of the flow field having a value of zero and the right side having a value of one. Only a thin region in the center of the reactor has intermediate values, indicating the steady state laminar nature of the flow at this Reynolds

number. As expected, mixing performance is poor. The middle panel of Fig. 4.7 shows the ensemble-average of the thresholded images for $Re_j = 1000$. Here, the improved mixing performance due to the presence of turbulence is readily observed. At the outlet of the reactor (below $y = -3$ mm), the exiting fluid does not have a nearly uniform binary value of 0 or 1, as it did in the $Re_j = 25$ case. Instead, the exiting fluid has ensemble-averaged values ranging from 0.6 to 1.0. Also, on the left side of the reactor, pure inlet fluid does not penetrate to the outlet of the reactor, as in the $Re_j = 25$ case, but instead penetrates to only $y = -1.5$ mm before it begins reacting with fluid from the other inlet stream. Finally, the last panel in Fig. 4.7 shows the ensemble-average of the thresholded images for $Re_j = 1500$. Here, the contours suggest better mixing performance than for $Re_j = 1000$ (as would be expected). There are several indications of this. First, the pure inlet fluid on the left side of the reactor is less able to penetrate far into the reactor before reacting with basic fluid, penetrating to only $y = -0.75$ mm. Moreover, at the exit of the reactor the ensemble-average value is nearly uniform at 0.8. The fluid is still not fully mixed and reacted, but this uniform value indicates that fluid from each of the inlet jets is nearly equally distributed at the reactor exit. Also, unlike the $Re_j = 25$ and $Re_j = 1000$ cases, none of the pure inlet fluid from the right inlet seemingly passes through the reactor before encountering acidic fluid, as below $y = -2.0$ mm, none of the contours have a value greater than 0.9. Even the regions of 0.6 and 0.7 ensemble-averaged value in the lower right side of the reactor are indicative of the superior mixing at this Reynolds number, as they indicate some of the fluid from the left inlet must be advected to this far corner of the reactor.

4.4.3 Spatial Correlations and Large-Scale Structures

The ensembles of instantaneous images can also be used to investigate the property and behavior of large-scale turbulent structures by calculating spatial auto-correlations of the thresholded images. Let $I(x, y)$ represent the ensemble-average of the thresholded images, as shown in Fig. 4.7. If $i(x, y)$ represents an instantaneous realization of the thresholded image ensemble, then for each instantaneous image, an instantaneous fluctuation, $i'(x, y)$, can be defined as $i'(x, y) = i(x, y) - I(x, y)$. Then the two-point spatial auto-correlation coefficient of i' can

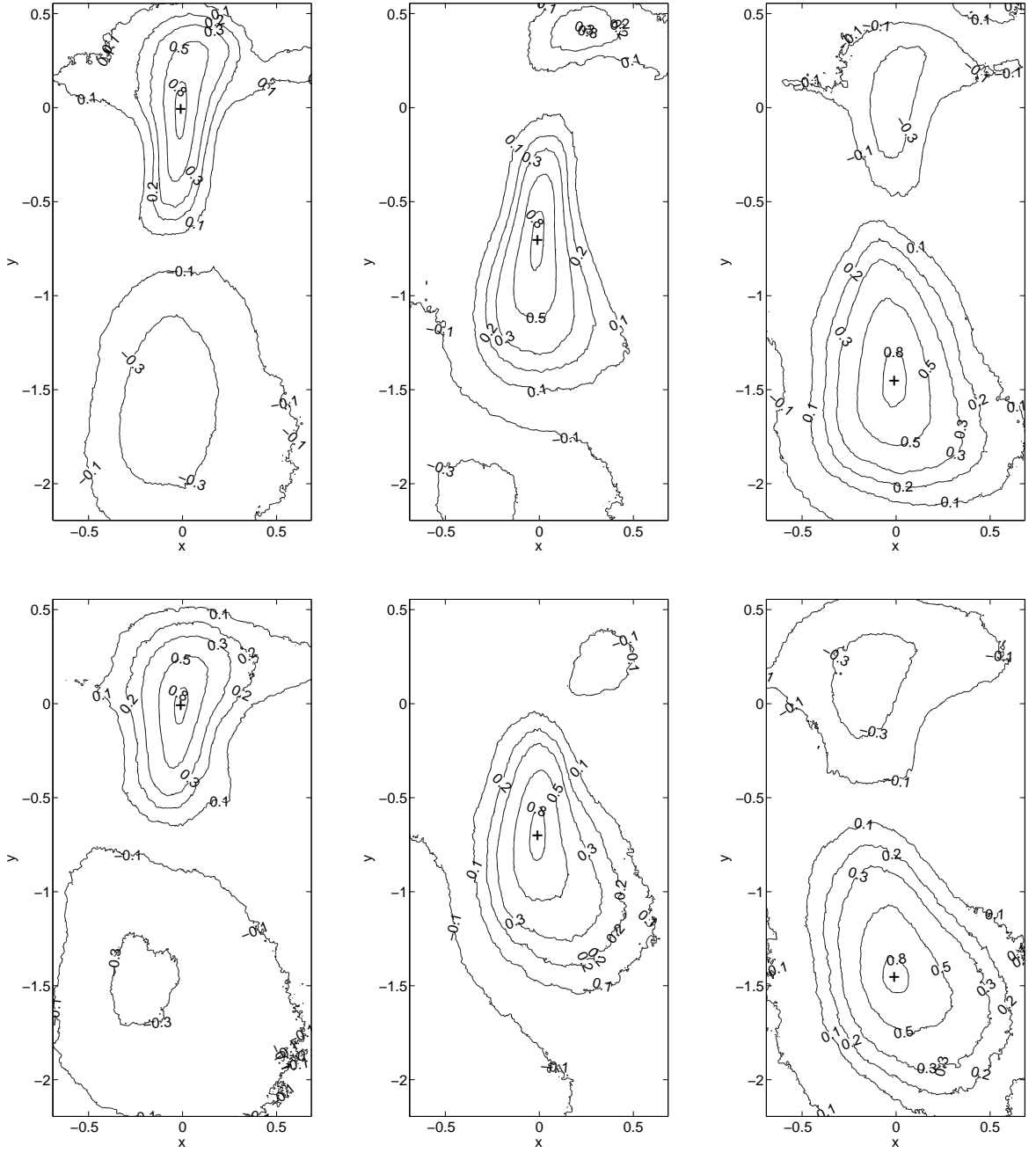


Figure 4.8 Contours of two-point spatial auto-correlation coefficient for $Re_j = 1000$ (top), $Re_j = 1500$ (bottom) at three different locations (marked with the '+' sign)

be computed as,

$$R(x, y; X, Y) = \frac{\langle i'(x, y)i'(X, Y) \rangle}{\sqrt{\langle i'^2(x, y) \rangle \langle i'^2(X, Y) \rangle}}, \quad (4.3)$$

where R is the correlation coefficient, (X, Y) is the basis point about which the spatial correlation is measured and (x, y) is a displacement from the point (X, Y) . The spatial auto-correlation of i' for three different measurement locations in the flow field for $\text{Re}_j = 1000$ and 1500 are presented in Fig. 4.8. The three measurement locations are all along vertical center-line of the reactor. The first point is at the same vertical location as the centerlines of the two inlet channels and roughly corresponds to the stagnation point in the flow. This location is denoted as $y = 0.0$ mm. The other two measurement locations are 0.7 mm and 1.5 mm below this location. The top three panels in Fig. 4.8 are the auto-correlation fields around the three measurement locations for $\text{Re}_j = 1000$. In each panel, the location of the basis point is shown by the '+' symbol. One interesting feature of these correlations is that the area of the correlation peaks becomes larger as downstream distance increases. Since the size of the correlation peaks is expected to be related to the size of large-scale turbulent structures in the flow, this suggests that the turbulent structures become larger as the flow convects downstream, a finding consistent with large-scale structure behavior in turbulent shear flows [51]. Also, at each measurement location, the positive auto-correlation peak is accompanied by a weakly negatively correlated region either upstream or downstream of the measurement location. This behavior is due to the unsteady oblique flapping of the interface between the two incoming streams. Because of this oblique flapping, if one location along the reactor has colored phenolphthalein, then locations above or below this location are likely to have uncolored dye, resulting in the observed anti-correlation.

The bottom three panels in Fig. 4.8 are the auto-correlation fields around the three measurement locations for $\text{Re}_j = 1500$. The features of the correlations are similar to those observed for $\text{Re}_j = 1000$ indicating similar flow behavior.

4.5 Conclusions

In the presented work, turbulent reactive mixing in a rectangular *confined impinging-jet microreactor* was investigated using the pH indicator phenolphthalein. The experiments were performed for three different inlet jets Reynolds numbers $Re_j = 25, 1000$ and 1500 . The visualizations show the flow is laminar at $Re_j = 25$ and turbulent at $Re_j = 1000$ and 1500 . The visualizations suggest an unsteady motion of the impingement plane consisting of an interface that obliquely rocks back and forth. A technique was then described for extracting quantitative mixing data from the instantaneous images by using image processing to identify regions in the flow field with pH greater than or equal to 9.3 and regions with pH less than 9.3. The thresholded images were then ensemble averaged to yield pH probability fields. The ensemble-averaged images indicate poor mixing performance for $Re_j = 25$, and better mixing performance for $Re_j = 1000$, and further improved mixing performance for $Re_j = 1500$. However, even at $Re_j = 1500$ complete mixing and reaction was not observed at the outlets.

Finally, spatial auto-correlations of the thresholded images fluctuations were calculated. The correlations suggested that large-scale turbulent structures grew as they convected towards the reactor outlet and provided further evidence of oblique flapping of the impingement zone.

CHAPTER 5. Measurements of Turbulent Velocity Statistics in a Microscale Rectangular Confined Impinging Jets Reactor

Abstract

Microscale chemical reactors capable of operating in the turbulent flow regime, such as confined impinging jets reactors (CIJR), offer many advantages for rapid chemical processing at the microscale. One application where these reactors are used is flash nanoprecipitation a method for producing functional nanoparticles. Because these reactors often operate in a flow regime just beyond transition to turbulence, modeling flows in these reactors can be problematic. With high-performance computational power becoming more affordable, large eddy simulation (LES) has become a viable option. However, validation of computational fluid dynamics models (CFD) like LES requires detailed and accurate experimental data, the availability of which has been very limited for turbulent microscale flows.

5.1 Introduction

The use of nanoparticles in various applications is becoming increasingly commonplace. One particular area where nanoparticles can be transformative is the pharmaceutical industry. Here, nanoparticles may be used in cancer treatment, wherein the nanoparticles carrying the drug are coated with ligands which attach to the specific cells found in cancer tumors, allowing for the targeting of specific cells. Other nanoparticles applicaiton areas include cosmetics, pesticides, and paints [11, 12]. One of popular methods of making this nanoparticles is by means of flash nanoprecipitation. In this process, taking an example of drug embedded nanoparticles, two streams of liquid are directed towards each other in a very small region. One of the

streams contains the medicine (hydrophobic) and polymers dissolved in it. The other stream contains an anti-solvent (pure water). When the two streams collide, the medicine precipitates out to avoid the water molecules and the polymers self-assemble around the medicinal core, for the nanoparticles. Flash nanoprecipitation has been demonstrated to work best in Multi-inlet vortex reactor and confined impinging jets reactor [13, 14]. The size distribution of the nanoparticles depends on the turbulence generated by the colliding jets and the mixing time. The presented research focuses on investigating the turbulent flowfield in the CIJR.

Johnson and Prud'homme [59] did a detailed review of the previous literature, which was basically for the mixing at low Reynolds number. They further did a thorough investigation of various configurations of the Confined Impinging Jets mixer and found the micromixing timescale on the order of few milliseconds. In flow in the inlets of the CIJR is laminar, but becomes turbulent after impinging inside the reactor. This process creates a highly intense region of the turbulent dissipation inside the reactor, such that most of the process streams pass through this region [59, 60]. The highly dissipated region is created because of the kinetic energy of the inlet jets are converted into turbulent motions after impinging and redirecting the flow in a small region.

CFD can be used a very useful tool in modeling and analysis of these processes. Detailed computational studies of micromixing (DQMOM-IEM) in a CIJR with a fourth Bourne reaction system have been performed by Liu and Fox [47], which successfully reproduced the experimentally measured outlet conversion. Gavi et al. [61] performed CFD simulation in an axisymmetric confined impinging jets reactor. However, the lack of detailed experimental data for the rectangular CIJR makes it hard to validate the CFD models. MicroPIV technique has been very promising in obtaining detailed flow physics of turbulent flows. Initial microPIV experiments were conducted by Liu et al. [7] in the planar CIJR for Reynolds' number up to 1000 by using a gearpump to deliver the fluid, and compared them to the RANS simulation. They found reasonable agreement between the experiment and simulation for the mean flow-field, and captured the trend of the turbulent kinetic energy. A study to calculate the energy dissipation and effect of the unequal flow was performed by Siddiqui et al. [60] on an axisym-

metric CIJR. They reported that the operation of the CIJR was very robust to the changes in the inflow rate for upto 30% difference in the inlet flows. In the present work, microscopic particle image velocimetry (microPIV) was employed on a planar CIJR to obtain instantaneous velocity fields for jet Reynolds numbers of 200, 1000 and 1500, corresponding to the completely laminar, the transition from laminar to turbulent, and the fully turbulent regimes, respectively, in the reaction zone. For each Reynolds number, at least 1500 instantaneous particle image realizations were collected to analyze the flow fields and calculate pointwise and spatial turbulence statistics.

5.2 Device Fabrication

The usage of Poly Dimethoxy siloxane(PDMS) to fabricate microfluidic devices is a well established procedure [32, 31, 6]. However, due to the elastic nature of PDMS, in a device such as the confined impinging jets reactor, the high pressures needed to generate high flow rates can deform the device and can even rupture seals. Therefore, in the present research it was decided to fabricate the device using electrical discharge machining(EDM) [7]. EDM is a manufacturing process wherein a desired two dimensional shape is obtained by using electrical discharge. Material is removed from the workpiece by a series of rapidly recurring current discharges between two electrodes, separated by a dielectric liquid. The workpiece acts as one electrode and the tool acts as the other electrode. The geometry thus obtained is very accurate with a smooth surface finish.

The device was fabricated from a stainless steel plate which was 0.87mm thick. The geometry of the device is as shown in Fig. 5.1. The width of the two inlet streams are $w = 0.5\text{mm}$. The other dimensions $W, L1, L2, H$ and Z are related to the jet width by the relations $W = 4.76w$, $L1 = 60w$, $L2 = 20d$, $H = 0.8W$ and $Z = 1.2W$. The device was sealed by glueing two glass slides on either side of the stainless steel plate using a double-sided silicon transfer adhesive film (Adhesive Applications, MA). The thickness of the adhesive film as provided by the manufacturer was 0.02504mm. This brought the overall depth of the device to 0.92mm. One of the glass slides had three pre-drilled holes to provide inlet and outlet ports

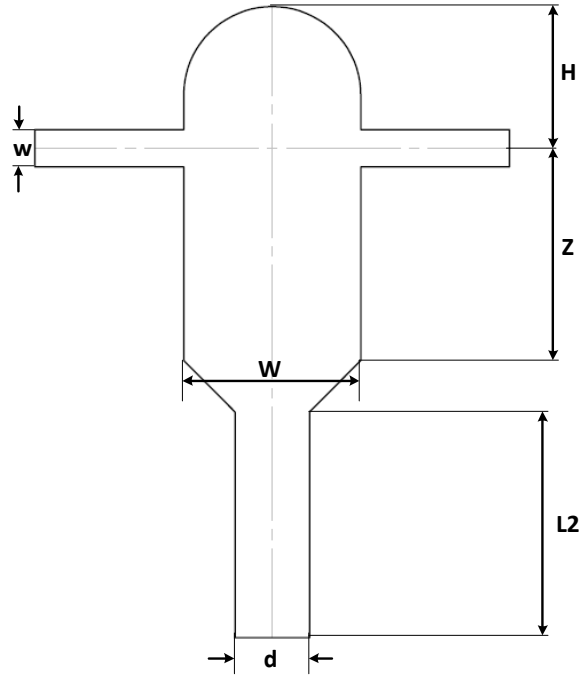


Figure 5.1 Geometry of CIJR

for the device. The inlet and outlet ports were bonded to the glass slide using commercial RTV sealant. This device fabrication procedure provided optical access to the interior of the CIJR which was crucial for the microPIV measurements and resulted in an overall thickness of the reactor that was complimentary to the working distance of the $4\times$ objective used in this case.

5.3 Methodology

Particle Image Velocimetry [62] is a well-established experiment technique for studying turbulent flow fields, and the guidelines for improving the performance of a PIV system have been investigated and formulated by Keane and Adrian [63]. Microscopic particle image velocimetry (microPIV) is an extension of PIV suitable for studying microscale fluid flow. The first application of the microPIV was demonstrated by Santiago et al. [4]. The primary difference of a microPIV system from a traditional PIV system is in the method of illumination. In a traditional PIV system, the flow is illuminated by means of a thin laser sheet. By doing so,

only the particles that are illuminated by the laser sheet are imaged and contribute to the measured velocity. However, in microPIV it is not possible to use a laser sheet illumination. Instead, the entire volume of a flow field is illuminated in a microPIV system. As a result, in the microPIV system all the particles that are in the field of view contribute to the captured images, either by forming discrete particle images or by contributing to a background glow [24]. The measurement volume in a microPIV experiment is described by the Depth of Correlation ($2Z_{corr}$) [36, 24], a parameter which defines the distance from the object plane beyond which the particles will not significantly contribute to the measured velocity. This parameter is a function of focal number, $f^\#$, diameter of the particle d_p , magnification of the objective M and the wavelength of the light emitted by the seed particles λ . The depth of correlation can be found by using [24]

$$2Z_{corr} = 2 \left[\frac{1 - \sqrt{\varepsilon}}{\sqrt{\varepsilon}} \left(f^{\#2} d_p^2 + \frac{5.95(M+1)^2 \lambda^2 f^{\#4}}{M^2} \right) \right]^{1/2} \quad (5.1)$$

where $\varepsilon = 0.01$. For low magnification, $f^\#$ can be related to the numerical aperture NA by

$$f^\# = \frac{1}{2NA}$$

In the microPIV experiments, time separation between successive images is chosen such that the particles move approximately a one fourth of interrogation window length [64, 65]. To ensure successful implementation of the cross-correlation technique, between 5 and 15 seed particles should be present in each interrogation volume [63]. In the present work the flow was seeded such that, on average 9 seed particles were in each interrogation volume.

5.4 Experimental Setup and Procedure

The experimental setup for the microPIV experiments presented here is shown in Fig. 5.2. A high pressure syringe pump (KD Scientific) was used to deliver the particle solution into the inlet streams of the CIJR through flexible Tygon tubing (Cole-Palmer). One limitation of using a syringe pump is the finite volume of particle solution that can be dispensed into the microreactor from a single syringe. Hence, during the course of collecting the experimental

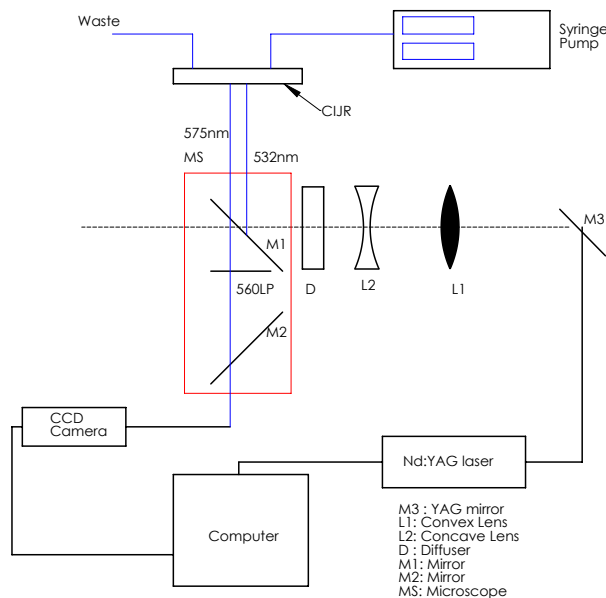


Figure 5.2 Schematic of the experimental Setup

data, the syringes had to be refilled many times. To ensure that there were no bubbles in the system, three way stop valves were used to aid purging the system.

Two micron diameter carboxylated polystyrene fluorescent microspheres (Invitrogen Corporation) were used as seed particles. The wavelengths of excitation and emission maxima of the seed particles were 535nm and 575nm respectively. The particle solution was carefully prepared by first rinsing the particles in NanoPure water to remove any contaminants. The washed particles were then re-suspended in degassed NanoPure water to prevent the particles from forming clusters. Care was taken to make sure that bubbles were not present in either the tubing or in the reactor itself as they might alter the flow significantly. The particles were illuminated by a 532nm double pulsed Nd:YAG laser (Continuum *minilite*), which passed through a lens system (L1, L2 and D in Fig. 5.2) before entering the optical port in the rear of the inverted microscope (*Nikon Inc.* TE-300). The convex lens L1 and the concave lens L2 in combination produces an expanded collimated beam, which is then passed through a diffuser, resulting in a uniform illumination over the field of view. The laser light is then guided through the objective by means of a dichroic mirror, after passing through a cleanup filter. The ob-

Table 5.1 Summary of Images Captured

Re	No. of Images
200	800
1000	2000
1500	2500

jective of the microscope can be raised or lowered along the z -direction in order to focus the microPIV images at a desired depth in the microreactor. After passing through the objective and a 560nm long pass filter that removes any scattered 532nm light from the illuminating laser, the particle images were recorded by a CCD camera (12 bit Imager Intense, *LaVision Inc*). The synchronization between the laser and the camera is controlled by a Programming Timing Unit (PTU) via *daVis* software (*LaVision Inc*). In the presented experiments, a 4 X 0.2NA objective was used in conjunction with a 0.45x coupler giving an overall magnification of 1.8X. This resulted in a depth of correlation of $93\mu\text{m}$. The microPIV experiments were performed for Reynolds numbers of 200, 1000 and 1500, where, the Reynolds number is based on the hydraulic diameter and mean velocity of the inlet streams. The number of velocity vector field collected at different Reynolds numbers is summarized in Tab. 5.1. The vector fields were calculated by first subtracting the background from every image and then applying a multi pass decreasing window size PIV algorithm. The initial interrogation window size was 32×32 pixels and the final interrogation widow size was 16×16 pixels, with a 50% overlap. This resulted in a velocity vector spacing of $57.5\mu\text{m}$ in the both X and Y directions. Typically, higher resolution can be obtained by increasing the particle concentration. However obtaining a high particle density is extremely challenging in microPIV, and this limits the spatial resolution in microPIV [3]. The particle images for all the Reynolds numbers were collected at the midplane (in the z -direction) of the channel.

Measurement Errors

The experimental error due to the interrogation of the particles images can be estimated to be $\frac{1}{10}$ of the seed particle image diameter, if the particle image covers approximately 3-4

pixels [66]. From the experimental parameters used in the present experiments, the particle image diameter is approximately $10\mu m$, yielding an effective particle diameter of $5.6\mu m$ when projected back to flow coordinates, meaning the measured particle displacements should be accurate to within $0.56\mu m$. In each of the microPIV experiment, the particles travel approximately $35\mu m$, resulting in an measurement uncertainty of 1.6%

Another potential source of error that one encounters in PIV is peak locking [67], where the measured displacements of the particles are biased towards integer pixel values. In order to ensure that the experimental results are free from peak locking, one can calculate the peak locking coefficient [68], which when between the values of 0 and 0.1, suggests negligible peak locking. In the present experiments, at Re 1500, the peak locking coefficient was equal to 0.015, suggesting a negligible degree of peak locking. Similar peak locking coefficients were found at the two lower Reynolds numbers investigated.

5.5 Results and Discussion

5.5.1 Instantaneous and Mean Velocity Fields

Instantaneous velocity fields were collected midway along the depth of the reactor (i.e., the centerplane of the reactor). Examples of instantaneous vector fields for the Reynolds numbers of 200, 1000 and 1500 are shown in Fig. 5.3. The collected instantaneous velocity fields at each Reynolds number can be ensemble averaged, resulting in the mean velocity fields shown in Fig. 5.4.

In the case of Re 200, the flow is not only laminar and steady state in the two inlets, but also in the entire reactor. The two inlet jets meet slightly below the center line of the inlet jets and in the middle of the reactor along the plane of symmetry. Once they impinge, the horizontal momentum of the jets decreases. Some of the jet fluid turns towards the top of the reactor and the rest turns towards the outlet of the reactor. As is evident from Fig. 5.4(a), four recirculation zones are formed, two above the inlet jets and two below the inlet jets. The flow in the inlet channels is fully developed laminar channel flow with a peak velocity of 0.6m/s. Comparing all of the instantaneous velocity field realizations at $Re = 200$, one observes that

there is very little unsteadiness (if any), and the difference between the instantaneous flow field and mean flow field is minimal, confirming that the flowfield is indeed steady at this Reynolds number.

As the Reynolds number increases, the high velocity jets upon impinging inside the reactor form an unstable impingement zone, and the flow becomes unsteady and turbulent, even though the flow in the inlet channel remains laminar. The flow being turbulent at these Reynolds numbers is consistent with the findings from large eddy simulations and microPIV experiments of the flow in an axisymmetric confined impinging jets reactor at Reynolds numbers up to 700 [61],cite[b]. Unlike an axisymmetric reactor, where the diameter of the inlet streams is smaller than the diameter of the reaction chamber, and thus the jets and the impingement zone are free to move in multiple direction, the reactor in the present study is a confined rectangular reactor where the depth of jets is equal to the depth of the reactor, and the flapping of the jets is confined only to the direction transverse to the incoming jets. This flapping is observed at both $Re=1000$ and $Re=1500$. The flapping consists of the impingement zone obliquely rocking about the centerline of the reactor. In addition to this unsteady flapping, evidence of turbulent eddy structures can be observed in the instantaneous velocity fields shown in Figures. 5.3(b) and 5.3(c).

It can also be observed from the mean flow fields Fig. 5.4 that the volume of region trapped above the two impinging inlet jets increases with increasing Reynolds number as the bulk of the fluid turns towards the outlet of the reactor. The velocity of the fluid trapped in the region above the jets is very small compared to that of the velocity of the jets themselves. This makes it very difficult to accurately measure the velocity in this region simultaneously with the velocity in the jets and the impingement zone, because the seed particles are hardly moving at all in this region (recall the measurement error is inversely proportional to the displacement of particles). The flow in the inlets is fully developed at Re 1000 giving rise to a parabolic profile with a peak velocity of $3m/s$; however, the flow is not fully developed laminar flow in the inlets at Re 1500 as the lengths of the inlets are not sufficiently long enough. Hence, the peak velocity measured in the midplane of the inlet was $3.9m/s$, when it would have been

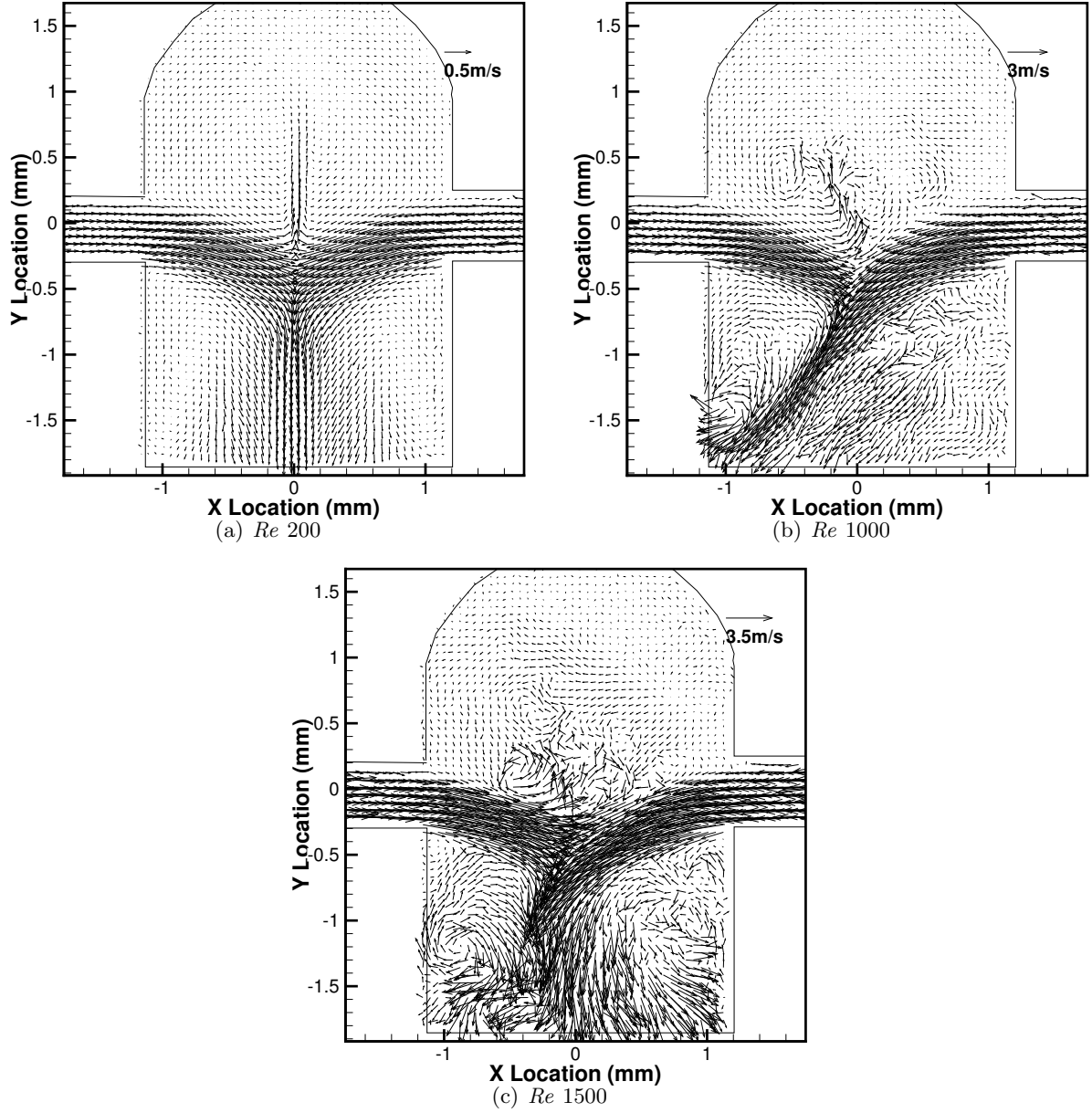


Figure 5.3 Instantaneous Velocity Vector Fields at various Reynolds numbers. In all the figures presented above, every other vector has been deliberately removed for the sake of clarity

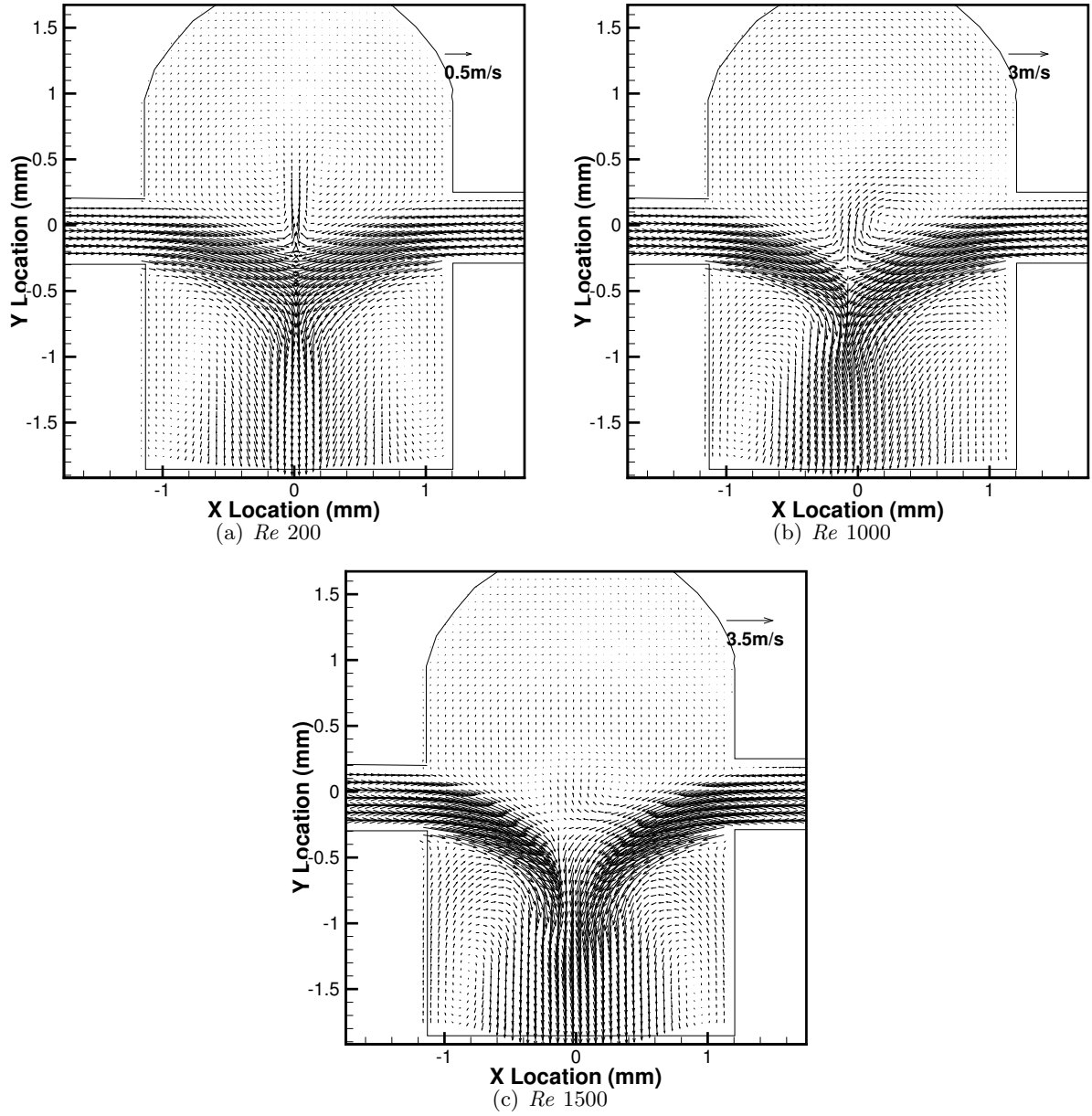


Figure 5.4 Mean Velocity Vector Fields at various Reynolds numbers. In the above figures, every other vector has been removed for the sake of clarity

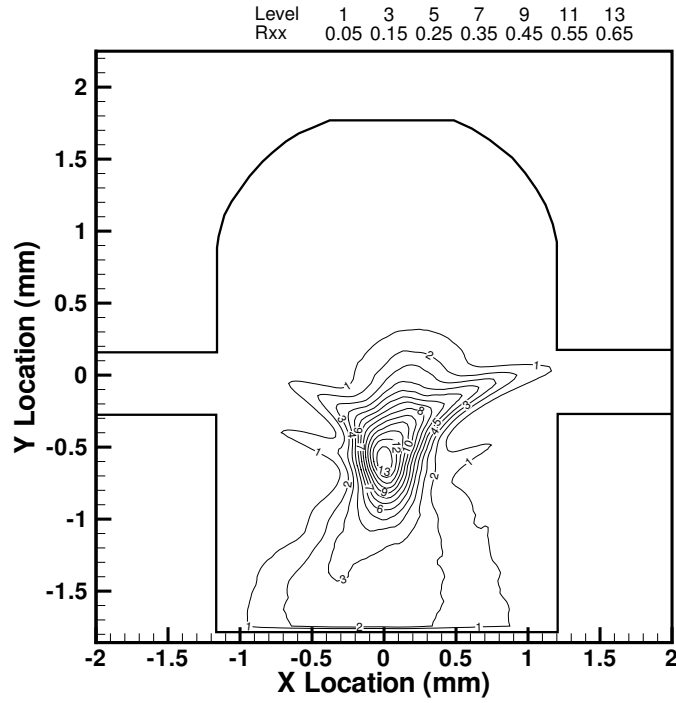


Figure 5.5 Reynolds normal stress $\frac{\langle u'u' \rangle}{U^2}$ at Re 1000

4.5m/s had it been developed fully.

5.5.2 Turbulence Statistics

5.5.2.1 Reynolds Stresses

In order to quantify and characterize the turbulence in the reactor, Reynolds normal and shear stresses for the jets Reynolds numbers of 1000 and 1500 have been calculated and plotted in Figs. 5.5 - 5.10. The Reynolds stresses for the case of Re 200 are not presented as the Reynolds stresses were equal to zero everywhere in the reactor, as expected, since such a low Reynolds number results in laminar flow throughout the reactor. Since the flow into the reactor should ideally be symmetric, one would expect the Reynolds stresses shown in Figs. 5.5 - 5.10 to also be symmetric. However, the Reynolds stresses presented here are not perfectly symmetric due to either slight asymmetries in the velocities of the inlet jets or slight variations in the geometry of the reactor. Figures. 5.5 and 5.6 show the normalized Reynolds normal stresses $\frac{\langle u'u' \rangle}{U^2}$, where U^2 is the mean velocity of the inlet channels. The peak Reynolds normal stress

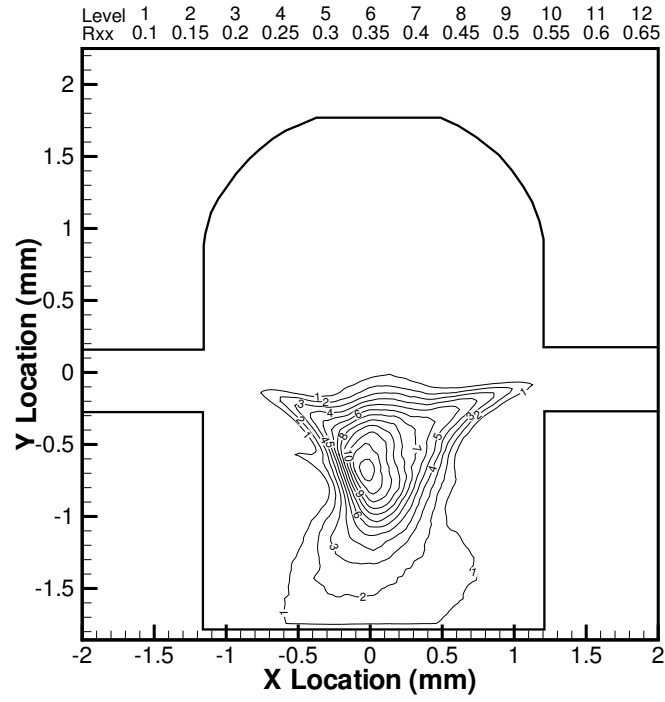


Figure 5.6 Reynolds shear stress $\frac{\langle u'v' \rangle}{U^2}$ at $Re = 1500$

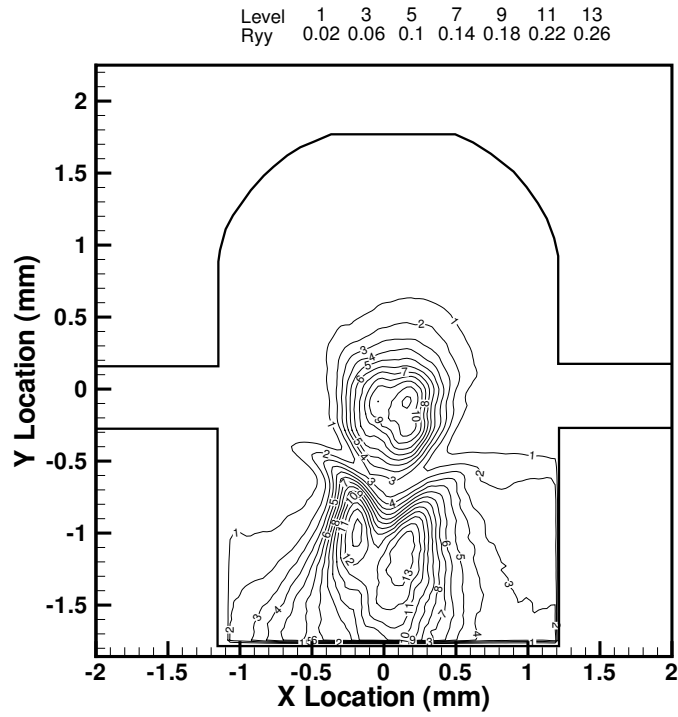


Figure 5.7 Reynolds normal stress $\frac{\langle v'v' \rangle}{U^2}$ at $Re = 1000$

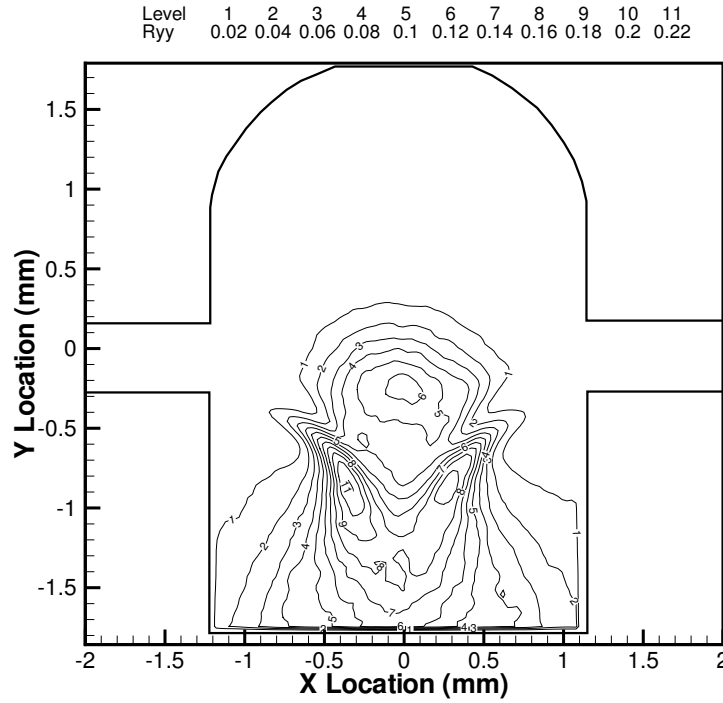


Figure 5.8 Reynolds normal stress $\langle v'v' \rangle$ at $Re = 1500$

occurs where the two jets collide in the impingement zone along the centerline of the reactor. At $Re = 1000$, the peak value of $\frac{\langle u'u' \rangle}{U^2}$ is 0.65, while at $Re = 1500$, the peak value is 0.65 as well. Moreover, at both Reynolds numbers, just below the impingement zone, there is a region where $\frac{\langle u'u' \rangle}{U^2}$ is approximately 15% of the peak value in the impingement region. This region spreads towards the walls of the reactor, which is due to the fact that there is band of high speed fluid which flaps back and forth from one reactor wall to the other at these Reynolds numbers. One can also observe that the area of non-zero Reynolds stress is larger in the case of $Re = 1500$ compared to that of $Re = 1000$ as the turbulent impingement zone moves about more as the Reynolds number increases.

Figures 5.7 and 5.8 show the normalized Reynolds normal stresses $\frac{\langle v'v' \rangle}{U^2}$. Again, one observes the presence of two regions at both Reynolds' numbers. The top smaller region is due to the small band of high speed fluid that flaps back and forth in the impingement region. The peak value of $\frac{\langle v'v' \rangle}{U^2}$ in this region is 0.26 at $Re = 1000$ and 0.22 at $Re = 1500$. Evidence of this flapping was also observed in the instantaneous velocity fields as shown in Fig. 5.3.

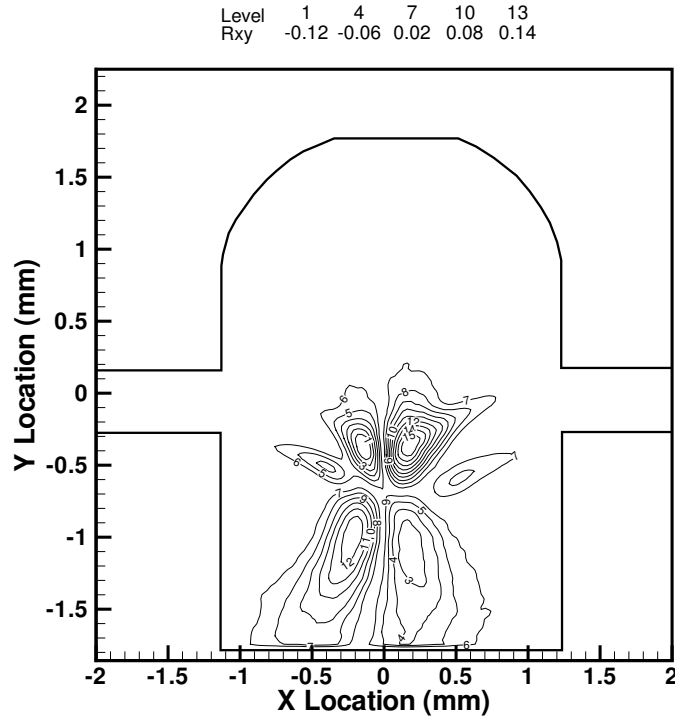


Figure 5.9 Reynolds normal stress $\frac{\langle u'v' \rangle}{U^2}$ at Re 1000

This flapping does not extend well into the trapped region above the impinging jets, and so the Reynolds stress is low in this region. The lower region has a higher value than the value in the impingement region, and is due to the jets turning and combining into a single, higher velocity jet as they move towards the outlet of the reactor. The higher v -velocity and the oblique flapping in this region results in the higher $\frac{\langle v'v' \rangle}{U^2}$ in this region. The far edges of the lower region correspond to the boundaries of the flapping zone generated in the reactor.

Figures 5.9 and 5.10 show the dimensionless Reynolds shear stresses $\frac{\langle u'v' \rangle}{U^2}$ at Re 1000 and Re 1500 respectively. The Reynolds shear stress has a shape of a butterfly with four distinct zones. The area where the four zones intersect is the region of the peak value of $\frac{\langle u'v' \rangle}{U^2}$. The shape gives us an idea as to location of the center of the impingement zone since the center of the impingement zone is a point of symmetry. The shape is also consistent with a Reynolds stress dominated by the oblique flapping of the impingement zone. Imagine the impingement plane is initially oriented vertically as in Fig. 5.3(a). When the plane rocks clockwise, the upper right portion of the plane has a positive u and a positive v velocity, resulting in a positive $u'v'$ event.

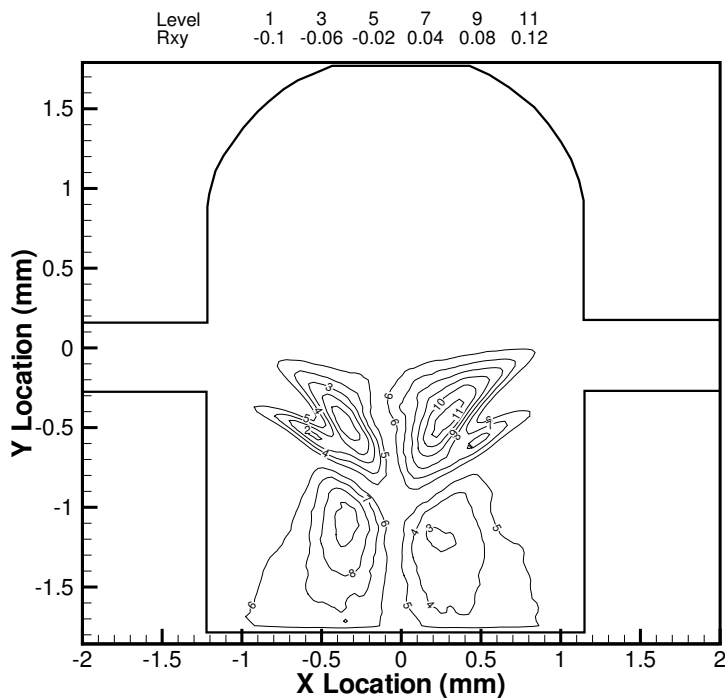


Figure 5.10 Reynolds shear stress $\frac{\langle u'v' \rangle}{U^2}$ at Re 1500

Similarly, the lower left portion of the reactor has a negative u and a negative v velocities, also resulting in a positive $u'v'$ event. However, when the plane rocks counterclockwise, the upper left portion of the reactor has a negative u and a positive v , resulting in a negative $u'v'$ event, while the lower right portion has a positive u and a negative v , also resulting in a negative $u'v'$ event. In all four quadrants, the magnitude of the dimensionless Reynolds shear stress is approximately 0.14 at $Re = 1000$, and 0.12 at $Re = 1500$.

5.5.2.2 Two Point Spatial Correlation

In addition to providing pointwise information of velocities and Reynolds stresses, the microPIV data can also provide statistical data on the large scale coherent structures present in the flow through spatial correlations of the velocity fluctuations. The spatial auto and cross correlations of the u' and v' velocity fluctuations are calculated using velocity fluctuations at two different points in the flow. For example, the spatial correlation $R_{u'_i u'_j}$ can be calculated

using

$$R_{u'_i u'_j} = \frac{\langle u'_i(X, Y) u'_j(x, y) \rangle}{\sqrt{\langle u'^2_i(X, Y) \rangle \langle u'^2_j(x, y) \rangle}} \quad (5.2)$$

where (X, Y) and (x, y) are the coordinates of a basis point (*i.e.*, the point about which the spatial correlation is measured) and a displacement from the basis point respectively. In the present study, the location of the peak $\langle u' u' \rangle$ Reynolds stress was chosen as the basis point as this point represented the core of the impingement region. The area over which the spatial correlation is calculated on a grid corresponding to 40x50 vectors, centered about the basis point.

The autocorrelation and the cross correlation of the velocity fluctuations are shown in Figs. 5.11 and 5.12 for $Re = 1000$ and $Re = 1500$ respectively. The correlations are normalized such that the peak values of the autocorrelations are 1 at the basis point. The $R_{u' u'}$ correlation is shown for $Re = 1000$ in Fig. 5.11(a) and for $Re = 1500$ in Fig. 5.12(a). Both the size and the shape of the correlation vary with Reynolds number. The area of the highly correlated region is smaller at $Re = 1500$ than $Re = 1000$. Moreover, at $Re = 1000$, the highly correlated region is roughly circular in shape, while at $Re = 1500$, the highly correlated region is a vertically oriented ellipse. This central region of both correlations is due to the turbulent structures at the center of the impingement zone, and the decreasing size of this region with increasing Reynolds number is consistent with these turbulent structures becoming smaller with increasing Reynolds number. The smaller valued correlation contours, such as the 0.2 contour, roughly suggest the butterfly shape observed in the $\frac{\langle u' v' \rangle}{U^2}$ Reynolds stress contours. This shape is consistent with the effects of the previously described rocking motion of the impingement plane and the effects this rocking would have on the u' velocity fluctuations.

Figures. 5.11(b) and 5.12(b) show the autocorrelation of v' . It can be seen that the area of the highly correlated region is once again larger at $Re = 1000$ than at $Re = 1500$, consistent with the fact that the size of the structures becomes smaller with higher Reynolds number. The autocorrelations are elliptical in shape, with the major axis aligned along the outlet of the CIJR. It can also be seen that there is a negative correlation on either side of the basis point. This suggests that the oblique flapping of the impingement zone also induces a slight

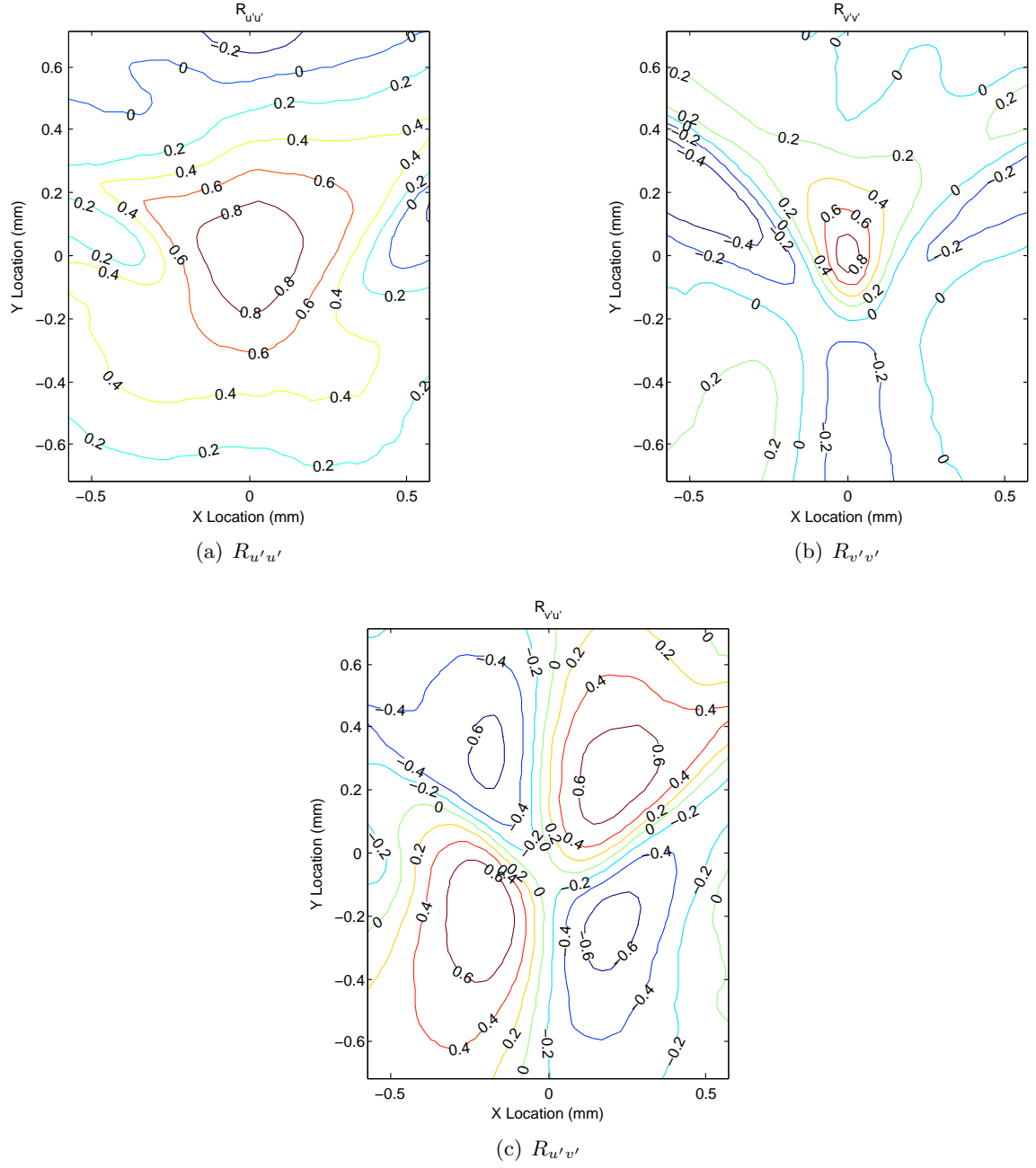


Figure 5.11 Two Point Spatial Correlation at $Re = 1000$

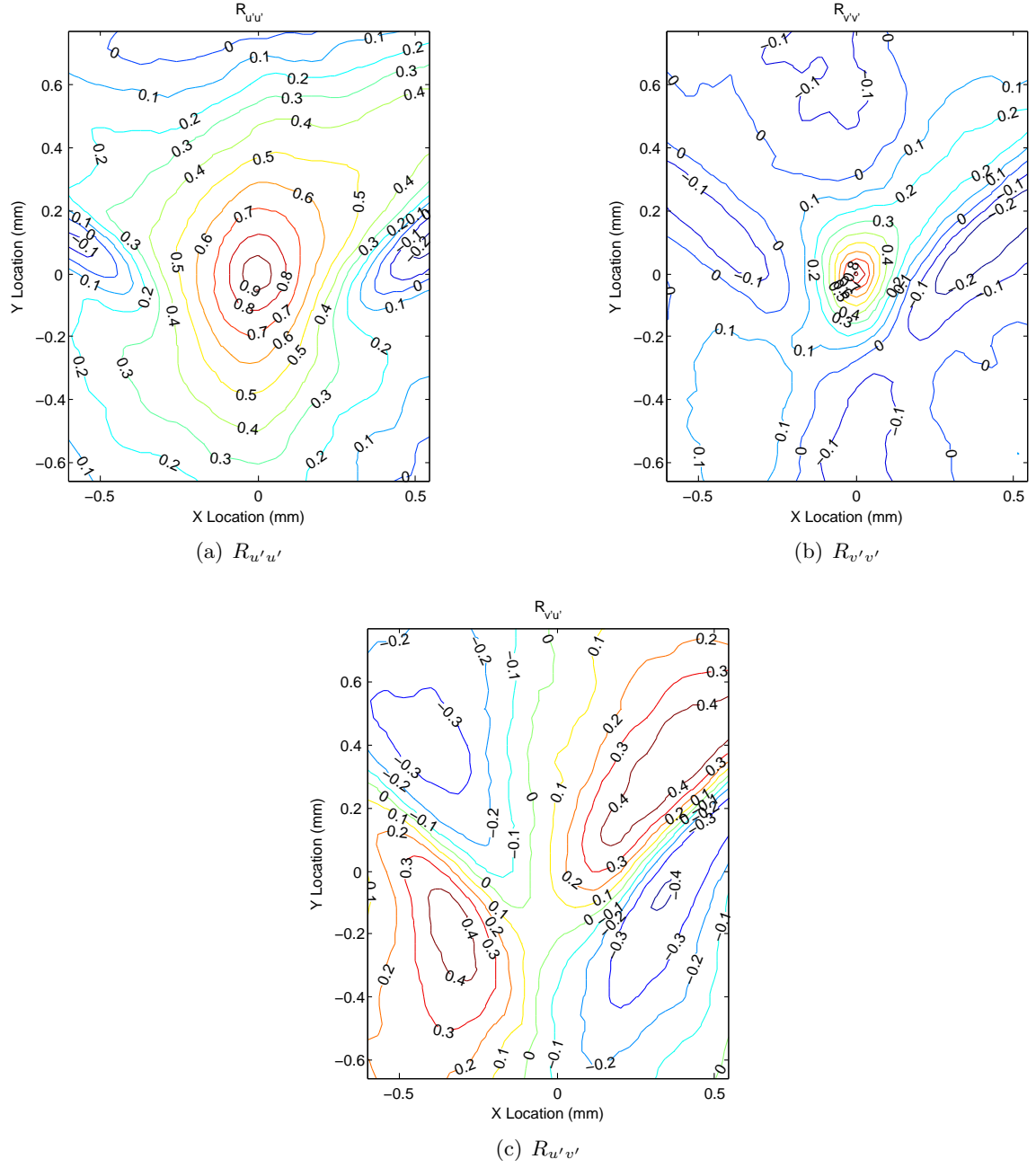


Figure 5.12 Two Point Spatial Correlation at $Re = 1500$

vertical flapping of the two impinging jets, and the interplay between these motions results in the features observed in the autocorrelation field. Towards the bottom of the reactor, one also observes an elongated elliptical negatively correlated region, which is a consequence of the flapping of the impingement zone and its effects on the flow near the outlet.

Figures. 5.11(c) and 5.12(c) show the crosscorrelation of u' at the basis point with v' for various points in the flow field. For both $Re = 1000$ and $Re = 1500$, the cross correlation is in the shape of butterfly wings just as seen in the Reynolds shear stress plots shown in Figs. 5.9 and 5.10. Also, just as for the Reynolds shear stress, this shape is a direct consequence of the oblique flapping of the impingement zone about the center of the reactor. The peak correlation values are higher for $Re = 1000$ than for $Re = 1500$ (just as the normalized Reynolds shear stresses were higher for $Re = 1000$ than for $Re = 1500$) due to the oblique flapping motion being more coherent at $Re = 1000$ than at $Re = 1500$.

5.6 Conclusions

MicroPIV experiments were performed on a rectangular CIJR for inlet stream Reynolds numbers of 200, 1000 and 1500. The flow is laminar and virtually steady state through the reactor for the case of Re 200. Although, the flow in the inlet regions is laminar for the cases of Re 1000 and Re 1500, instabilities as a result of high velocity jets impinging in the middle of the reactor lead to a highly turbulent and unsteady impingement region. An oblique flapping of the impingement zone is observed at both these Reynolds numbers. The center of the impingingemet zone for these cases was slightly below the centerline of the inlets, with the impingement point moving further towards the reactor outlet for the case of Re 1500. Reynolds normal and shear stresses were computed and analyzed. We observed that the peak magnitude of the normalized Reynolds normal and shear stresses were approximately the same for the Reynolds numbers of 1000 and 1500. At these Reynolds numbers, from Figs 5.5, 5.6, we noticed that there is a region below the location of the peak value of $\frac{\langle u'u' \rangle}{U^2}$, which extends from wall to wall which is as a result of the jets moving back and forth after impinging roughly in the center of the reactor. From the normalize Reynolds stresses $\frac{\langle v'v' \rangle}{U^2}$, we observed that

the stresses are split into two regions, above and below the point of peak $\frac{\langle u'u' \rangle}{U^2}$. These were formed as a result of part of the impinging jets turning towards the top wall of the reactor and the rest turning towards the outlet of the reactor. It was further noted that this top region is smaller due the fact that the part of the impinging jets, after turning upwards slow down in the trapped volume of fluid. The shape of normalized Reynolds shear stress $\frac{\langle u'v' \rangle}{U^2}$ was found to be like that of butterfly wings. The values of the stresses are negative along the diagonal from top left to bottom right (u and v components are of opposite signs), and are positive along the diagonal going from top right to bottom left (both u and v are of the same sign). The spatial auto and cross correlations were calculated and analysed to get an understanding of size of the coherent structures. The location of the peak $\frac{\langle u'u' \rangle}{U^2}$ was chosen as the basis point, as this represented the center of the impingement zone. It was observed that the shape of the highly correlated regions for $R_{u'u'}$ was circular in shape at Re 1000, and was elliptical in shape for Re 1500. It was also noticed that the area of higher correlation was large at Re 1000, suggesting as expected, the turbulent structures becoming smaller with increasing Reynolds number. The shape of the cross correlation was that of butterfly wings consistent with the observations from the normalized Reynolds shear stresses.

CHAPTER 6. Large Eddy Simulation of CIJR

In this chapter, a very brief introduction to the method of Large Eddy simulation is given. It is specifically geared towards incompressible flows. We then present the finite volume method of solving the incompressible Navier-Stokes equations. The results of the LES applied to the confined impinging jets is presented and compared to the experimental results from the previous chapter.

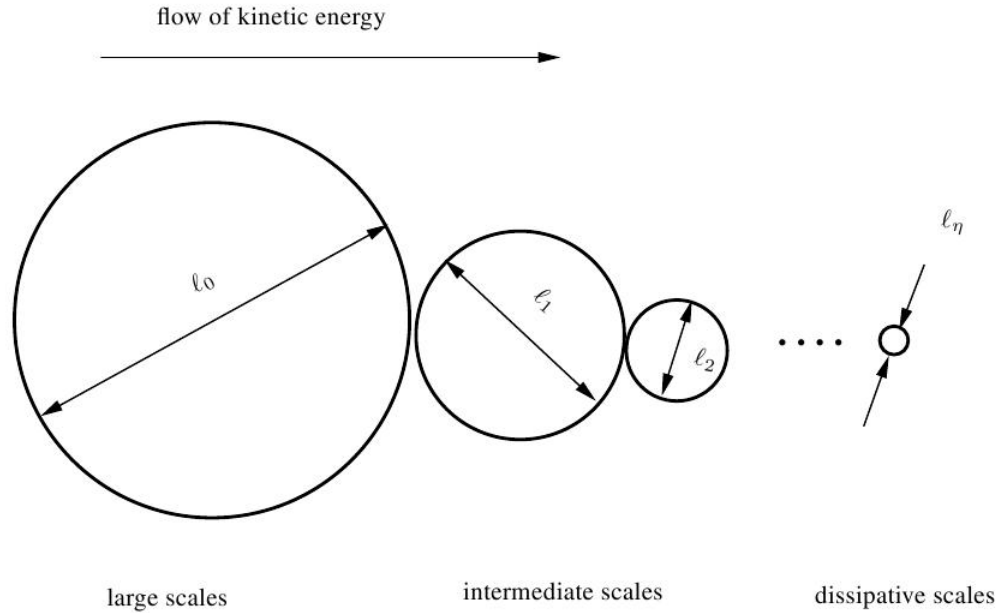
Turbulence is everywhere in nature and we only have to look to find one. Some of the examples that one could easily relate to are flow around cars, trucks, aircrafts, plume from smoke stack etc. There isn't a formal definition of a turbulent flow, however, it is described based on the following characteristics (see Pope [69] and Tennekkes & Lumley [70])

1. Irregularity
2. Diffusivity
3. Large Reynolds number
4. Three dimensional
5. Dissipation
6. Continuum

Turbulent flows, like all other fluids flows are governed by the Navier-Stokes equations. The continuity and the momentum equations for the incompressible flows are given below.

$$\frac{\partial u_i}{\partial x_i} = 0 \quad (6.1)$$

$$\frac{\partial u_i}{\partial t} + \frac{\partial u_i u_j}{\partial x_j} = -\frac{1}{\rho} \frac{\partial p}{\partial x_i} + \nu \frac{\partial^2 u_i}{\partial x_j \partial x_j} \quad (6.2)$$



isucaptionTurbulent Scales (Source: Lecture Notes on Turbulence by Lars Davidson)

Turbulent flows have a wide range of length scales as shown in the Fig. 6. The large eddies are of the size comparable to that of the flow geometry. They extract energy from the mean flow. They interact with the smaller eddies transferring the energy. These smaller eddies interact with even smaller eddies, again transferring the energy. This continues as a energy cascade until they reach the smallest scales (Kolmogorov scales), where the energy is dissipated as heat (viscous dissipation).

6.1 Direct Numerical Simulation, RANS and LES

There are only a handful of analytical solutions available in the literature for very simple flows, let alone turbulent flows. Hence, one tries to solve the Navier-Stokes equations numerically. The straight forward and intuitively very simple way of solving these equations is called Direct Numerical Simulation (DNS), where all we do is discretize the continuity and the momentum equations and solve for the flow quantities, without using any models for turbulence. The only requirement being that the equations are solved on a grid, which is fine enough to resolve even the smallest of scales. This requirement makes it almost impossible to perform DNS on any practical industrial problems, and is instead restricted to simple cases. The cost

of DNS goes approximately as Re^3 .

The second method of solving is called the Reynolds Average Navier-Stokes (RANS), where the flow variable is decomposed into a mean and a fluctuating component. We then solve for the mean quantities, and the effect of the turbulence is input exclusively through models. The problem here is that there is no one model that works well for all flows, and has to be tweaked for different flows encountered on a case by case basis, since the large eddies that contribute to energy transfer are dependant on the flow geometry and boundary conditions.

Large Eddy Simulation (LES) is a path in between the DNS and RANS. The foundations of LES were laid by Smagorinsky [71] in 1960's. In LES, the large eddies which are dependent of the flow geometry and the boundary conditions are computed explicitly, and the small scales are represented by a model. By doing so, LES addresses the drawbacks of both DNS and RANS. The idea that the small scales can be represented by a model is based on the theory of Kolmogorov [72], that the small scales are some what universal in nature and drain the energy received from the large scale via the cascade process. Therefore, the computational effort required by a LES is far less compared to DNS. However, it should be noted that the computational effort required is also a lot more compared to that of a RANS simulation. One more advantage that LES has over RANS is that we can solve complex three-dimensional unsteady problems instead of just solving for mean quantities.

In LES, the variables that we are interested in is decomposed into a filtered part and a residual part. The idea is to solve for the filtered part by accounting the effect of the residual part via modeling. This is accomplished by using a low pass filter, which will essentially remove all the small scale motions. The filtering is performed by convolving a chosen filter kernel G with the variable, say $f(\vec{x}, t)$, to obtain the filtered quantity $\tilde{f}(\vec{x}, t)$

$$\tilde{f}(\vec{x}, t) = \int_{-\infty}^{\infty} f(\vec{x} - \vec{\zeta}, t) G(\vec{\zeta}) d\vec{\zeta} \quad (6.3)$$

The filter kernel G is associated with the cut-off scale Δ (filter width). They conform to certain properties which are listed below:

Table 6.1 Common LES filters

Box	$G(x) = \begin{cases} \frac{1}{\Delta} & \text{if } x \leq \frac{\Delta}{2} \\ 0 & \text{otherwise} \end{cases}$
Gaussian	$\sqrt{\frac{6}{\pi\Delta^2}} \exp\left(\frac{-6x^2}{\Delta^2}\right)$
Sharp spectral filter	$G(k) = \begin{cases} 1 & k \leq \Delta \\ 0 & \text{otherwise} \end{cases}$

- Filter applied to a constant quantity is a constant

$$\int_{-\infty}^{\infty} G(\vec{x}d\vec{x}) = 1$$

- Linearity:

$$\widetilde{f + v} = \widetilde{f} + \widetilde{v}$$

- Commutate with differentiation

$$\begin{aligned} \frac{\partial \widetilde{f}}{\partial \vec{x}} &= \frac{\partial \widetilde{f}}{\partial \vec{x}} \\ \frac{\partial \widetilde{u}_i}{\partial t} + \frac{\partial \widetilde{u}_i \widetilde{u}_j}{\partial x_j} &= -\frac{1}{\rho} \frac{\partial \widetilde{p}}{\partial x_i} + \nu \frac{\partial^2 \widetilde{u}_i}{\partial x_j^2} - \frac{\partial \tau_{ij}}{\partial x_j} \end{aligned} \quad (6.4)$$

6.2 LES filters

The filters can be applied either in the spatial domain or in the frequency domain. The most common filters used are listed in Tab. 6.1. The shape of these filters in the spatial and the frequency domains are shown in Fig. 6.1.

When the filter operation is performed on the Navier-Stokes equations, we get what are called filtered Navier-Stokes equations as below

$$\frac{\partial \bar{u}_i}{\partial x_i} = 0 \quad (6.5)$$

$$\frac{\partial \bar{u}_i}{\partial t} + \frac{\partial \bar{u}_i \bar{u}_j}{\partial x_j} = -\frac{1}{\rho} \frac{\partial \bar{p}}{\partial x_i} - \frac{\partial \tau_{ij}}{\partial x_j} + \nu \frac{\partial^2 \bar{u}_i}{\partial x_j \partial x_j} \quad (6.6)$$

The above set of equations looks very much like the N-S equations written in terms of filtered quantities, with an addition of the subgrid-scale (SGS) stress term, also known as residual

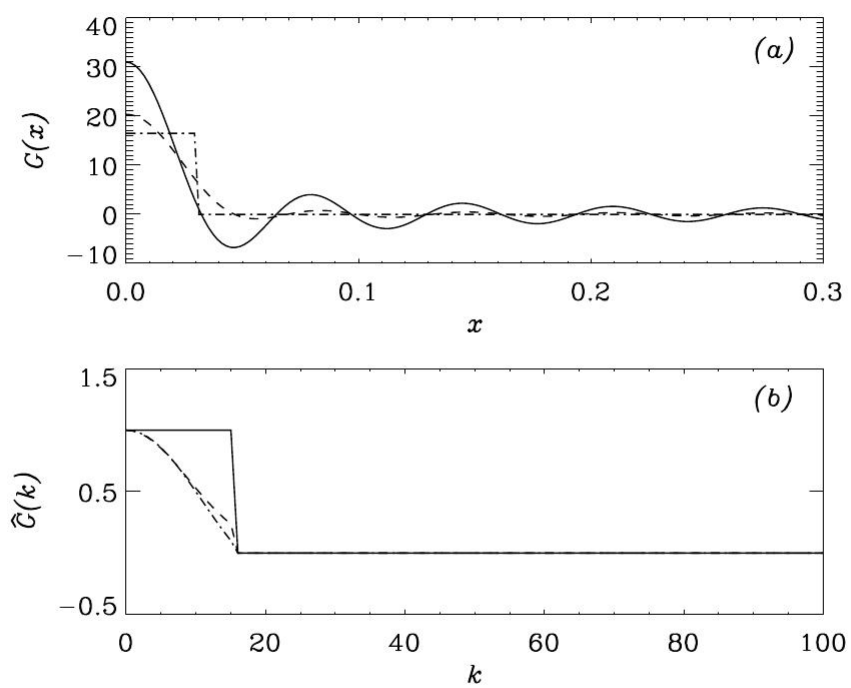


Figure 6.1 Shape of filters in Spacial and Frequency domain

stress term given by

$$\tau_{ij} = \overline{u_i u_j} - \bar{u}_i \bar{u}_j \quad (6.7)$$

The SGS term has to be modeled in order to achieve closure.

6.3 Subgrid scale models

6.3.1 Smagorinsky model

In turbulent flows the energy from the mean flow (large scale) cascades to the smallest scales, where the energy drains in the form of viscous dissipation. Since, in LES we explicitly resolve the large scale features, the primary purpose of the SGS model is to drain the energy the small scale structures receive from the large scale structure via cascade. Smagorinsky model [71], is like most SGS models, is eddy viscosity based model. Here, the traceless part of the SGS stress term is related to the strain rate \bar{S}_{ij} of the resolved velocity field.

$$\tau_{ij}^r = \tau_{ij} - \frac{1}{3} \delta_{ij} \tau_{kk} = -2\nu_t \bar{S}_{ij}, \quad \text{where} \quad (6.8)$$

ν_t is called turbulent viscosity, is calculated based on the analogy to the mixing-length hypothesis as

$$\nu_t = l^2 |\bar{S}|$$

In Smagorinsky model, the SGS turbulent length scale l corresponds to $C_s \Delta$, where C_s is the Smagorinsky constant, and $\Delta = (\Delta x \Delta y \Delta z)^{1/3}$, is the filter width. Lilly [73] used a sharp spectral filter to obtain the value of $C_s = 0.17$.

6.3.2 Dynamic subgrid scale model

The main drawback in using the Smagorinsky model is that the Smagorinsky constant C_s has to be specified. Germano et al. [74] developed a procedure to calculate the model coefficients during the simulation, thus eliminating the need to specify it manually. From Eqn. 6.4, recall that the subgrid scale tensor is given by

$$\tau_{ij} = \widetilde{u_i u_j} - \tilde{u}_i \tilde{u}_j \quad (6.9)$$

This was obtained by applying a filter, of size Δ (in the equations this is denoted by $-$). The dynamic procedure calls for applying another test filter of width $\bar{\Delta}$ larger (typically twice as big as Δ) to the filtered Navier-Stokes equation (eqn. 6.4).

$$\frac{\partial \tilde{u}_i}{\partial t} + \frac{\partial \tilde{u}_i \tilde{u}_j}{\partial x_j} = -\frac{1}{\rho} \frac{\partial \tilde{p}}{\partial x_i} + \nu \frac{\partial^2 \tilde{u}_i}{\partial x_j^2} - \frac{\partial \tau_{ij}}{\partial x_j} \quad (6.10)$$

Let us consider the second term, which can be written as

$$\frac{\partial \tilde{u}_i \tilde{u}_j}{\partial x_j} = \frac{\partial}{\partial x_j} (\tilde{u}_i \tilde{u}_j - \tilde{u}_i \tilde{u}_j + \tilde{u}_i \tilde{u}_j) \quad (6.11)$$

Now consider the last term on the RHS of eqn. 6.10, which can be simplified as

$$\frac{\partial \tau_{ij}}{\partial x_j} = \overline{\tilde{u}_i \tilde{u}_j} - \tilde{u}_i \tilde{u}_j \quad (6.12)$$

Combining Eqn 6.11 and Eqn 6.12, we get the SGS stress at the test filter level as shown below

$$T_{ij} = \overline{\tilde{u}_i \tilde{u}_j} - \tilde{u}_i \tilde{u}_j \quad (6.13)$$

The Leonard stress term L_{ij} is given by

$$L_{ij} = \tilde{u}_i \tilde{u}_j - \tilde{u}_i \tilde{u}_j \quad (6.14)$$

combining Eqns. 6.9, 6.12, and 6.14, we get the Germano identity

$$L_{ij} = T_{ij} - \tau_{ij} \quad (6.15)$$

To obtain the dynamic Smagorinsky model, we apply Smagorinsky model at both $\bar{\Delta}$ and Δ filter levels. It is assumed at the same model can be applied for stress at both levels. This will lead to

$$L_{ij} = -2 (C_s \bar{\Delta})^2 |\bar{S}| \bar{S}_{ij} + 2 (C_s \Delta)^2 |\bar{S}| \bar{S}_{ij} \quad (6.16)$$

The error associated in using the Smagorinsky model in the above equation can be found by calculating

$$e_{ij} = L_{ij} - C_s^2 M_{ij}, \text{ where} \quad (6.17)$$

$$M_{ij} = 2 \left[\overline{(\Delta)^2 |\bar{S}| \bar{S}_{ij}} - (\bar{\Delta})^2 |\bar{S}| \bar{S}_{ij} \right] \quad (6.18)$$

The problem with above equation is that we have 9 equations and one unknown. Lilly [75] proposed that the error e_{ij} be minimized in a least square sense. This would require that

$$\frac{\partial e_{ij}^2}{\partial C_s^2} = 0 \quad (6.19)$$

This results in

$$-2L_{ij}M_{ij} + 2C_s^2M_{ij}M_{ij} = 0 \quad (6.20)$$

Rearranging the above equation, we get the equation to for C_s^2 as

$$C_s^2 = \frac{L_{ij}M_{ij}}{M_{ij}M_{ij}} \quad (6.21)$$

The equation thus derived for dynamic Smagorinsky coefficient is numerically unstable. This is overcome by enforcing the Germano identity in an average sense to obtain

$$C_s^2 = \frac{\langle L_{ij}M_{ij} \rangle}{\langle M_{ij}M_{ij} \rangle} \quad (6.22)$$

6.4 Numerical methods

The unsteady convection-diffusion equation of a scalar ϕ in a continuous domain is given by

$$\underbrace{\frac{\partial \rho \phi}{\partial t}}_{\text{Temporal derivative}} + \underbrace{\nabla \cdot (\rho U \phi)}_{\text{Convective term}} = \underbrace{\nabla \cdot (\Gamma \nabla \phi)}_{\text{Diffusive term}} + \underbrace{S_\phi(\phi)}_{\text{Source term}} \quad (6.23)$$

In Eqn. 6.23, ρ is the density, U is the velocity, ϕ is the scalar being transported, Γ_ϕ is the diffusion coefficient and S_ϕ is the source term. It should be noted that both Γ_ϕ and S_ϕ can be a function of ϕ . The above equation is a second order partial differential equation due the presence of $\nabla \cdot \nabla \phi$ term. Therefore, any discretization that is used must be of at least second order, both in time and in space, to maintain the accuracy.

An arbitrary set of control volumes are shown in Fig. 6.2, where two control volumes $CV1$ and $CV2$ share a common *face*. \mathbf{P} is the centroid of the control volume $CV1$ and \mathbf{N} is the centroid of the neighboring control volume $CV2$. \mathbf{A}_{face} is the area normal vector of the face shared between the two control volumes. To obtain second order discretization, one can expand

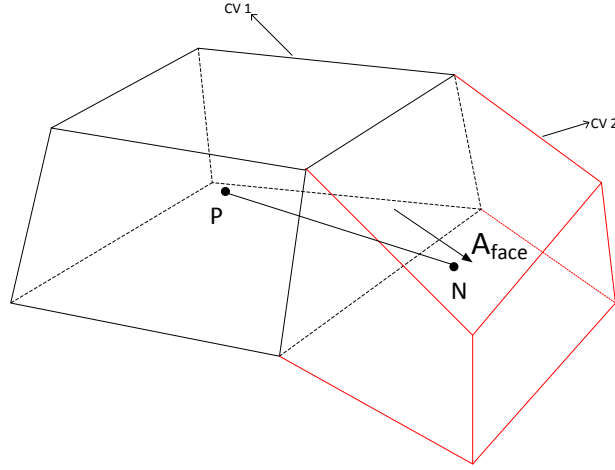


Figure 6.2 Arbitrary Control Volume

$\phi(\mathbf{x})$ as

$$\phi(\mathbf{x}) = \phi_P + (\mathbf{x} - \mathbf{x}_P)(\nabla\phi)_P \quad (6.24)$$

$$\phi(t + \Delta t) = \phi_t + (\Delta t) \left(\frac{\partial\phi}{\partial t} \right)^t \quad (6.25)$$

In this study, we use the finite volume approach, in which we integrate the governing equations over a control volume to obtain the discretized equations. There are other approaches like the finite difference methods and finite elements method to name a few. We chose the finite volume method as the integral formulation results in satisfying the conservation laws exactly. The integral form of Eqn. 6.23 can be written as

$$\int_t^{t+\Delta t} \left[\int_V \frac{\partial \rho \phi}{\partial t} dV + \int_V \nabla \cdot (\rho U \phi) dV \right] dt = \int_t^{t+\Delta t} \left[\int_V \nabla \cdot (\Gamma \nabla \phi) dV + \int_V S_\phi(\phi) dV \right] dt \quad (6.26)$$

The discretization of Eqn. 6.43 has two parts namely *spatial discretization* and *temporal discretization*. We begin the discussion by addressing the spatial terms first. In doing so, we will use Gauss theorem in order to convert a volume integral into an area integral. Gauss theorem states that

$$\int_{V_P} \nabla \cdot \phi dV = \int_A (\phi \cdot \mathbf{n}) dA \quad (6.27)$$

where, \mathbf{n} is the unit normal vector, \mathbf{A} is the surface bounding the control volume V_P . Equation. 6.27 can be further simplified into a discrete form as shown below.

$$\int_A (\phi \cdot n) dA = \int_A \phi \cdot d\mathbf{A} = \sum_f \phi_f \cdot \mathbf{A} \quad (6.28)$$

where, f represents the face of a control volume and \mathbf{A} is the outward area normal vector. In the above equation ϕ_f represents the face centered value of the scalar. Since we solve for the value of ϕ only in the cell centers, we have to find a way to interpolate its value on the face. It is further assumed that the value of scalar ϕ is constant in a control volume. This can be used to evaluate another volume integral as shown below.

$$\int_{V_P} \phi(\mathbf{x}) dV = \phi_P V_P, \text{ where} \quad (6.29)$$

ϕ_P is the cell centered value of the scalar, and V_P is the cell volume.

6.4.1 Convective term

From Eqn. 6.23, the convective term (the scalar ϕ convected by the velocity U) can be recognized as

$$\int_{V_P} \nabla \cdot (\rho U \phi) dV \quad (6.30)$$

Applying the divergence theorem (also referred to as Gauss theorem) Eqn. 6.28, one gets

$$\int_{V_P} \nabla \cdot (\rho U \phi) dV = \sum_f \phi_f \rho U_f \cdot \mathbf{A} \quad (6.31)$$

In Eqn. 6.31, $\rho U_f \cdot \mathbf{A} = F$, the mass flux through the face f . Therefore,

$$\sum_f \phi_f \rho U_f \cdot \mathbf{A} = \sum_f \phi_f F \quad (6.32)$$

At this point, it should be noted that the term F contains velocity U_f evaluated on the face, which again needs to be calculated as we will calculate ϕ_f on the control volume faces. However, care must be taken to ensure that the continuity equation is still satisfied after calculating F on all the faces as shown below

$$\sum_f F = 0 \quad (6.33)$$

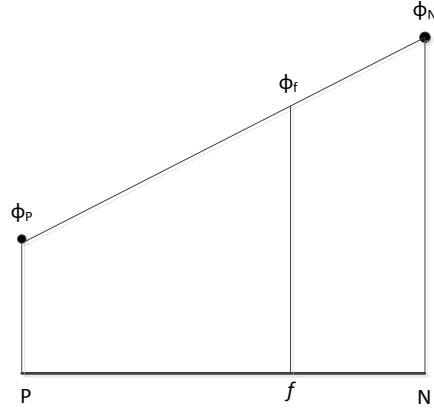


Figure 6.3 Variation of ϕ across two control volumes

For the sake of simplicity, ϕ is assumed to vary linearly as shown in the Fig. 6.3. The value of ϕ_f is calculated using the relation

$$\phi_f = f_R \phi_P + (1 - f_R) \phi_N \quad (6.34)$$

where, the ratio $f_R = \frac{fN}{PN}$. It can be easily verified that in the event of the face being exactly midway between P and N, then, ϕ_f is just the arithmetic average of ϕ_P and ϕ_N . This way of obtaining the value of ϕ on the face is also known as *Central Differencing*. It can be shown that the above mentioned scheme is second order accurate by simply expanding ϕ_P and ϕ_N about f and rearranging the resulting equations. The central differencing scheme is also found to be of second order on unstructured meshes [76]. However, the scheme also has the problem of producing unphysical oscillations when the convection term dominates the system. This phenomenon becomes a problem in a coupled set of equations like that of Navier-Stokes equations. This causes the variable to become unbounded as the value of the variable being solved for at a point is not bounded by the values of the neighboring cell influencing the cell under consideration. This can be overcome by adding a fourth order diffusion term [77], however, it can be very cumbersome to implement this on a unstructured mesh.

Other way of overcoming this issue is by using an upwind scheme that improves the stability and the solution remains bounded. In the upwind scheme, the value of ϕ on the face is

calculated by

$$\phi_f = \phi_P \text{ if } F \geq 0 \quad (6.35)$$

$$\phi_f = \phi_N \text{ if } F < 0 \quad (6.36)$$

This method tends to introduce numerical diffusion, which unfortunately becomes an issue for LES, since the contribution of the modeled diffusivity is overshadowed by the numerical diffusion. The cure to this problem is to use central differencing with mesh refinement in the region where the accuracy of the flow field is very critical. In the non-critical region some sort of upwinding may be used to damp the oscillations.

6.4.2 Diffusive term

By applying Green's theorem (Eqn. 6.28) to the diffusion term in eqn. 6.23, we get

$$\int_{V_P} \nabla \cdot (\Gamma_\phi \nabla \phi) dV = \sum_f (\Gamma_\phi)_f (\nabla \phi)_f \cdot \mathbf{A} \quad (6.37)$$

The diffusion coefficient Γ_ϕ on the face can be found using an equation similar to Eqn. 6.34. Special attention must be paid to the face gradient term $(\nabla \phi)_f$. If the mesh is orthogonal (meaning the vectors A_{face} and \mathbf{d} , the distance vector between \mathbf{P} and \mathbf{N} are parallel), then the gradient of the scalar on the face can be calculated as

$$\mathbf{A} \cdot (\nabla \phi)_f = |A| \frac{(\phi_N - \phi_P)}{|d|} \quad (6.38)$$

Another way of calculating is to use an equation like that of Eqn. 6.34, which results in

$$(\nabla \phi)_f = f_R (\nabla \phi)_P + (1 - f_R) (\nabla \phi)_N \quad (6.39)$$

Using the above equation requires a bigger computational molecule in order to calculate $(\nabla \phi)_{P,N}$. Also, the truncation error associated with this is larger than the method described in Eqn 6.38 as shown by Jasak [78]. If the mesh is non-orthogonal, then the area vector \mathbf{A} is split into orthogonal part and non-orthogonal part as shown in Fig. 6.4. The gradient is then calculated using the relation

$$A \cdot (\nabla \phi)_f = |A_{ortho}| \frac{(\phi_N - \phi_P)}{|d|} + A_{Non-ortho} \cdot (\widetilde{\nabla \phi})_f \quad (6.40)$$

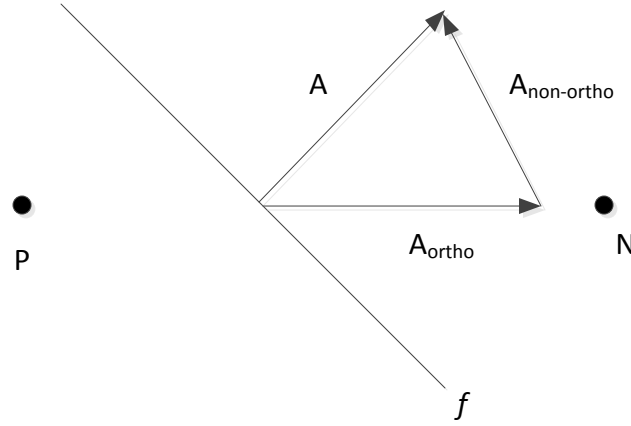


Figure 6.4 Splitting of Area normal vector into orthogonal and non-orthogonal parts

Since calculation of $(\widetilde{\nabla\phi})_f$ requires a larger molecule, it is calculated explicitly by using the values from the previous time-step/iteration.

6.4.3 Source terms

Upon discretization, all the terms that cannot be put into the convective, diffusive or the temporal terms, are collectively clubbed together as source terms. The source terms in general is a function of ϕ , and needs to be linearized. The simplest way is as shown below

$$S_\phi(\phi) = S_c + S_P\phi \quad (6.41)$$

$$\int_{V_P} S_\phi\phi dV = S_c V_P + S_P V_P \phi_P \quad (6.42)$$

In the above equations, V_P is the cell volume and $S_P \leq 0$ as this would increase the diagonal dominance when solving for ϕ later.

6.4.4 Temporal discretization

So far we have dealt with only the spatial discretization, which basically involved converting the volume integrals into area integrals using Green's theorem and the finding the face

centered values of the scalar ϕ , gradient of the scalar ($\nabla\phi$) and the velocity \mathbf{U} . Now, we pay our attention to the temporal discretization by reconsidering the integral form of the scalar transport equation

$$\int_t^{t+\Delta t} \left[\frac{\partial}{\partial t} \int_V \rho \phi dV + \int_V \nabla \cdot (\rho \mathbf{U} \phi) dV - \int_V \nabla \cdot (\Gamma \nabla \phi) dV \right] dt = \int_t^{t+\Delta t} \left[\int_V S_\phi(\phi) dV \right] dt \quad (6.43)$$

Assuming that ϕ is constant in a given control volume, and using Eqns. 6.32, 6.37, 6.42 in the above equation will yield

$$\int_t^{t+\Delta t} \left[\left(\frac{\partial \rho \phi}{\partial t} \right)_P V_P + \sum_f F \phi_f - \sum_f (\rho \Gamma_\phi)_f (\nabla \phi)_f \cdot \mathbf{A} \right] dt = \int_t^{t+\Delta t} (S_c V_P + S_P V_P \phi_P) dt \quad (6.44)$$

Knowing the variation of ϕ from Eqn. 6.25, the time derivative can be calculated using

$$\left(\frac{\partial \rho \phi}{\partial t} \right)_P = \frac{\rho^{n+1} \phi^{n+1} - \rho^n \phi^n}{\Delta t} \quad (6.45)$$

where, $n + 1$ denotes the new time step, and n denotes the current time step. It is worth mentioning here that the discretization of ϕ with respect to time can be completely different from how the convective, diffusive and the source terms are discretized. The only caveat being that all of the discretization schemes should be of at least second order, to ensure second order accuracy overall. At this point we will have to decide as to how the other terms which are evaluated on the face vary with time. If we evaluate ϕ_f as

$$\int_t^{t+\Delta t} \phi_f dt = \frac{1}{2} (\phi^{n+1} + \phi^n) \Delta t \quad (6.46)$$

Then, we can simplify Eqn.6.44 as

$$\begin{aligned} & \frac{(\rho_P \phi^{n+1} - \rho_P \phi^n)}{\Delta t} V_P + \frac{1}{2} \left(\sum_f F \phi_f^{n+1} - \sum_f (\rho \Gamma_\phi)_f (\nabla \phi)_f^{n+1} \cdot \mathbf{A} \right) \\ & + \frac{1}{2} \left(\sum_f F \phi_f^n - \sum_f (\rho \Gamma_\phi)_f (\nabla \phi)_f^n \cdot \mathbf{A} \right) \\ & = S_c V_P + \frac{1}{2} S_P V_P \phi_P^{n+1} + \frac{1}{2} S_P V_P \phi_P^n \end{aligned}$$

The above discretization is known as Crank-Nicholson method. It is second order accurate in time and is unconditionally stable (see Hirsch [79]). It does require calculation of ϕ , $\nabla\phi$ on

the faces at both the current and the new time step. The face values are calculated using any of the appropriate schemes discussed earlier. This means that Crank-Nicholson method does require a lot of memory as it has to store a number of variables, which in turn also makes the procedure computationally expensive.

Even though, the variation of ϕ in time is linear, the derivative is second order accurate at time $t + \Delta t/2$. Therefore, assuming the same value of the temporal derivative at $t + \Delta t$, would make it first order. It is customary to ignore the variation of face values of both ϕ and $\nabla\phi$ in time (see Patankar [80]). Therefore, one can construct a second order accurate scheme by using three time levels ($n+1$, n , and $n-1$) as shown below, by expanding ϕ^n and ϕ^{n-1} in terms of ϕ^{n+1} , and then rearranging.

$$\phi^n = \phi^{n+1} - \frac{\partial\phi}{\partial t}\Delta t + \frac{1}{2}\frac{\partial^2\phi}{\partial t^2}(\Delta t^2) + O(\Delta t^3) \quad (6.47)$$

$$\phi^{n-1} = \phi^{n+1} - 2\frac{\partial\phi}{\partial t}\Delta t + 2\frac{\partial^2\phi}{\partial t^2}(\Delta t^2) + O(\Delta t^3) \quad (6.48)$$

Combining the above equations, we can find

$$\left(\frac{\partial\phi}{\partial t}\right) = \frac{\frac{3}{2}\phi^{n+1} - 2\phi^n + \frac{1}{2}\phi^{n-1}}{\Delta t} \quad (6.49)$$

The above discretization method is called the backward differencing, and is the method used in this study as it is easy to implement and computationally less expensive compared to Crank-Nicholson. The overall discretized transport equation now becomes

$$\frac{\frac{3}{2}\phi^{n+1} - 2\phi^n + \frac{1}{2}\phi^{n-1}}{\Delta t}V_P + \sum_f F\phi_f^{n+1} - \sum_f (\rho\Gamma_\phi)_f(\nabla\phi)_f^{n+1} = S_cV_P + S_PV_P\phi_P^{n+1} \quad (6.50)$$

6.5 Discretization of the Navier-Stokes equations

In the previous section, we dealt with the general principles involved in description a scalar transport equation. In particular we learned how to compute the gradient of the scalar ϕ on the cell faces, interpolating ϕ , Γ and U on the faces using schemes like the central difference and upwind schemes. We also dealt with the temporal schemes like the Crank-Nicholson scheme and the backward differencing scheme. The discretization of the Navier-Stokes equation can be handled very much like the transport equation with a slight modification. This is because

the N-S equations can be derived from the transport equation by substituting ϕ with velocity U and the diffusion coefficient Γ by μ and the source term by the pressure gradient term. The continuity and the momentum equations incompressible flow can be written as

$$\nabla \cdot U = 0 \quad (6.51)$$

$$\frac{\partial U}{\partial t} + \nabla \cdot (UU) - \nabla \cdot (\nu \nabla U) = -\nabla p \quad (6.52)$$

Two things that need to be paid special attention to are the non-linearity of the momentum equation and the pressure velocity coupling. Consider the non-linear term $\nabla \cdot (UU)$ integrated over the control volume. On applying the Green's theorem, we get

$$\int_{V_P} \nabla \cdot (UU) dV = \int_A dA \cdot (UU) = \sum_f A_f \cdot U_f U_f \quad (6.53)$$

The equation is linearized by approximating one of interpolated velocity on the face with the previous time step as below

$$\sum_f A_f \cdot U_f U_f \approx \sum_f (A_f U_f)^n U_f^{n+1} \quad (6.54)$$

In the above equation, n represents the previous time step and $n + 1$ represents the current time step.

In the Eqn. 6.52, if we knew the pressure distribution in the flow domain, calculating the velocity field would be a straight forward procedure. Since the pressure p is also one of the variables that we are solving for, we need to find a way to work around this issue. In this study we use the PISO (Pressure Implicit with Splitting of Operators) procedure, proposed by Issa [81]. Here, the pressure is coupled to the velocity through the conservation of mass flux (continuity equation). If we discretize the momentum equation (eqn 6.52) without doing anything to pressure gradient term, we obtain

$$a_P U_P^{n+1} = H(U) - \nabla p, \text{ where} \quad (6.55)$$

$$H(U) = \sum_N a_N U_N^n + \frac{U^n}{\Delta t} \quad (6.56)$$

Rearranging Eqn.6.55, we can solve for U_P as

$$U_P = \frac{H(U)}{a_P} - \frac{\nabla p}{a_P} \quad (6.57)$$

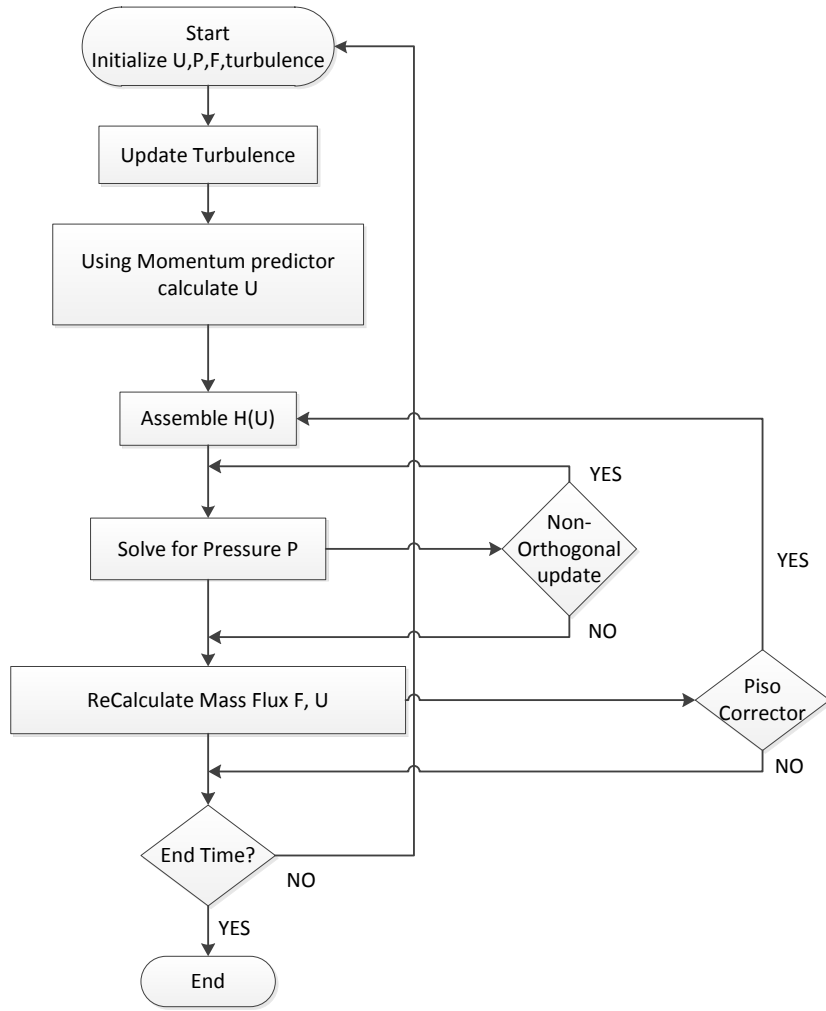


Figure 6.5 PISO algorithm

Equation 6.57 is known as momentum predictor equation. The continuity equation says that the divergence of the velocity is zero. If this the case, it must hold true for the velocity we compute (U_P), in each cell. Therefore,

$$\nabla \cdot U_P = 0 = \nabla \cdot \frac{H(U)}{a_P} - \nabla \cdot \left(\frac{\nabla p}{a_P} \right) \quad (6.58)$$

The above equation can be further simplified to obtain the pressure correction equation

$$\nabla \cdot \left(\frac{\nabla p}{a_P} \right) = \sum_f \left(\frac{H(U)}{a_P} \right)_f \quad (6.59)$$

The PISO algorithm is schematically shown in Fig. 6.5

1. At the beginning of the solution procedure initialize all the relevant variables
2. Using the pressure from the previous time step (or guessed pressure if it is the first time step), calculate U_P using Eqn. 6.57 (momentum predictor equation). This calculated velocity normally doesn't satisfy the continuity equation.
3. Assemble the H equation (Eqn. 6.56), and then interpolate to find $\left(\frac{H(U)}{a_P}\right)_f$ on the cell faces.
4. Solve the pressure correction equation (Eqn. 6.59) and find p .
5. Update the velocity U , using Eqn. 6.57, and calculate the mass flux on the cell faces.

Repeat steps 3 - 5 until the values of variables no longer change. This should not take more than 2 or 3 iterations. We then proceed to the next time step using the pressure calculated from this step as the starting guess value.

6.6 Application of LES to CIJR using OpenFOAM

In Chapter 5, we have discussed at length as to importance of investigating flow in the confined impinging jets reactors. The microPIV experiments were performed so that we can validate the simulations. Liu et al. [7] have investigated the simulation in CIR by performing RANS simulation using fluent using a two layer k-epsilon model. They found that the model over-predicted the turbulent kinetic energy at Reynolds number of 600 and under-predicted at Reynolds number of 1000. In this work, we perform the Large Eddy Simulation using OpenFOAM, an open source CFD library. OpenFOAM is a very advanced CFD library with capabilities of solving incompressible and compressible flow. They have a wide variety of turbulence models, linear solvers, boundary conditions and interpolation schemes that are already implemented, hence making it just a matter of choosing various options while solving. The entire code is written in a high level C++ language and one can easily modify the existing code or implement their own model or solver if required. Each problem is referred to as a case

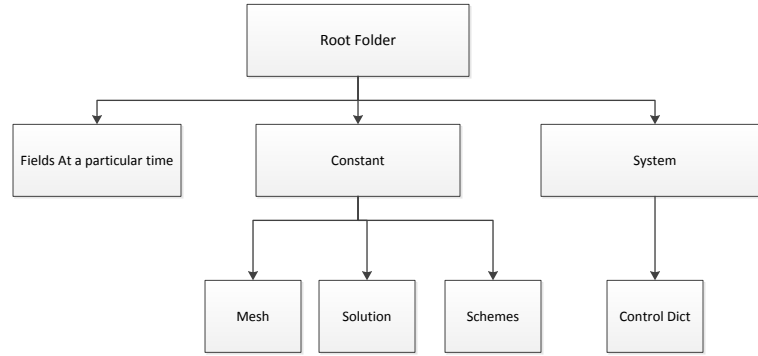


Figure 6.6 OpenFOAM case structure

and the structure of an OpenFOAM case is shown in Fig. 6.6. Each case folder contains three folders namely *Fields* (denoted by a time-step number), *constant*, and *system*. The Fields folder would be the 0 folder at the beginning of the simulation. It contains all the relevant field variables that we are solving for. In some cases, it also has some subsidiary files, which are used by the problem but are not necessary the variables that we need. The *constant* folder contains details about the mesh, the transport properties like viscosity and density, and the information about the models used for turbulence calculation. The *system* folder has the solution schemes and the solvers that are used to solve various variables. It also has a *controlDict* file which has information such as time stepping and parameters for collecting turbulence statistics. A detailed list of different solvers, schemes to calculate the divergence, gradient and interpolation are listed in Appendix A.

6.6.1 Grid generation

OpenFOAM comes with two built-in mesh generation utilities namely *blockMesh* and *snappyHexMesh*. The *blockMesh* utility is a very simple tool, where we provided information as to the location of the vertices, then the line connecting the vertices and the surfaces which form the boundaries, and the number of cells on each lines. This is very useful for generating rectangular meshes. However, the presence of the curved surface in CIR posed a problem to create a good mesh. Therefore, we used *snappyHexMesh* to generate the mesh in conjunction

with the *blockMesh*. The idea behind *snappyHexMesh* tool is very simple in that, we need to provide a coarse mesh and also the final geometry we need. The tool then carves out the geometry from the provided mesh and iteratively improves the grid based on the parameters that we have provided, like the total cell count or the dimension of the smallest cell etc. The mesh that was generated using this tool finally had approximately 0.6 million hexahedral cells.

6.6.2 SGS models analyzed

Three models namely *Smagorinsky*, *Dynamic Smagorinsky* and *One equation eddy* models were used to perform the simulations. OpenFOAM has the implementations for the three models just mentioned. However, in the case of dynamic model, it gives us a Smagorinsky constant averaged over the entire domain for a particular time step. Since we wanted to calculate the Smagorinsky constant dynamically which was a function of both time and space, a new model called *locAvgDynSmagorinsky* model was implemented.

6.6.3 Boundary conditions

No slip velocity boundary condition is used at the walls. In the case of the Reynolds number 1000, a fully developed 3D profile of the velocity was used at the inlets. The 3D profile was obtained by performing a simulation with a plug flow inlet on rectangular channel of the same cross section as that of the inlet. Pressure boundary condition was applied at the outlet. However, we have taken a slight different approach for inlet velocity boundary condition in the case of Reynolds number 1500. From the microPIV experiments, it was observed that the inlet channel length was not long enough to obtain a full developed flow at the entrance of the reactor. Therefore, we ended up simulating a channel flow with a uniform plug flow at its inlet and then let it develop. Various slices were taken along the length of the channel and the one which closely matched the peak velocity obtained from the experiments was chosen.

Solver	pisoFOAM
Pressure-Velocity Coupling	PISO
Divergence	Second Order Central
Gradient	Second Order
Time	Second Order Backward

Table 6.2 Simulation Details

6.6.4 Results and Discussion

The various schemes used in the simulation are summarized in Tab. 6.2. The simulation was run for approximately 25 residence times to allow for the flow to become turbulent, and the turbulent statistics were then collected for approximately 40 residence times. The performance of the three models at both the Reynolds numbers were analyzed. Though all the three models tested in the simulation performed reasonably well, we found that the Smagorinsky model seem to agree very well at Reynolds number of 1000 and the Dynamic Smagorinsky model agreed matched very well at Reynolds number of 1500 as will shown here. Therefore, the results presented here are with Smagorinsky model at $Re = 1000$ and dynamic Smagorinsky at $Re = 1500$.

6.6.4.1 Streamlines

Since the results obtained from the simulation are three dimensional, it is interesting to see how the streamlines look. Figures. 6.7 and 6.8 show the streamlines generated for the three points chosen on the $Z = 0$ plane at the inlets for mean flow at Reynolds number of 1000, and instantaneous flowfield at Reynolds numbers of 1500. It is very evident from looking at the figures that the flow is going out of the plane at $Z = 0$ in both the mean and the instantaneous flowfields, at both the Reynolds numbers. This shows that even in the planar reactor, when the Reynolds number is high enough, we see this unsteady three dimensional flow and care has to be taken to account for this out of plane motion as we are measuring the two dimensional flowfield from the experiments.

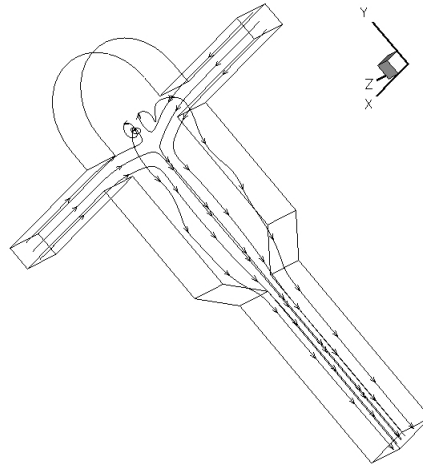


Figure 6.7 Streamlines at Re 1000

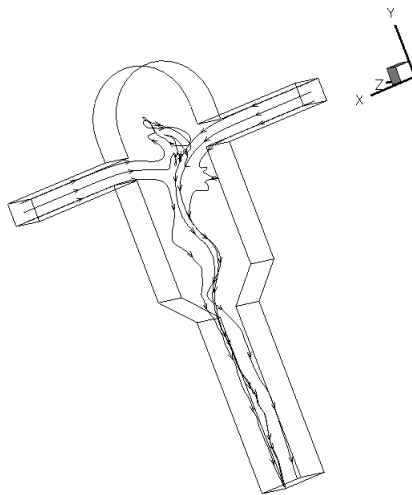


Figure 6.8 Instantaneous streamlines at Re 1500

6.6.5 Instantaneous and mean velocity flowfields

A very detailed explanation and analysis of the results for microPIV experiments on the CIR are explained in Sec 5.5. Here, we summarize the results and compare the simulation results with that of the experiments. Figure 6.9 shows the instantaneous velocity fields taken at the midplane ($Z = 0$) of the CIR at Reynolds numbers of 1000 and 1500, respectively. We see that at both the Reynolds numbers, the two inlet jets meet approximately along the centerline of the reactor. In the case of Reynolds number of 1000, the flapping is to the right of the line of symmetry and in the case of Reynolds number of 1500, the flapping is to the left of the line of symmetry. This flapping occurs back and forth about the line of symmetry. This flapping occurs as the horizontal momentum of the jets decreases to zero as they impinge, and as a result of this part of the jet turns toward the top of the reactor and the rest turns towards the outlet of the reactor.

The time averaged mean flowfields for Reynolds number of 1000 and Reynolds number of 1500 are shown in Fig. 6.10. The simulation shows that the two inlet jets meet just below the center of the inlet channels. At both the Reynolds numbers, two recirculation zones are formed at the top of the two inlet jets. When compared to the mean flow fields from the microPIV experiments as shown in Fig. 5.4, we notice not only that the jets in the simulation impinge approximately at the same location, but they also impinge at a point slightly above in the reactor compared to that of the experiments. This might be due to the fact that the impingement zone in the experiment at both Reynolds numbers are slightly bigger than that formed in the simulation. As a result of this, the jets meet at a point slightly lower in the reactor, along the line of symmetry. The peak velocities of 3m/s and 3.8m/s at Reynolds number of 1000 and Reynolds number of 1500, are in excellent agreement with the experimental results.

6.6.6 Reynolds Stresses

Figure 6.11 shows the normalized Reynolds normal stresses $\frac{\langle u'u' \rangle}{U^2}$ for Reynolds numbers of 1000 and 1500. The peak value of normalized Reynolds stresses are 0.55 and 0.63 at Reynolds

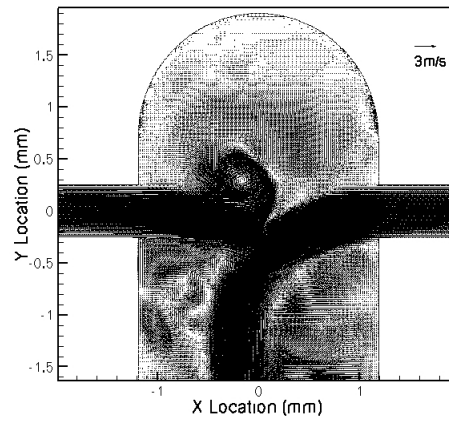
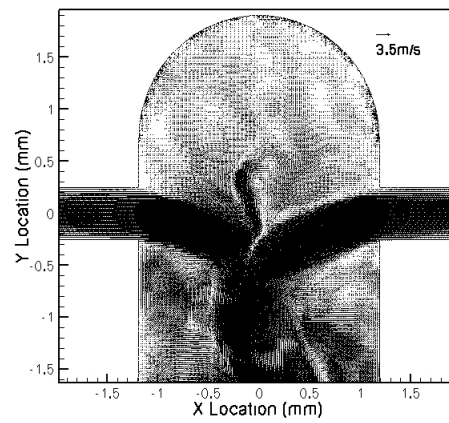
(a) $Re\ 1000$ (b) $Re\ 1500$

Figure 6.9 Instantaneous velocity vector fields at Reynolds numbers of 1000 and 1500.

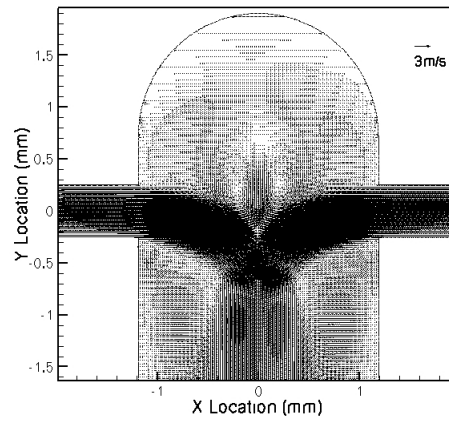
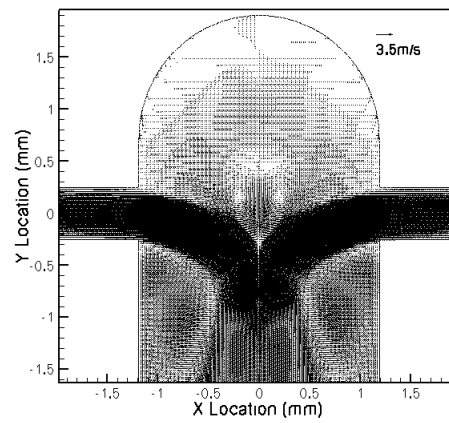
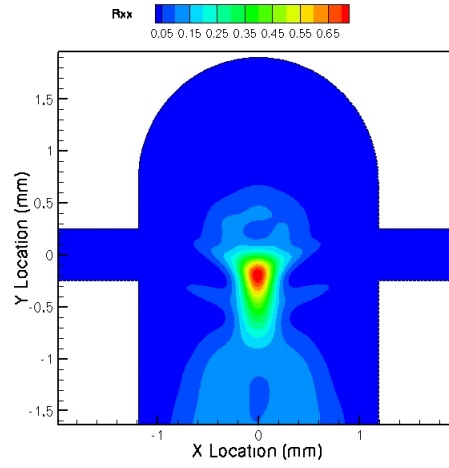
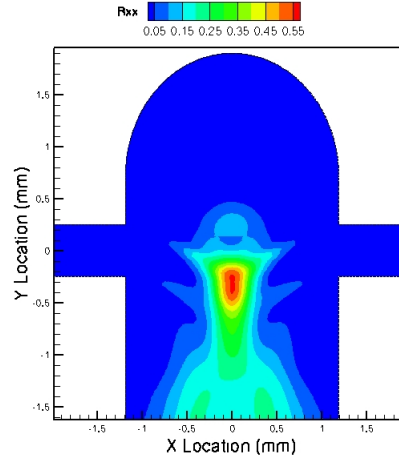
(a) Re 1000(b) Re 1500

Figure 6.10 Average velocity vector fields at Reynolds numbers at 1000 and 1500.

(a) $Re\ 1000$ (b) $Re\ 1500$ Figure 6.11 Normalized Reynolds normal stress $\frac{\langle u'u' \rangle}{U^2}$

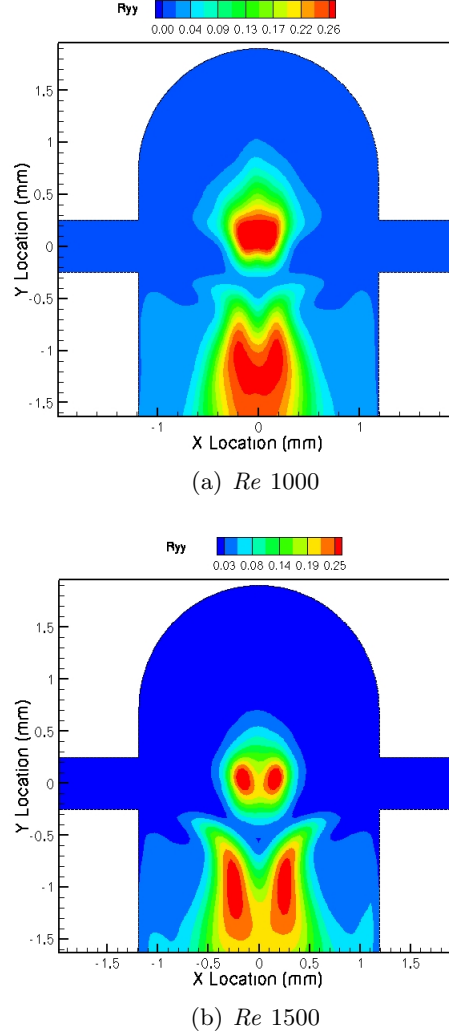
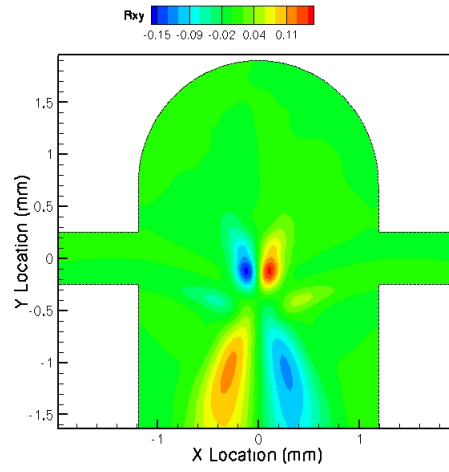
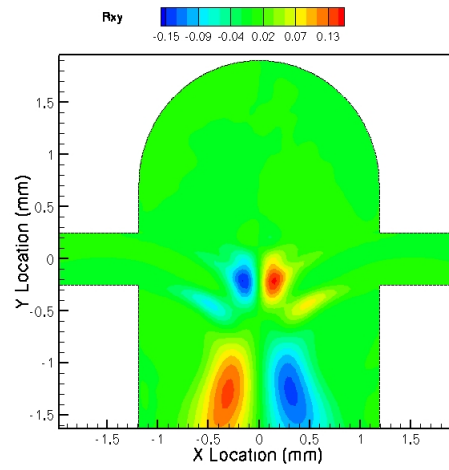


Figure 6.12 Normalized Reynolds normal stress $\frac{\langle u'v' \rangle}{U^2}$

numbers of 1000 and 1500 respectively. When compared to the normalized Reynolds stresses $\frac{\langle u'u' \rangle}{U^2}$ from microPIV as shown in Figs. 5.5 and 5.6, we see that the simulation captures the trend very accurately including the shape and the peak values. However, we notice that the impingement zone is more unstable in the experiments, and hence moves a lot in the horizontal direction. As a result of this, the region of the Reynolds stress in the experiments is larger than that of the region in the simulation.

Figure 6.12 shows the normalized Reynolds normal stresses $\frac{\langle v'v' \rangle}{U^2}$ for Reynolds numbers of 1000 and 1500. The simulation does capture the shape and normalized magnitudes very well

(a) Re 1000(b) Re 1500Figure 6.13 Normalized Reynolds normal stress $\frac{\langle v'v' \rangle}{U^2}$

compared to the normalized $\frac{\langle v'v' \rangle}{U^2}$ from the microPIV experiments as shown in Figs. 5.7 and 5.8. In the case of Reynolds number of 1500, we notice that in the upper half, just about the center of the reactor, there are two regions of high magnitude of $\frac{\langle v'v' \rangle}{U^2} = 0.23$. This region coincides with the two counter rotating regions that can be seen from the mean flowfield at the same location, as shown in Fig. 6.10(b). In the experiments, it is very hard to resolve the vertical component of the velocity in this region as the time interval Δt is chosen mainly to resolve the x-velocity in that region.

Figure. 6.13 shows the normalized Reynolds shear stress $\frac{\langle u'v' \rangle}{U^2}$ for Reynolds numbers of 1000 and 1500. The shape of the shear stress at both the Reynolds number resemble the shape of butterfly wings. The reason for this kind of shape is explained in details in Sec. 5.5.2.1. When compared to the normalized Reynolds shear stress from the microPIV experiments as shown in Figs 5.9 and 5.10, we notice that though the normalized magnitudes and shape of the contours match extremely well with simulation, the area of the stresses is larger in the experiments compared to that of the simulation. This can be attributed to the fact that the impingement zone moves quite a bit in the experiment, perhaps due the fact that it is extremely hard to balance the two inlet jets perfectly.

6.7 Conclusions

The flow in the confined impinging jets reactor was analyzed using large eddy simulation. A hexahedral grid comprising of approximately 0.7 million cells was used to simulate the flow. Three different models namely Smagorinsky, local dynamic Smagorinsky and One equation eddy were used to model the contribution of the subgrid scales. The local dynamic model was implement in the OpenFOAM to calculate the Smagorinsky constant dynamically as a function of both time and space. Since the results obtained from the experiments are at the midplane and two dimensional, only the 2D data from the midplane of the simulation are compared. It was found the Smagorinsky model gave an excellent agreement with the results from the MicroPIV experiments at Reynolds number 1000 and the local dynamic Smagorinsky model gave the best agreement with the experiments at Reynolds number 1500. It was noticed

that the two inlet jets met at the center line along the line of symmetry approximately at the same location for both Reynolds numbers of 1000 and 1500. This was not the case in the experiments, where the jets met slightly below the center of the inlets for Reynolds number of 1000 and further down towards the outlet for Reynolds number of 1500. It could be reasoned that the impingement zone as seen from the experiments is larger in the experiments when compared to that of the simulation, and this might make the jets bend more towards the outlet in the experiments, effectively making the jets meet slightly lower than the simulations. The agreement between the normalized Reynolds normal and shear stresses with the experiment is outstanding in that the simulation captures not only the overall shape accurately, but also the magnitude of the normalized stresses. However, we did notice that the area of the Reynolds shear stress at 1500 is smaller than that from experiments at the same Reynolds number. This is due to the fact that the impingement zone moves more in the experiments due to the difficulty in balancing the inlet jets as described before.

CHAPTER 7. Conclusion and Future work

In this dissertation, we have applied techniques like the microPIV, flow visualization using phenolphthalein, and Large eddy simulation successfully to microscale devices. Specifically, mircoPIV was performed to analyze the flow in herringbone micromixers at low reynolds numbers, where the effect of placing the pattern on the surface of the channel in generating a transverse velocity in the midplane was investigated. The flow across the transverse direction is periodic as the surface pattern repeats itself. We also noticed that the presence of these grooves (chevrons) generated a counter rotating secondary flow, which can be realized by noticing the change of sign in the transverse velocity near the chevron peaks. It was further found that the secondary flow (normalized transverse velocity) was identical for the cases of $Re = 0.008$ and $Re = 0.8$. The flow in this micromixer can be thought of a channel comprising of one channel split into a number of smaller channels. We also learnt that the internal angle of the chevorn does significantly affect the transverse velocity generated, and that the internal angle of 135° performs the best when compared to 90° and 45° internal angles.

A flow visualization technique was developed, and successfully applied to analyze the turbulent reactive mixing in confined impinging jets reactor. A new experimental setup was developed wherein, a short pulsed ($5\mu s$) xenon lamp was triggered by means of a timing unit in order to freeze the motion, so as to see the structures in the flow. Experiments were performed at three different jets Reynolds numbers namely 25, 1000 and 1500. At the lowest Reynolds number, the mixing is purely by diffusion, and we see a sharp interface inside the reactor, where the acidic and the basic solutions meet. At higher Reynolds number, we noticed a highly unsteady motion as a result of two high velocity jets impinging in the center of the reactor. This can be thought of as a imaginary plane rocking back and forth. A technique to

extract the quantitative mixing data was then proposed, which involved identifying the regions in the flow field that correspond to the regions of pH higher than 9.3 and to regions of pH less than or equal to 9.3. The ensemble average of the images that were processed with the pH technique, gives us the probability fields (mixture fraction). Using this method we found that the mixing performance increased as the Reynolds number increased. Finally, spatial auto-correlations of the thresholded image fluctuations were calculated. The correlations suggested that large-scale turbulent structures grew as they convected towards the reactor outlet and provided further evidence of oblique flapping of the impingement zone.

The flow in the CIJR was analyzed using microPIV and Large eddy simulation. The study was performed at Reynolds numbers of 200, 1000 and 1500 respectively. The flow at the Reynolds number of 200 was perfectly laminar with no unsteadiness whatsoever. At higher Reynolds numbers, we observed the high velocity jets collided approximately along the center line of the reactor. This resulted in flapping motion which rocked back and forth making it a highly unsteady flow. The Reynolds normal and Reynolds shear stresses were computed and analyzed for cases of $Re=1000$ and $Re=1500$. We found that the Reynolds shear stresses have the shape of the butterfly wing, which could be thought of as a result of the imaginary plane rocking back and forth about the center of the impingement zone. Spatial correlations were performed to analyze the size of the structures in the flow. We found the regions of high correlations ($u'u'$) were smaller for the higher Reynolds number, which would mean the structures are small. OpenFOAM was used to perform the numerical simulations (LES) on the CIJR. Three models namely Smagorinsky, Dynamic Smagorinsky and One Equation eddy model were tested at Reynolds numbers of 1000 and 1500. It was found that the Smagorinsky model worked best for the case of the $Re = 1000$ and Dynamics Smagorinsky model worked best for the case of $Re = 1500$. As a part of the study, the Dynamic Smagorinsky model was implemented in OpenFOAM. We found that there was excellent agreement between the results obtained from the LES to that obtained from microPIV. In this particular study, we didn't perform a detailed analysis of the different grid resolutions. We propose to do that as the first step in ensuring that the solution obtained is grid independent. As a future work,

with the availability of the experimental data, one can perform Linear stochastic estimation. We recommend that the LES of the passive scalar transport be performed first, followed by implementation of the reactive mixing models.

APPENDIX A. ADDITIONAL MATERIAL

This is now the same as any other chapter except that all sectioning levels below the chapter level must begin with the *-form of a sectioning command.

OpenFOAM

Centred schemes	
linear	Linear interpolation (central differencing)
cubicCorrection	Cubic scheme
midPoint	Linear interpolation with symmetric weighting
Upwinded convection schemes	
upwind	Upwind differencing
linearUpwind	Linear upwind differencing
skewLinear	Linear with skewness correction
QUICK	Quadratic upwind differencing
TVD schemes	
limitedLinear	limited linear differencing
vanLeer	van Leer limiter
MUSCL	MUSCL limiter
limitedCubic	Cubic limiter
NVD schemes	
SFCD	Self-filtered central differencing
Gamma ψ	Gamma differencing

Table A.1 Interpolation schemes

Scheme	Description
corrected	Explicit non-orthogonal correction
uncorrected	No non-orthogonal correction
limited ψ	Limited non-orthogonal correction
bounded	Bounded correction for positive scalars
fourth	Fourth order

Table A.2 Surface normal gradient schemes

Discretization scheme	Description
Gauss $< interpolationScheme >$	Second order, Gaussian integration
leastSquares	Second order, least squares
fourth	Fourth order, least squares
cellLimited $< gradScheme >$	Cell limited version of one of the above schemes
faceLimited $< gradScheme >$	Face limited version of one of the above schemes

Table A.3 Discretization schemes available in *gradSchemes*

Scheme	Numerical behavior
corrected	Unbounded, second order, conservative
uncorrected	Bounded, first order, non-conservative
limited ψ	Blend of corrected and uncorrected
bounded	First order for bounded scalars
fourth	Unbounded, fourth order, conservative

Table A.4 Behavior of surface normal schemes used in *laplacianSchemes*

Scheme	Numerical behavior
linear	Second order, unbounded
skewLinear	Second order, (more) unbounded, skewness correction
cubicCorrected	Fourth order, unbounded
upwind	First order, bounded
linearUpwind	First/second order, bounded
QUICK	First/second order, bounded
TVD schemes	First/second order, bounded
SFCD	Second order, bounded
NVD schemes	First/second order, bounded

Table A.5 Behavior of interpolation schemes used in *divSchemes*

Scheme	Description
Euler	First order, bounded, implicit
CrankNicholson ψ	Second order, bounded, implicit
backward	Second order, implicit
steadyState	Does not solve for time derivatives

Table A.6 Discretization schemes available in *ddtSchemes*

Solver	Keyword
Preconditioned (bi-)conjugate gradient	PCG/PBiCG [†]
Solver using a smoother	smoothSolver
Generalized geometric-algebraic multi-grid	GAMG

[†]PCG for symmetric matrices, PBiCG for asymmetric

Table A.7 Linear solvers

Preconditioner	Keyword
Diagonal incomplete-Cholesky (symmetric)	DIC
Faster diagonal incomplete-Cholesky (DIC with caching)	FDIC
Diagonal incomplete-LU (asymmetric)	DILU
Diagonal	diagonal
Geometric-algebraic multi-grid	GAMG
No preconditioning	none

Table A.8 Preconditioner options

Smoother	Keyword
Gauss-Seidel	GaussSeidel
Diagonal incomplete-Cholesky (symmetric)	DIC
Diagonal incomplete-Cholesky with Gauss-Seidel (symmetric)	DICGaussSeidel

Table A.9 Smoother options

BIBLIOGRAPHY

- [1] C. D. Meinhart, S. T. Wereley, and M. H. B. Gray. Volume illumination for two-dimensional particle image velocimetry. *Measurement Science and Technology*, 11:809, 2000.
- [2] Chuong Vinh Nguyen, Andreas Fouras, and Josie Carberry. Improvement of measurement accuracy in micro PIV by image overlapping. *Experiments in Fluids*, 49(3):701–712, 2010.
- [3] S. T. Wereley, L. Gui, and C. D. Meinhart. Advanced algorithms for microscale particle image velocimetry. *AIAA journal*, 40(6):10471055, 2002.
- [4] J. G. Santiago, S. T. Wereley, C. D. Meinhart, D. J. Beebe, and R. J. Adrian. A particle image velocimetry system for microfluidics. *Experiments in Fluids*, 25(4):316–319, 1998.
- [5] Hao Li and Michael G. Olsen. Aspect ratio effects on turbulent and transitional flow in rectangular microchannels as measured with MicroPIV. *Journal of Fluids Engineering*, 128(2):305–315, March 2006.
- [6] Hao Li and Michael G. Olsen. MicroPIV measurements of turbulent flow in square microchannels with hydraulic diameters from 200 [μ]m to 640 [μ]m. *International Journal of Heat and Fluid Flow*, 27(1):123–134, February 2006.
- [7] Ying Liu, Michael G. Olsen, and Rodney O. Fox. Turbulence in a microscale planar confined impinging-jets reactor. *Lab on a Chip*, 9(8):1110, 2009.
- [8] Janine Chungyin Cheng, Michael G. Olsen, and Rodney O. Fox. A microscale multi-inlet vortex nanoprecipitation reactor: Turbulence measurement and simulation. *Applied Physics Letters*, 94(20):204104, 2009.

- [9] J. M Ottino and S. Wiggins. Introduction: mixing in microfluidics. *Philosophical Transactions of the Royal Society of London. Series A: Mathematical, Physical and Engineering Sciences*, 362(1818):923, 2004.
- [10] Todd M. Squires and Stephen R. Quake. Microfluidics: Fluid physics at the nanoliter scale. *Reviews of Modern Physics*, 77(3):977, October 2005.
- [11] A. J Mahajan and D. J Kirwan. Micromixing effects in a two-impinging-jets precipitator. *AIChE Journal*, 42(7):18011814, 1996.
- [12] A. J Mahajan and D. J. Kirwan. Rapid precipitation of biochemicals. *Journal of Physics D: Applied Physics*, 26:B176, 1993.
- [13] Ying Liu, Chungyin Cheng, Ying Liu, Robert K. Prud’homme, and Rodney O. Fox. Mixing in a multi-inlet vortex mixer (MIVM) for flash nano-precipitation. *Chemical Engineering Science*, 63(11):2829 – 2842, 2008.
- [14] Brian K. Johnson and Robert K. Prud’homme. Flash NanoPrecipitation of Organic Actives and Block Copolymers using a Confined Impinging Jets Mixer. *Aust. J. Chem.*, 56(10):1021–1024, January 2003.
- [15] R. Breidenthal. Structure in Turbulent Mixing Layers and Wakes Using a Chemical Reaction. *Journal of Fluid Mechanics*, 109:1–24, 1981.
- [16] Kuo Tseng Li and Herbert L. Toor. Chemical indicators as mixing probes. A possible way to measure micromixing simply. *Industrial & Engineering Chemistry Fundamentals*, 25(4):719–723, 1986.
- [17] S. Zhang, S. P. Schneider, and S. H. Collicott. Quantitative molecular-mixing measurements using digital processing of absorption images. *Experiments in Fluids*, 19(5):319–327, September 1995.

- [18] R.H. Liu, M.A. Stremler, K.V. Sharp, M.G. Olsen, J.G. Santiago, R.J. Adrian, H. Aref, and D.J. Beebe. Passive mixing in a three-dimensional serpentine microchannel. *Microelectromechanical Systems, Journal of*, 9(2):190–197, Jun 2000.
- [19] Sunghwan Chang and Young-Ho Cho. Static micromixers using alternating whirls and lamination. *Journal of Micromechanics and Microengineering*, 15(8):1397–1405, 2005.
- [20] Ronald J. Adrian. Particle imaging techniques for experimental fluid mechanics. *Annual Review of Fluid Mechanics*, 23:261–304, 1991.
- [21] Markus Raffel, Christian E. Willert, Steve T. Wereley, and Jürgen Kompenhans. *Particle Image Velocimetry: A Practical Guide*. Springer Berlin Heidelberg, 2nd edition, 2007.
- [22] C. D. Meinhart, S. T. Wereley, and J. G. Santiago. PIV measurements of a microchannel flow. *Experiments in Fluids*, 27(5):414–419, October 1999.
- [23] Michael G. Olsen and Ronald J. Adrian. Brownian motion and correlation in particle image velocimetry. *Optics & Laser Technology*, 32(7-8):621–627, October 2000.
- [24] M. G. Olsen and R. J. Adrian. Out-of-focus effects on particle image visibility and correlation in microscopic particle image velocimetry. *Experiments in Fluids*, 29(0):S166–S174, December 2000.
- [25] C. J. Bourdon, M. G. Olsen, and A. D. Gorby. Power-filter technique for modifying depth of correlation in microPIV experiments. *Experiments in Fluids*, 37(2):263–271, 2004.
- [26] R.H. Liu, M.A. Stremler, K.V. Sharp, M.G. Olsen, J.G. Santiago, R.J. Adrian, H. Aref, and D.J. Beebe. Passive mixing in a three-dimensional serpentine microchannel. *Journal of Microelectromechanical Systems*, 9(2):190–197, 2000.
- [27] A. D Stroock, S. K Dertinger, G. M Whitesides, and A. Ajdari. Patterning flows using grooved surfaces. *Analytical chemistry*, 74(20):5306–5312, 2002.
- [28] F. G Bessoth and A. Manz. Microstructure for efficient continuous flow mixing. *Anal. Commun.*, 36(6):213–215, 1999.

- [29] N. L Jeon, H. Baskaran, S. K.W Dertinger, G. M Whitesides, L. Van De Water, and M. Toner. Neutrophil chemotaxis in linear and complex gradients of interleukin-8 formed in a microfabricated device. *Nature biotechnology*, 20(8):826–830, 2002.
- [30] F. Sch\`onfeld, V. Hessel, and C. Hofmann. An optimised split-and-recombine micro-mixer with uniform ‘chaotic’ mixing. *Lab Chip*, 4(1):65–69, 2004.
- [31] B. H Jo, L. M Van Lerberghe, K. M Motsegood, and D. J Beebe. Three-dimensional micro-channel fabrication in polydimethylsiloxane (PDMS) elastomer. *Microelectromechanical Systems, Journal of*, 9(1):76–81, 2000.
- [32] J. R Anderson, D. T Chiu, R. J Jackman, O. Cherniavskaya, J. C McDonald, H. Wu, S. H Whitesides, and G. M Whitesides. Fabrication of topologically complex three-dimensional microfluidic systems in PDMS by rapid prototyping. *Analytical Chemistry*, 72(14):3158–3164, 2000.
- [33] M. K McQuain, K. Seale, J. Peek, T. S Fisher, S. Levy, M. A Stremmer, and F. R Haselton. Chaotic mixer improves microarray hybridization. *Analytical biochemistry*, 325(2):215–226, 2004.
- [34] G. M Walker, J. Sai, A. Richmond, M. Stremmer, C. Y Chung, and J. P Wikswo. Effects of flow and diffusion on chemotaxis studies in a microfabricated gradient generator. *Lab on a Chip*, 5(6):611, 2005.
- [35] A. D Stroock, S. K.W Dertinger, A. Ajdari, I. Mezić, H. A Stone, and G. M Whitesides. Chaotic mixer for microchannels. *Science*, 295(5555):647, 2002.
- [36] Christopher J Bourdon, Michael G Olsen, and A D Gorby. Validation of an analytical solution for depth of correlation in microscopic particle image velocimetry. *Measurement Science and Technology*, 15(2):318–327, 2004.
- [37] Raghunath Halder, Adeniyi Lawal, and Reddy Damavarapu. Nitration of toluene in a microreactor. *Catalysis Today*, 125(1-2):74–80, July 2007.

- [38] Chun-Xia Zhao, Lizhong He, Shi Zhang Qiao, and Anton P.J. Middelberg. Nanoparticle synthesis in microreactors. *Chemical Engineering Science*, In Press, Corrected Proof:–, 2010.
- [39] Samuel Marre and Klavs F. Jensen. Synthesis of micro and nanostructures in microfluidic systems. *Chem. Soc. Rev.*, 39:1183–1202, 2010.
- [40] Volker Hessel, Holger Lwe, and Friedhelm Schnfeld. Micromixers—a review on passive and active mixing principles. *Chemical Engineering Science*, 60(8-9):2479 – 2501, 2005. 5th International Symposium on Mixing in Industrial Processes (ISMIP5).
- [41] L. Falk and J.-M. Commenge. Performance comparison of micromixers. *Chemical Engineering Science*, 65(1):405 – 411, 2010. 20th International Symposium in Chemical Reaction Engineering—Green Chemical Reaction Engineering for a Sustainable Future.
- [42] J.M. Khler, L. Abahmane, J. Wagner, J. Albert, and G. Mayer. Preparation of metal nanoparticles with varied composition for catalytical applications in microreactors. *Chemical Engineering Science*, 63(20):5048 – 5055, 2008. 5TH Unsteady-State Processes in Catalysis: a Special Issue of Chemical Engineering Science.
- [43] Brian K. Johnson and Robert K. Prud’homme. Chemical processing and micromixing in confined impinging jets. *AIChE Journal*, 49(9):2264–2282, 2003.
- [44] Dieter Horn and Jens Rieger. Organic Nanoparticles in the Aqueous Phase - Theory, Experiment, and Use. *Angewandte Chemie International Edition*, 40(23):4330–4361, 2001.
- [45] Ying Liu. *Formulating nanoparticles by Flash NanoPrecipitation for drug delivery and sustained release*. PhD thesis, Princeton University, November 2007.
- [46] Qian Qiu Zhao, Arthur Boxman, and Uma Chowdhry. Nanotechnology in the Chemical Industry - Opportunities and Challenges. *Journal of Nanoparticle Research*, 5(5):567–572, December 2003.

- [47] Ying Liu and Rodney O. Fox. CFD predictions for chemical processing in a confined impinging-jets reactor. *AIChE Journal*, 52(2):731–744, 2006.
- [48] Janine Chungyin Cheng, Michael G. Olsen, and Rodney O. Fox. A microscale multi-inlet vortex nanoprecipitation reactor: Turbulence measurement and simulation. *Applied Physics Letters*, 94(20):204104, 2009.
- [49] Ying Liu, Michael G. Olsen, and Rodney O. Fox. Turbulence in a microscale planar confined impinging-jets reactor. *Lab on a Chip*, 9(8):1110–1118, 2009.
- [50] J. Baldyga, J. R. Bourne, and B. Walker. Non-isothermal micromixing in turbulent liquids: Theory and experiment. *Can. J. Chem. Eng.*, 76(3):641–649, 1998.
- [51] Hua Feng, Michael Olsen, James Hill, and Rodney Fox. Simultaneous velocity and concentration field measurements of passive-scalar mixing in a confined rectangular jet. *Experiments in Fluids*, 42:847–862, 2007. 10.1007/s00348-007-0265-7.
- [52] David R. Unger and Fernando J. Muzzio. Laser-induced fluorescence technique for the quantification of mixing in impinging jets. *AIChE Journal*, 45(12):2477–2486, 1999.
- [53] Elena Abarca and T. Prabhakar Clement. A novel approach for characterizing the mixing zone of a saltwater wedge. *Geophys. Res. Lett.*, 36:–, March 2009.
- [54] Edward Caldin. *Fast reactions in solution*. Wiley, New York, 1964.
- [55] Izaak Maurits Kolthoff. *Acid-base indicators*. Macmillan, New York, 1937.
- [56] William K. Pratt. *Digital Image Processing: PIKS Scientific Inside*. Wiley, New Jersey, 4th edition, 2007.
- [57] Matteo Icardi, Emmanuela Gavi, Daniele L. Marchisio, Michael G. Olsen, Rodney O. Fox, and Djamel Lakehal. Validation of LES predictions for turbulent flow in a Confined Impinging Jets Reactor. *Applied Mathematical Modelling*, 35(4):1591 – 1602, 2011.

- [58] Matteo Icardi, Emmanuela Gavi, Daniele L. Marchisio, Antonello A. Barresi, Michael G. Olsen, Rodney O. Fox, and Djamel Lakehal. Investigation of the flow field in a three-dimensional Confined Impinging Jets Reactor by means of microPIV and DNS. *Chemical Engineering Journal*, 166(1):294 – 305, 2011.
- [59] Brian K. Johnson and Robert K. Prud’homme. Chemical processing and micromixing in confined impinging jets. *AIChE Journal*, 49(9):2264–2282, 2003.
- [60] S. W Siddiqui, Y. Zhao, A. Kukukova, and S. M Kresta. Characteristics of a confined impinging jet reactor: Energy dissipation, homogeneous and heterogeneous reaction products, and effect of unequal flow. *Industrial & Engineering Chemistry Research*, 48(17):7945–7958, 2009.
- [61] E. Gavi, D. L Marchisio, and A. A Barresi. CFD modelling and scale-up of confined impinging jet reactors. *Chemical engineering science*, 62(8):2228–2241, 2007.
- [62] R. J Adrian. Particle-imaging techniques for experimental fluid mechanics. *Annual Review of Fluid Mechanics*, 23(1):261304, 1991.
- [63] Richard D. Keane and Ronald J. Adrian. Theory of cross-correlation analysis of PIV images. *Applied Scientific Research*, 49(3):191–215, July 1992.
- [64] J. Westerweel. Digital particle image velocimetry: theory and application, June 1993.
- [65] Markus Raffel, Chris Willert, and J. Kompenhans. *Particle Image Velocimetry: A Practical Guide*. Springer, corrected edition, June 2002.
- [66] A. K. Prasad, R. J. Adrian, C. C. Landreth, and P. W. Offutt. Effect of resolution on the speed and accuracy of particle image velocimetry interrogation. *Experiments in Fluids*, 13(2-3):105–116, 1992.
- [67] K. T. Christensen. The influence of peak-locking errors on turbulence statistics computed from PIV ensembles. *Experiments in fluids*, 36(3):484–497, 2004.

- [68] M. Stanislas, K. Okamoto, C. J. Khler, and J. Westerweel. Main results of the second international PIV challenge. *Experiments in Fluids*, 39(2):170–191, 2005.
- [69] S. B Pope. *Turbulent flows*. Cambridge Univ Pr, 2000.
- [70] H. Tennekes and J. L Lumley. *A first course in turbulence*. The MIT press, 1972.
- [71] J. Smagorinsky. General circulation experiments with the primitive equations. *Monthly Weather Review*, 91(3):99–164, 1963.
- [72] A. N Kolmogorov. The local structure of turbulence in incompressible viscous fluid for very large reynolds numbers. In *Dokl. Akad. Nauk SSSR*, volume 30, page 9–13, 1941.
- [73] D. K Lilly. The representation of small scale turbulence in numerical simulation experiments. 1967.
- [74] Massimo Germano, Ugo Piomelli, Parviz Moin, and William H. Cabot. A dynamic subgrid-scale eddy viscosity model. *Physics of Fluids A: Fluid Dynamics*, 3(7):1760, 1991.
- [75] D. K. Lilly. A proposed modification of the germano subgrid-scale closure method. *Physics of Fluids A: Fluid Dynamics*, 4(3):633, 1992.
- [76] Joel H. Ferziger and Milovan Peric. *Computational Methods for Fluid Dynamics*. Springer, 3rd edition, December 2001.
- [77] A. Jameson, W. Schmidt, E. Turkel, et al. Numerical solutions of the euler equations by finite volume methods using Runge-Kutta time-stepping schemes. *AIAA paper*, 81:1259, 1981.
- [78] Hrvoje Jasak. Error analysis and estimation for the finite volume method with applications to fluid flows. *Direct*, M(June), 1996.
- [79] C. Hirsh. *Numerical Computation of Internal and External Flows, Vol. 1*. John Wiley & Sons, Brussels, 1991.
- [80] S. V Patankar. *Numerical heat transfer and fluid flow*. Hemisphere Pub, 1980.

- [81] R. I. Issa. Solution of the implicitly discretised fluid flow equations by operator-splitting.
Journal of Computational Physics, 62(1):40–65, January 1986.